

**CONTROL OF FUEL CELL BASED GREEN ENERGY SYSTEMS FOR
DISTRIBUTED GENERATION APPLICATIONS**

DISSERTATION

Presented in Partial Fulfillment of the Requirements for the Degree Doctor of Philosophy
in the Graduate School of The Ohio State University

By

Sachin Puranik, M.S.

Graduate Program in Electrical Engineering

The Ohio State University

2009

Dissertation Committee:

Professor Ali Keyhani, Adviser

Professor Donald Kasten

Professor Betty Lise Anderson

© Copyright by

Sachin Puranik

2009

ABSTRACT

In this dissertation, a proton exchange membrane (PEM) fuel cell-based distributed generation (DG) system is analyzed by modeling various units of the DG system, performing mathematical analyses, and simulation studies. The suitable control strategies are designed for the specific units of the DG system in order to achieve the desired operating performance.

First, the nonlinear state space model of a 500-W PEM fuel cell is developed by modeling an open-circuit output voltage of the PEM fuel cell, irreversible voltage losses in the PEM fuel cell, formation of a charge double-layer in the PEM fuel cell, along with a mass balance and thermodynamic energy balance in the PEM fuel cell system. The state space model is validated, and then used to study the dynamic behavior of the PEM fuel cell under different input conditions. The modeling of the PEM fuel cell is also performed using the neural network approach, and the nonlinear autoregressive moving average model of the PEM fuel cell with external inputs (NARMAX) is developed using the recurrent neural network. It is shown that the two-layer neural network with a hyperbolic tangent sigmoid function, as an activation function, in the first layer, and a pure linear function, as an activation function, in the second layer can effectively model the nonlinear dynamics of the PEM fuel cell.

The sizing of the lead-acid battery bank, which is the energy storage element required for the DG system, is performed using the model of a 12 V, 4Ah lead-acid battery. The discharge characteristics of the battery model are studied, and the model is appropriately scaled to perform the design of the battery bank. Using the battery and dc/dc boost converter model, the charging of the battery bank is simulated in MATLAB/Simulink. A sliding mode control law is designed for the dc/dc converter to control its output voltage.

The application of two different control strategies to a single-phase and three-phase inverter is analyzed. The objective of the control design is to achieve low (total harmonic distortion) THD output voltage, fast transient response, and asymptotic tracking of reference output voltage under linear and nonlinear loads minimizing the effect of harmonic frequencies.

First, the proportional-derivative-integral (PID) technique is used to design the voltage and current controller for the single-phase and three-phase inverter. The robust servomechanism problem (RSP) voltage controller and the sliding mode current controller are then designed for the single-phase and three-phase inverter. For both the techniques, the control design is performed in a discrete-time domain. The performance of the single-phase and three-phase inverter with these control strategies is analyzed and the results are shown.

Dedicated to Aai, Baba, Neetu, and Anuja,

ACKNOWLEDGEMENTS

I would like to respectfully thank my adviser, Prof. Ali Keyhani, for giving me the opportunity to work under his guidance in the ‘Mechatronic - Green Energy Systems Lab’ at ‘The Ohio State University’. During last five years, I’ve learnt a lot from him. I admire the confident approach he brings to the work, and his supreme commitment to the field of electrical engineering is infectious. I sincerely thank him for providing me the adequate financial support during my doctoral studies. I like to acknowledge that, this work was supported in part by National Science Foundation (NSF) grant ECS0501349.

I thank Prof. Donald Kasten and Prof. Betty Lise Anderson for having agreed to serve on my dissertation committee.

I sincerely thank Prof. Farshad Khorrami, Dr. Prashanth Krishnamurthy, and Mr. Yun She from Polytechnic University, Brooklyn, New York, for their valuable inputs and comments during the process of the PEM fuel cell model development.

I thank all my former colleagues at ‘Mechatronic- Green Energy Systems Lab’ – Dr. Min Dai , Dr. Wenzhe Lu, Dr. Jin-woo Jung, and Dr Nanda Marwali – for helping me out at different times.

From the bottom of my heart, I’m grateful to my parents, Mr. Vishwas Puranik and Mrs. Sulbha Puranik, and my sister, Neeta, for their unwavering support, constant

encouragement, and extraordinary understanding throughout my graduate studies. I'm equally grateful to my in-laws, Mr. Suhas Moghe, Mrs. Lata Moghe, and my sister-in-law, Aditee, for their good wishes, and specifically, for their trust in my abilities. I humbly thank my uncle, Mr. Sadanand Tatke, whose thoughts and teachings have always guided me at crucial times during my graduate studies. I consider myself quite privileged to have been affiliated with him. I truly believe that this work could lead to completion only due to blessings and good wishes from all of them.

I specially thank my friend, Sumit Sinha from University of Illinois, Urbana-Champaign. The constant exchange of information and discussions with him over the period of last five years had wonderfully motivated me during my doctoral studies.

Many thanks are due to all my friends in Columbus – Yugendra, Aniruddha, Soumitra, Swapnil, Vrushali, Charuta, Richa, and Smita. They have made my stay in Columbus very enjoyable and provided any help required whenever needed.

Finally, I'm feeling short of words to articulate the companionship and support provided by my lovely wife, Anuja. I would have left this work long ago without her presence in my life. Ph.D. programs have different, at times uncomfortable, dynamics and, invariably, have peaks and troughs along the way. Anuja stood behind me through all of them. She was always willing to adjust everything according to my work schedules. There were umpteen weekends and holidays I've spent doing my work, and her acceptance of such routine had consistently been phlegmatic, without the slightest of grudge. I could not have asked for more, and I warmly thank her for the role she has played in making this endeavor a success.

VITA

1979.....Born – Thane, India

1996-2000.....B.E. Instrumentation and Control Engineering,
University of Mumbai, Mumbai, India.

2000-2001.....Instrumentation and Control Engineer
Deepak Fertilizers & Petrochemicals Pvt. Ltd.
Mumbai, India

2001-2002.....Control Engineer
SNC-Lavlin Pvt. Ltd., Mumbai, India.

2002-2004..... M.S. Electrical Engineering,
Mississippi State University,
Starkville, MS, USA.

2005-2008.....Graduate Research /Teaching Associate,
The Ohio State University, Columbus,
Ohio.

2008-2009..... Fuel Systems Control Engineer,
Caterpillar Inc.
Peoria, IL, USA.

2009-present..... Control Engineer,
BSI Industries, Inc.
Columbus, OH, USA.

FIELDS OF STUDY

Major Field: Electrical Engineering

TABLE OF CONTENTS

	Page
Abstract.....	ii
Dedication.....	iv
Acknowledgements.....	v
Vita.....	vii
List of Figures.....	xiv
List of Tables.....	xx
List of Abbreviations.....	xxi
Chapters:.....	
1. Introduction.....	1
1.1 Need of Renewable and Green Energy Systems.....	1
1.2 Background of Distributed Generation Systems.....	2
1.3 Topologies of Distributed Generation Systems.....	3
1.3.1 Stand-alone DG Systems Feeding to the Local Loads.....	3
1.3.2 DG System Connected to the AC Power Grid.....	7
1.4 Problem Formulation.....	9
1.5 Literature Review.....	11
1.5.1 Modeling of Fuel Cells.....	12
1.5.1.1 Analytical Modeling of Fuel Cells.....	12
1.5.1.2 Nonparametric Modeling of Fuel Cells.....	14

1.5.2	Control of Fuel Cell-based Distributed Generation (DG) Systems	16
1.5.3	Modeling of Energy Storage Devices	18
1.6	Research Objectives.....	22
1.6.1	Development of the PEM Fuel Cell Model	23
1.6.2	Charging of the Lead-Acid Battery bank from the PEM Fuel Cell Array	24
1.6.3	Control of a Single-Phase Inverter.....	25
1.6.4	Control of a Three-Phase Inverter	25
1.7	Organization of the Dissertation	26
2.	State Space Modeling of Proton Exchange Membrane Fuel Cell	28
2.1	Introduction.....	28
2.2	Open-Circuit Output Voltage of the PEM Fuel Cell	28
2.3	Irreversible Voltage Losses in the PEM Fuel Cell	31
2.3.1	Activation Losses.....	31
2.3.2	Ohmic Losses.....	32
2.3.3	Concentration Losses	32
2.4	Humidification in the PEM Fuel Cell.....	33
2.5	Mass Balance and Thermodynamic Energy Balance in the PEM Fuel Cell	33
2.6	Formation of a Charge Double Layer in the PEM Fuel Cell.....	37
2.7	Simulation of the the PEM Fuel Cell Model	40
2.8	Simulation Results	42
2.8.1	<i>V-I</i> Characteristics of the PEM Fuel Cell Model.....	42
2.8.2	Polarization Curves of the PEM Fuel Cell Model for Different Values of Input Variables	46

2.8.2.1	<i>V-I</i> Characteristics of the PEM Fuel Cell Model for Increasing Values of the Anode Channel Pressure (u_{p_A})	46
2.8.2.2	<i>V-I</i> Characteristics of the PEM Fuel Cell Model for Increasing Values of the Cathode Channel Pressure (u_{p_C})	47
2.8.3	Transient Response of the PEM Fuel Cell Model	49
2.8.3.1	Transient Response of the PEM Fuel Cell Model over a Short-Time Period.....	49
2.8.3.2	Transient Response of the PEM Fuel Cell Model over a Long-Time Period.....	50
2.8.4	Behavior of the PEM Fuel Cell Model under a Resistive (R) Load	52
2.9	Formulation of the PEM Fuel Cell Array	53
2.10	Chapter Summary	55
3.	Neural Network Modeling of Proton Exchange Membrane Fuel Cell	57
3.1	Introduction.....	57
3.2	The Neural Network Modeling Approach	57
3.3	Neural Network Model Development.....	58
3.3.1	Cross-Correlation Analysis.....	60
3.3.2	The Proposed Neural Network Model for the PEM Fuel Cell	64
3.3.3	Training of the Neural Network Model	66
3.4	Simulation Results	68
3.4.1	Polarization Curves of the PEM Fuel Cell Model for Different Values of Input Variables	73
3.4.2	Transient Response of the PEM Fuel Cell Model	76
3.5	Robustness Toward Noise	79
3.6	Chapter Summary	81

4. Modeling of Lead-Acid Battery and Control of DC/DC Converter	83
4.1 Introduction.....	83
4.2 Modeling of the Lead-Acid Battery	84
4.3 Identification of the Battery Model Parameters.....	87
4.3.1 Battery EMF (E_b).....	87
4.3.2 Self-Discharge Resistance (R_{sd})	88
4.3.3 Discharge Polarization Resistance (R_{dch})	90
4.3.4 Polarization Capacitance (C_{ov}).....	93
4.3.5 Charging Polarization Resistance (R_{ch})	93
4.4 Validation of the Lead-Acid Battery Model	95
4.5 Discharge Characteristics of the Battery Model	96
4.6 Scaling of the Battery Model for Different Battery Capacities	98
4.7 Design of the Battery Bank for the Fuel Cell-based DG System	98
4.7.1 Determination of the Terminal Voltage of the Battery bank	99
4.7.2 Determination of the Battery Bank Capacity.....	99
4.8 Summary Specifications	100
4.9 Determination of the Discharge Characteristics of 480 V, 90 Ah Battery Bank	101
4.10 Control of the DC/DC Boost Converter	103
4.11 Simulation of the PEM Fuel Cell Array with the DC/DC Boost Converter.....	107
4.12 Charging of 480V, 90Ah Lead-Acid Battery Bank	111
4.13 Chapter Summary	114
5. Control of a Single-Phase and Three-Phase Inverter.....	116

5.1	Introduction.....	116
5.2	Model of a Single-Phase Inverter	117
5.3	Control Development for the Single-Phase Inverter.....	118
5.4	Discrete-time PID Voltage and Current Control Design	119
5.5	Discrete-time Robust Servomechanism Problem (RSP) Voltage Control and Discrete-time Sliding Mode Current Control Design	122
5.5.1	Design Steps for the Discrete-time RSP Voltage Controller and Discrete-time Sliding Mode Current Controller	122
5.5.2	Step 1- Design of the Discrete-time Sliding Mode Current Controller ..	123
5.5.3	Step 2 - Formulation of the Plant for the Discrete-time RSP Voltage Controller	124
5.5.4	Step 3- Design of the Discrete-time RSP Voltage Controller	126
5.5.5	Necessary Conditions for the Existence of a Solution of the Robust Servomechanism Problem	127
5.6	Internal Model Principle	128
5.7	Design Steps for the RSP Voltage Controller.....	129
5.7.1	Step 1: The Servocompensator Design.....	130
5.7.2	Step 2: Determination of the Augmented System	131
5.7.3	Step 3: Design of the Stabilizing Compensator	132
5.8	Model of a Three-Phase Inverter	134
5.9	Control Development for the Three-Phase Inverter	139
5.10	Simulation Results	143
5.10.1	Simulation Results of the Single-Phase Inverter with the Discrete-time PID Voltage Controller and Discrete-time PID Current Controller	144
5.10.2	Simulation Results of the Single-Phase Inverter with the Discrete-time RSP Voltage Controller and Discrete-time	

Sliding Mode Current Controller	147
5.10.3 Simulation Results of the Three-Phase Inverter with the Discrete-time PID Voltage Controller and Discrete-time PID Current Controller	150
5.10.4 Simulation Results of the Three-Phase Inverter with the Discrete-time RSP Voltage Controller and Discrete-time Sliding Mode Current Controller	155
5.11 Chapter Summary	163
6. Conclusions and Future Work	165
6.1 Conclusions of the Dissertation	165
6.2 Future Work	168
Bibliography	169

LIST OF FIGURES

Figures	Page
1.1 Topology 1: Photovoltaic Array-based Stand-alone DG System	3
1.2 Topology 1: Microturbine-based Stand-alone DG System.....	4
1.3 Topology 1: Fuel Cell-based Stand-alone DG System.....	5
1.4 Topology 2: Photovoltaic Array-based Stand-alone DG System	6
1.5 Topology 2: Fuel Cell-based Stand-alone DG System.....	7
1.6 DG System Connected to the AC Power Grid.....	8
1.7 PEM Fuel Cell-based Stand-alone DG System Feeding to Local Loads	9
1.8 A Simple Battery Model	19
1.9 Thevenin Battery Model	20
1.10 Improved Thevenin Battery Model.....	21
1.11 Dynamic Model of A Lead-Acid Battery	22
2.1 Working of the PEM Fuel Cell	29
2.2 Formation of a Charge Double Layer in the PEM Fuel Cell	37
2.3 Implementation of the PEM Fuel Cell Model in MATLAB/Simulink.....	41
2.4 <i>V-I</i> characteristics of the PEM Fuel Cell Model.....	43
2.5 Validation of the PEM Fuel Cell Model.....	43
2.6 Output Voltage Response of the PEM Fuel Cell Model.....	44

2.7	Temperature Response of the PEM Fuel Cell Model	45
2.8	<i>P-I</i> Characteristics of the PEM Fuel Cell Model	46
2.9	<i>V-I</i> Characteristics of the PEM Fuel Cell Model for Increasing u_{P_A}	47
2.10	<i>V-I</i> Characteristics of the PEM Fuel Cell Model for Increasing u_{P_C}	48
2.11	Transient Response of the PEM Fuel Cell Model over a Short-time Period (Top: Stack current, Bottom: Output Voltage).....	49
2.12	Transient Response of the PEM Fuel Cell Model over a Long-time Period	51
2.13	Output Voltage of the PEM Fuel Cell Model under a Resistive Load	52
2.14	Stack Temperature of the PEM Fuel Cell Model under a Resistive Load.....	52
2.15	Formulation of the PEM Fuel Cell array in MATLAB/Simulink	54
2.16	<i>V-I</i> Characteristics of the PEM Fuel Cell Array	55
3.1	Structure of A Multilayer Feedforward Neural Network	59
3.2	Structure of A Recurrent Neural Network.....	60
3.3	Cross-correlation between V_{fc} and u_{P_A}	62
3.4	Cross-correlation between V_{fc} and u_{P_C}	62
3.5	Cross-correlation between V_{fc} and u_{T_R}	63
3.6	Structure of the Proposed Neural Network Model of the PEM Fuel Cell	64
3.7	Training of the Neural Network Model for the Output Voltage Values.....	67
3.8	Training of the Neural Network Model for the Stack Temperature Values	67
3.9	Validation of the Neural Network Model of the PEM Fuel Cell.....	68
3.10	Validation of the State Space Model of the PEM Fuel Cell	69
3.11	Polarization Characteristics of the Neural Network Model.....	70
3.12	Output Voltage Response of the Neural Network Model.....	71

3.13	<i>P-I</i> Characteristics of the Neural Network Model	72
3.14	Temperature Response of the Neural Network Model	73
3.15	<i>V-I</i> Characteristics of the PEM Fuel Cell Model for Increasing u_{P_A}	74
3.16	<i>V-I</i> Characteristics of the PEM Fuel Cell Model for Increasing u_{P_C}	75
3.17	Transient Response of the Model over a Short-time Period	77
3.18	Transient Response of the Model over a Long-time Period	78
3.19	Performance of the Neural Network Model for SNR = 200:1	79
3.20	Performance of the Neural Network Model for SNR = 50:1	80
4.1	The Proposed Lead-Acid Battery Model	85
4.2	Variation in E_b as a Function of the Battery SOC	88
4.3	Variation in R_{sd} as a Function of the Battery SOC	89
4.4	Discharge Characteristics of <i>Yuasa NP4-12</i> Battery (From the manufacturer's data sheet)	90
4.5	Variation in R_{bdi} with the Discharge Current	91
4.6	Variation in R_{bd} with the Battery SOC	92
4.7	Variation in R_{bc} with the Battery SOC	94
4.8	Validation of the Battery Model	96
4.9	Discharge Characteristics of the Battery Model (12 V, 4Ah)	97
4.10	Variation in the Battery SOC for Different Discharge Currents	97
4.11	Block Diagram for Determining the Discharge Characteristics of the Battery Bank	102
4.12	Discharge Characteristics of the battery bank	102
4.13	Variation in the SOC of the Battery Bank during Discharging	103

4.14	The DC/DC Boost Converter.....	104
4.15	Block Diagram of the Sliding Mode Control Design for the DC/DC Boost Converter	105
4.16	Simulation of the PEM Fuel Cell Array with the DC/DC Boost Converter in MATLAB/Simulink.....	107
4.17	DC/DC Boost Converter with the Sliding Mode Controller in MATLAB/Simulink.....	108
4.18	Output Voltage of the DC/DC Boost Converter	109
4.19	DC Output Current	109
4.20	Sliding Surface $S = x_{1bc} - x_{1bc}^* = 0$	110
4.21	Sliding Mode (Equivalent Control u_{eq}) Control Switching Pattern.....	110
4.22	Charging Characteristics of the Battery Bank (with charging current = 12A, charging time = 450 minutes)	111
4.23	Variation in the SOC of the Battery Bank (Case I: charging current = 12A).....	112
4.24	Charging Characteristics of the Battery Bank (with charging current = 18A, charging time = 300 minutes)	112
4.25	Variation in the SOC of the Battery Bank (Case II: charging current = 18A) ...	113
4.26	Charging Characteristics of the Battery Bank (with charging current = 25.5A, charging time = 212 minutes)	113
4.27	Variation in the SOC of the Battery Bank (Case III: Charging current =25.5A)	114
5.1	Single-Phase Full-Bridge Inverter	117
5.2	Control Block Diagram of the Discrete-time PID Voltage and Current Control for Single-Phase Inverter	119
5.3	Discrete-time PID Voltage Controller for the Single-Phase Inverter	121
5.4	Discrete-time PID Current Controller for the Single-Phase Inverter	121
5.5	Control Block Diagram of the Discrete-time RSP Voltage Control and	

	Discrete-time Sliding Mode Current Control for the Single-Phase Inverter	122
5.6	Block Diagram of the Discrete-time RSP Voltage Controller.....	134
5.7	Three-Phase Inverter with a Low-pass L-C Filter and a Transformer.....	135
5.8	A Delta-wye Transformer Model	136
5.9	Control Block Diagram of the Discrete-time PID Voltage Control and Current Control for the Three-Phase Inverter.....	140
5.10	Discrete-time PID Voltage Controller for the Three-Phase Inverter.....	140
5.11	Discrete-time PID Current Controller for the Three-Phase Inverter	141
5.12	Control Block Diagram of the Discrete-time RSP Voltage Control and Discrete-time Sliding Mode Current Control for the Three-Phase Inverter	142
5.13	Block Diagram of the Discrete-time RSP Voltage Controller for Three- Phase Inverter	142
5.14	Simulation Results of the Single-Phase Inverter under Linear (R-L) Load with Power Factor 0.7 (Top: Load Voltage, Middle: Load Current, Bottom: Load (RMS) Voltage).....	145
5.15	Comparison of the Reference Voltage with the Actual Load Voltage of the Single-Phase Inverter under Linear (R-L) Load with Power Factor 0.7	145
5.16	Simulation Results of the Single-Phase Inverter under Nonlinear load (Top: Load Voltage, Middle: Load Current, Bottom: Load (RMS) Voltage)	146
5.17	Comparison of the Reference Voltage with the Actual Load Voltage of the Single-Phase Inverter under Nonlinear Load.....	146
5.18	Simulation Results of the Single-Phase Inverter under Linear (R-L) Load with Power Factor 0.7 (Top: Load Voltage, Middle: Load Current, Bottom: Load (RMS) Voltage).....	148
5.19	Comparison of the Reference Voltage with the Actual Load Voltage of the Single-Phase Inverter with Linear (R-L) Load with Power Factor 0.7	148
5.20	Simulation Results of the Single-Phase Inverter under Nonlinear load (Top: Load Voltage, Middle: Load Current, Bottom: Load (RMS) Voltage)...	149
5.21	Comparison of the Reference Voltage with the Actual Load Voltage of the	

Single-Phase Inverter under Nonlinear Load.....	149
5.22 Simulation Results of the Three-Phase Inverter under Balanced Linear Load (Top: Load Voltage, Middle: Load Current, Bottom: Load (RMS) Voltage)	151
5.23 Comparison of the Reference Voltage with the Actual Load Voltage of the Three-Phase Inverter (in the d-q axis reference frame) under Balanced Linear Load.....	152
5.24 Simulation Results of the Three-Phase Inverter under Nonlinear Load (Top: Load Voltage, Middle: Load Current, Bottom: Load (RMS) Voltage)	153
5.25 Comparison of the Reference Voltage with the Actual Load Voltage of the Three-Phase Inverter (in the d-q axis reference frame) under NonLinear Load.....	154
5.26 Simulation Results of the Three-Phase Inverter under Balanced Linear Load (Top: Load Voltage, Middle: Load Current, Bottom: Load (RMS) Voltage)	156
5.27 Comparison of the Reference Voltage with the Actual Load Voltage of the Three-Phase Inverter (in the d-q axis reference frame) under Balanced Linear Load.....	157
5.28 Simulation Results of the Three-Phase Inverter under Unbalanced Linear Load Case I: Phase A: Fully Loaded, Phase B: 75% Loaded, Phase C: 75% Loaded (Top: Load Voltage, Middle: Load Current, Bottom: Load (RMS) Voltage)...	158
5.29 Transient Response of the Three-Phase Inverter for 100% to 75% Load Change (Top: Load Current, Bottom: Load Voltage)	159
5.30 Transient Response of the Three-Phase Inverter for 50% to 100% Load Change (Top: Load Current, Bottom: Load Voltage)	160
5.31 Simulation Results of the Three-Phase Inverter under Nonlinear Load (Top: Load Voltage, Middle: Load Current, Bottom: Load (RMS) Voltage)	161
5.32 Comparison of the Reference Voltage with the Actual Load Voltage of the Three-Phase Inverter (in the d-q axis reference frame) under Nonlinear Load	162
5.33 Simulation Results of the Three-Phase Inverter for Short-circuit Condition (Top: Load Voltage, Bottom: Inverter Current).....	163

LIST OF TABLES

Tables	Page
2.1 Parameters of the PEM Fuel Cell Model.....	42
3.1 Mean Squared Voltage Errors for Different Signal-to-Noise Ratios (SNRs).....	81
4.1 Parameters of 12 V, 4Ah Battery Model	100
4.2 Parameters of 480 V, 90Ah Battery Bank	101
5.1 Parameters of the Single-Phase Full-Bridge Inverter	117
5.2 Parameters of the Three-Phase Inverter System.....	135
5.3 Single-Phase Inverter: Results with the Discrete-time PID Voltage and Current Controller.....	144
5.4 Single-Phase Inverter: Results with the Discrete-time RSP Voltage Controller and Discrete-time Sliding Mode Current Controller	147
5.5 Three-Phase Inverter: Results with the Discrete-time PID Voltage and Current Controller.....	150
5.6 Three-Phase Inverter: Results with the Discrete-time RSP Voltage Controller and Discrete-time Sliding Mode Current Controller	155

LIST OF ABBREVIATIONS

- A_s : Area of a single cell (m^2).
- a, b : Constants in Tafel equation (V / K).
- a_0 : Constant in Tafel equation (V).
- C : Capacitance due to charge double layer (F).
- C_{fc} : Specific heat capacity of PEM fuel cell stack [$J / (mol.K)$].
- D_w : Diffusion coefficient (m^2 / s).
- E_0^A : Standard reference potential of anode (V).
- E_0^C : Standard reference potential of cathode (V).
- E^{Cell} : Reversible cell potential (V).
- E_0^{Cell} : Reference potential at standard operating conditions (V).
- e : Number of participating electrons
- F : Faraday's constant (C / mol).
- ΔG : Change in a Gibb's free energy (J / mol).
- ΔG^0 : Change in a Gibb's free energy at standard operating conditions (J / mol).
- h_s : Convective heat transfer coefficient [$W / (m^2.K)$].
- I : Stack current (A).

I_d	: Current density (A / m^2).
I_L	: Limiting current (A).
K_I	: Constant in computation of R^0 (Ω / A).
K_T	: Constant in computation of R^0 (Ω / K).
M_{fc}	: Total mass of PEM fuel cell stack (kg).
$(m_{H_2})_{in}$: Inlet flow rate of hydrogen (mol / s).
$(m_{H_2})_{out}$: Outlet flow rate of hydrogen (mol / s).
$(m_{H_2})_{net}$: Net mole flow rate of hydrogen (mol / s).
$(m_{H_2O})_{net}$: Net mole flow rate of water (mol / s).
$(m_{O_2})_{in}$: Inlet flow rate of oxygen (mol / s).
$(m_{O_2})_{out}$: Outlet flow rate of oxygen (mol / s).
$(m_{O_2})_{net}$: Net mole flow rate of oxygen (mol / s).
$(m_{H_2O})_{in}^a$: Mole flow rate of water at anode (mol / s).
$(m_{H_2O})_{in}^c$: Mole flow rate of water at cathode (mol / s).
M_v	: Moles of vapor (mol).
$(m_v)_M$: Vapor transfer rate (mol / s).
n_d	: Electro-osmotic Coefficient
n_s	: Number of PEM fuel cell stacks
P_{H_2}	: Partial pressure of hydrogen (atm).

- P_{O_2} : Partial pressure of oxygen (*atm*).
- P_{H_2O} : Partial pressure of water (*atm*).
- $(P_{H_2O})_{in}^a$: Partial pressure of water at anode (*atm*).
- $(P_{H_2O})_{in}^c$: Partial pressure of water at cathode (*atm*).
- $P_{H_2O}^{Sat}$: Saturated vapor pressure of water (*atm*).
- Q_C : Heat generated due to electrochemical reaction (*J*).
- Q_E : Heat generated due to electricity (*J*).
- Q_L : Heat loss by air convection (*J*).
- R : Universal gas constant [*J/(mol.K)*].
- R^A : Resistance of anode (Ω).
- R^{Act} : Equivalent resistance corresponding to activation voltage loss (Ω).
- R^C : Resistance of cathode (Ω).
- R^{Conc} : Equivalent resistance corresponding to concentration voltage loss (Ω).
- R^O : Ohmic resistance (Ω).
- R_c^O : Constant in computation of R^O (Ω).
- R^M : Resistance of membrane (Ω).
- T : Stack temperature (*K*).
- t_m : Membrane thickness (*m*).
- u_{P_A} : Channel pressure of hydrogen (*atm*).

u_{P_C}	: Channel pressure of oxygen (<i>atm</i>).
u_{T_R}	: Room temperature (<i>K</i>).
V_a	: Volume of anode (m^3).
V_c	: Volume of cathode (m^3).
V_C	: Voltage across capacitor (<i>V</i>).
V_{fc}	: Output voltage of PEM fuel cell (<i>V</i>).
$V_{O,FC}$: Open-circuit output voltage (<i>V</i>).
V^{Act}	: Activation voltage loss (<i>V</i>).
V^O	: Ohmic voltage loss (<i>V</i>).
V^{Conc}	: Concentration voltage loss (<i>V</i>).
λ_A	: Flow delay at anode (<i>sec</i>).
λ_C	: Flow delay at cathode (<i>sec</i>).
ϕ_a	: Relative humidity at anode.
ϕ_c	: Relative humidity at cathode.

CHAPTER 1

INTRODUCTION

1.1 Need of Renewable and Green Energy Systems

Today, in the first decade of the 21st century, energy consumption around the world has increased astronomically. New generation technologies have arrived in various walks of life, and proper operation of most of these new technologies requires reliable and sustainable energy [1]. In some overpopulated countries, like in India, there exists a dearth of power-generating resources, and the conventional centralized power generation units are not entirely capable of meeting rising power demands. As a result, many cities are facing constant load shedding, brown-outs, and even black-outs. One of the potential solutions for these problems is to generate power in a distributed manner, making use of alternate energy resources, such as fuel cells, photovoltaic cells, wind turbines, and microturbines.

Moreover, generation of power in a conventional manner requires combustion of hydrocarbon-rich fossil fuels such as coal, oil and natural gas. The combustion of these hydrocarbon-rich resources is proving to be dangerous for the environment, as it releases carbon dioxide, one of the major anthropogenic greenhouse gases, in the earth's atmosphere, contributing to the effect of 'global warming' [2]. The ill-effects of 'global

warming' have been perceived worldwide by many researchers, and there exists a pronounced need to use alternate, more environmental-friendly power-generation methods which would not have any detrimental impact on the environment.

The concept of 'green energy' has thus evolved based on the idea of generating electrical power without any harmful impact on the environment and it can be realized using various technologies. The hydrogen-based resources, like fuel cells and microturbines; renewable energy sources, like photovoltaic cells and wind power can be used to generate green energy [2].

1.2 Background of Distributed Generation Systems

The idea behind distributed generation is not entirely new. During the salad days of electricity generation, due to the limited availability of supply voltages, DC power had been supplied to customers only in the vicinity of the generation [3]. The balance between demand and supply was achieved with the help of local battery storage.

In the DG system, electricity is produced from a large number of small-to-medium sized power plants, rather than from a centralized large capacity power plant. According to [4], "distributed generation is an electric power source connected directly to the distribution network or on the customer side of the meter". The capacity of the DG system can vary from tens of kilo-watts (kW) to hundreds of mega-watts MW. Many more definitions of DG can be found in [5], based on a system's rating, location, power delivery area, and underlying technology. DG systems can use various energy conversion technologies to generate power, such as: microturbines (MT), fuel cells (FC), photovoltaic arrays, wind power generators, biomass fuel, ultra capacitors, batteries, and

flywheels [6], [7]. An explanation of different topologies of the DG system based on different energy sources is given in the next section.

1.3 Topologies of Distributed Generation Systems

Various topologies of the DG system based on different energy sources are shown in Figures 1.1 to 1.5 [8]-[10].

1.3.1 Stand-alone DG Systems Feeding to the Local Loads

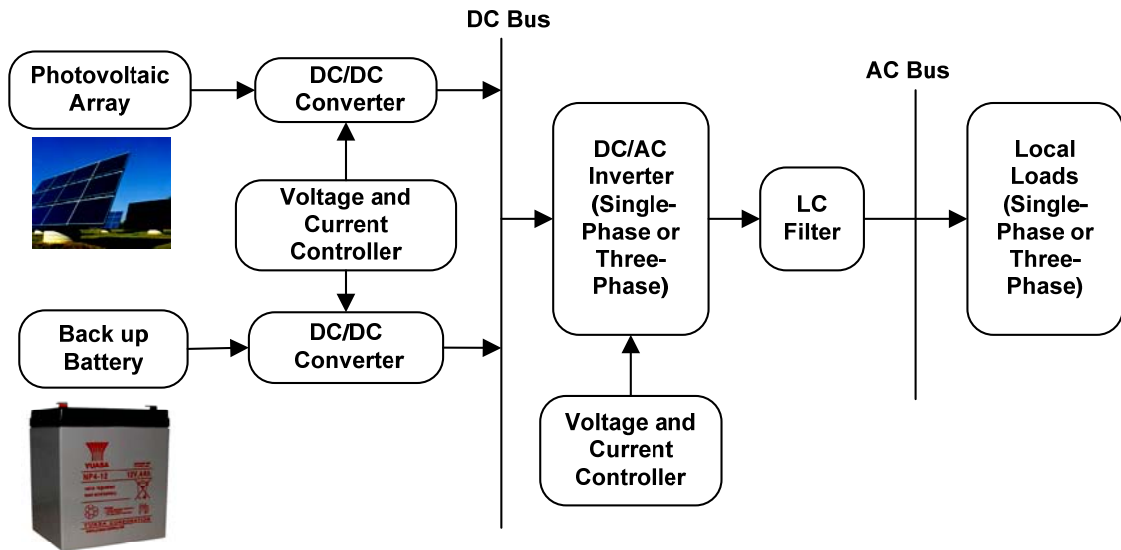


Figure 1.1 Topology 1: Photovoltaic Array-based Stand-alone DG System

Figure 1.1 shows the configuration of the stand-alone DG system based on a photovoltaic array feeding to the local single-phase and three-phase loads. The output of a photovoltaic array is low voltage DC (typically 48-60 V), which is boosted by the dc/dc

converter to get the required dc bus voltage (200-540 V) needed for the operation of a dc/ac inverter.

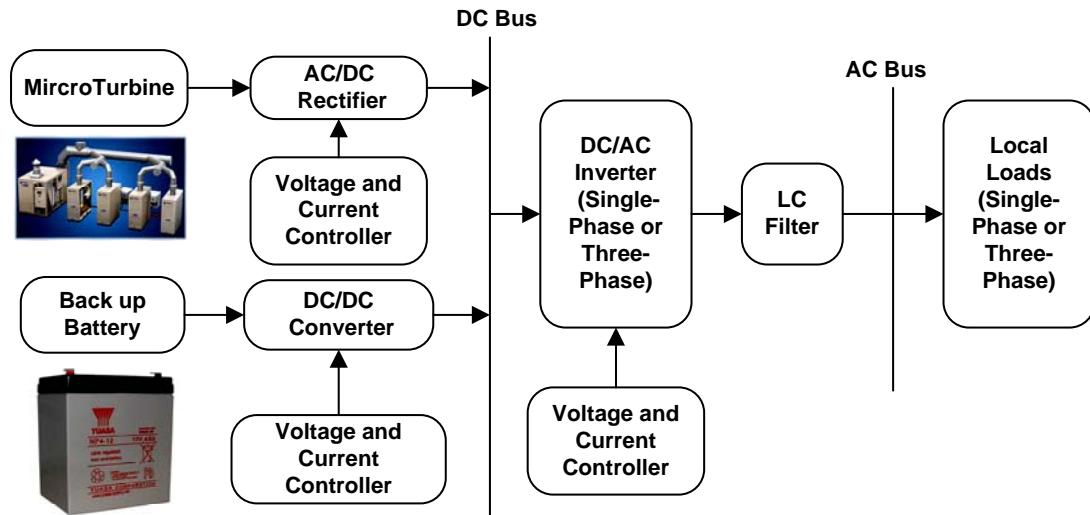


Figure 1.2 Topology 1: Microturbine-based Stand-alone DG System

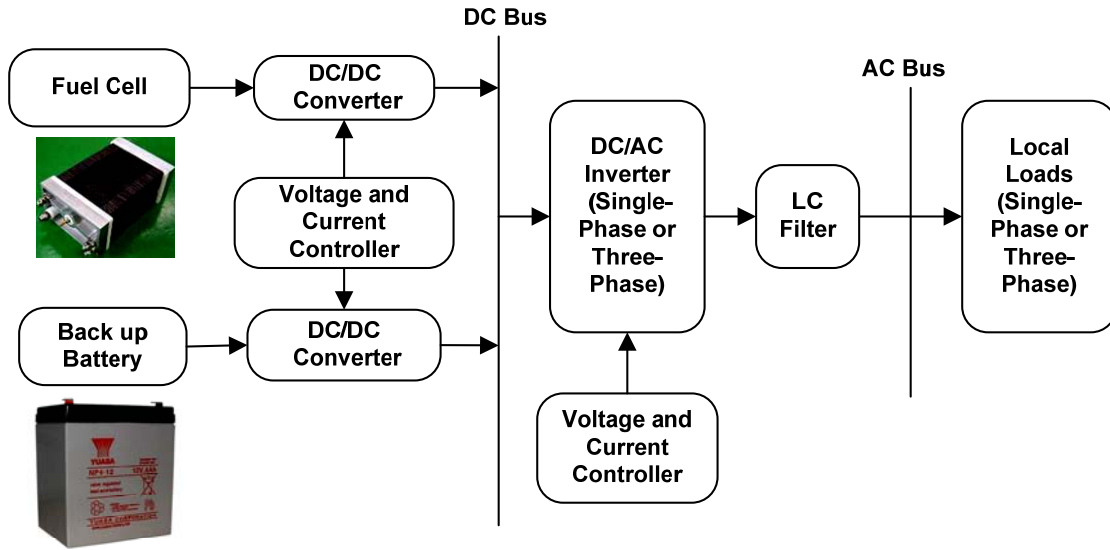


Figure 1.3 Topology 1: Fuel Cell-based Stand-alone DG System

Figures 1.2 and 1.3 show the configuration of the stand-alone DG system based on microturbine and fuel cell, respectively. As shown in Figure 1.2, the ac output voltage generated by the microturbine is rectified before it is fed to the dc/dc inverter. The back-up battery with a separate dc/dc converter is provided in each of the configurations shown in Figures 1.1, 1.2 and 1.3. The energy storage element is required in the DG system to protect the system from the weather dependency of some of the energy sources and to satisfy peak load demand.

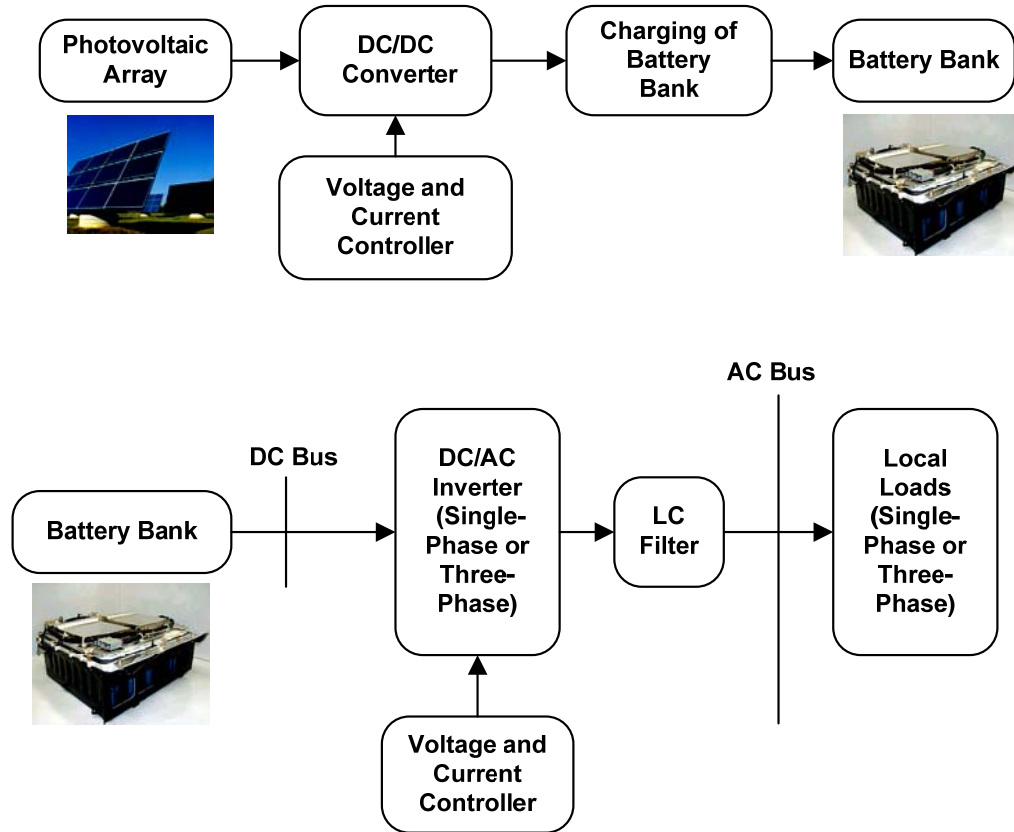


Figure 1.4 Topology 2: Photovoltaic Array-based Stand-alone DG System

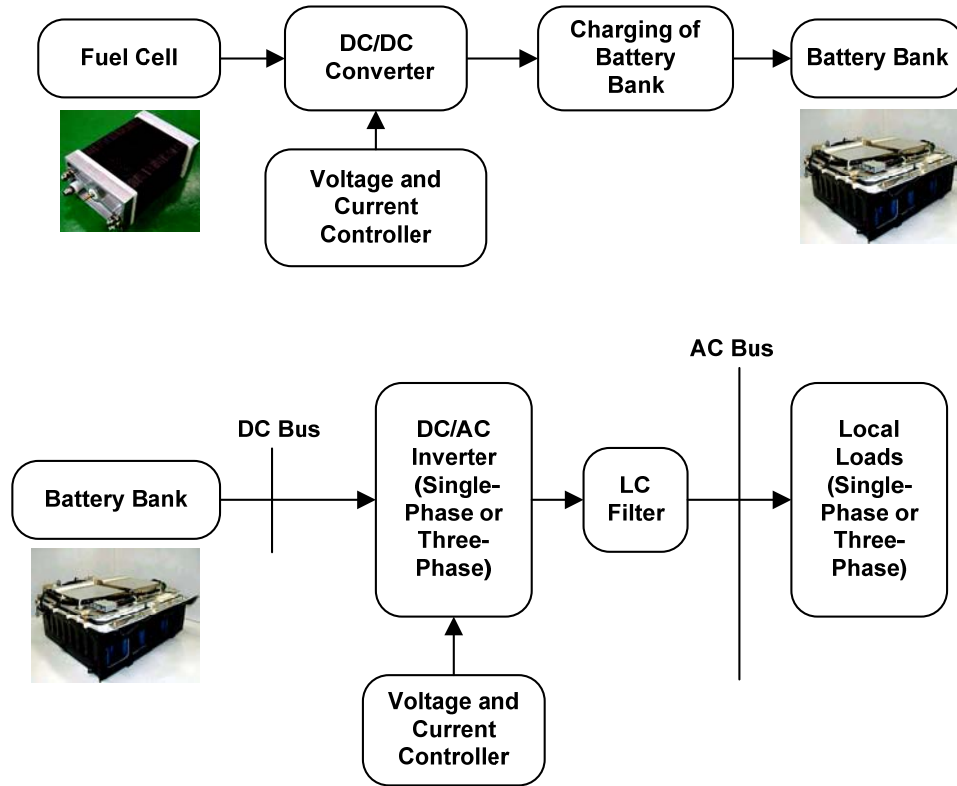


Figure 1.5 Topology 2: Fuel Cell-based Stand-alone DG System

Figures 1.4 and 1.5 depict a different topology of the DG system wherein the output voltages from the photovoltaic array and fuel cells are not directly fed to the dc/ac inverter but instead are used to charge the battery bank. The charged battery bank then provides the required dc bus voltage to the dc/ac inverter.

1.3.2 DG System Connected to the AC Power Grid

Figure 1.6 shows the topology of the DG system based on a photovoltaic array, microturbine, and fuel cell, and connected to the AC power grid. The lead-acid battery is

used as the energy storage device for the system. The step-up transformer is used, which steps up the voltage of the DG system necessary for synchronization with the AC power grid.

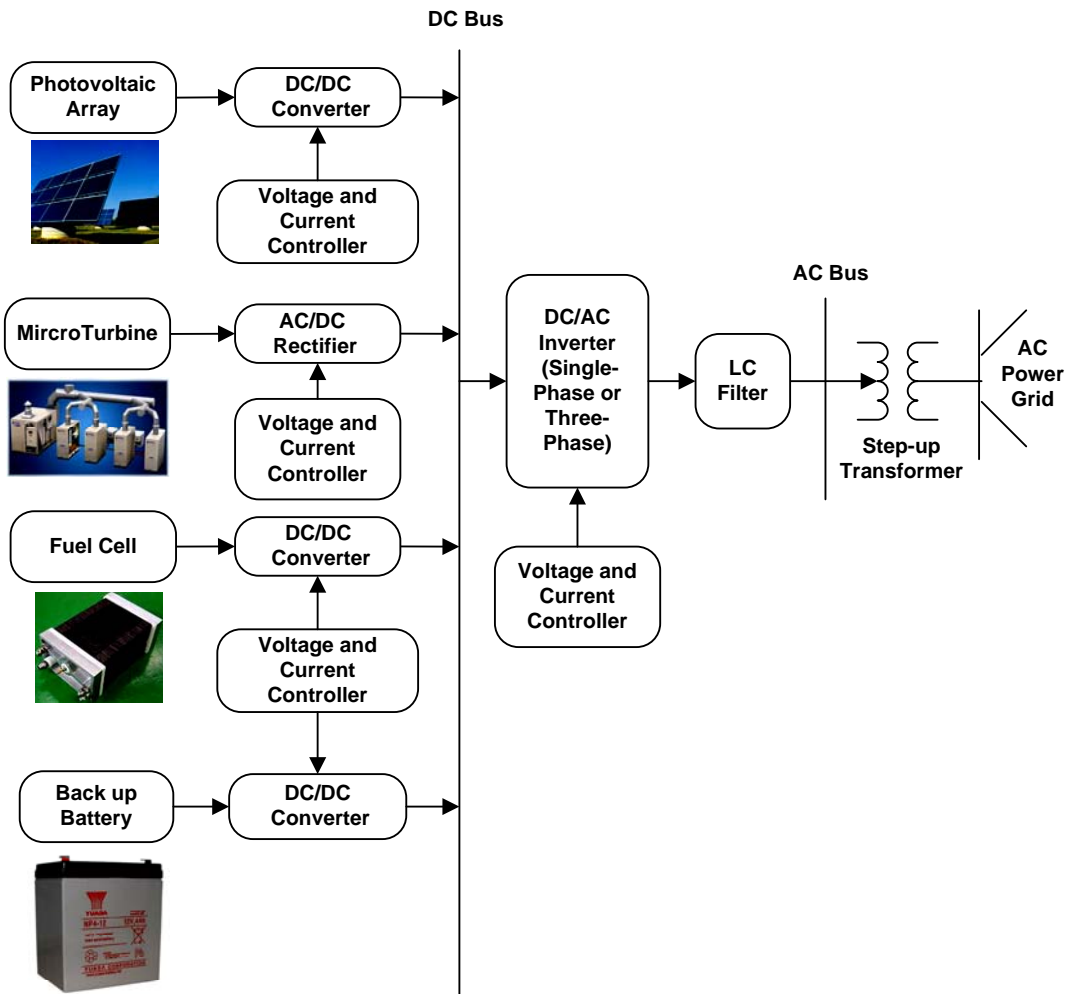


Figure 1.6 DG System Connected to the AC Power Grid

1.4 Problem Formulation

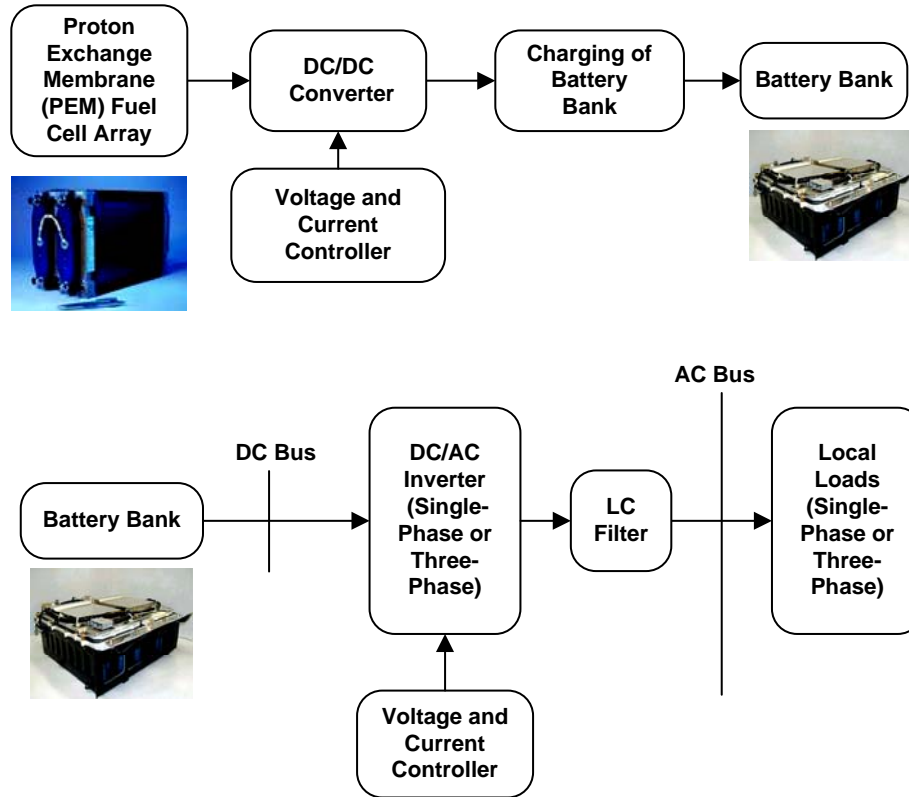


Figure 1.7 PEM Fuel Cell-based Stand-alone DG System Feeding to Local Loads

In this dissertation, an analysis of the fuel cell-based DG system, similar to that shown in Figure 1.5, is performed. Among the available fuel cells, phosphoric acid fuel cells (PAFC), proton exchange membrane (PEM) fuel cells, solid oxide fuel cells (SOFC) and molten carbonate fuel cells (MCFC), are important candidates for the DG system. Specifically, the PEM fuel cell possesses attractive features, such as high power density,

solid electrolyte, low operating temperature, fast start-up, low sensitivity to orientation, favorable power-to-weight ratio, long cell and stack life, and low corrosion [11]. Hence, the PEM fuel cell is a well-conceived candidate for developing distributed generation power systems. As a result, there is a growing interest in the PEM fuel cell-based DG system. A block diagram of the PEM fuel cell-based stand-alone DG system is shown in Figure 1.7.

It is important for the fuel cell-based DG system supplying to the residential and industrial loads to meet certain desired operating characteristics [12], [13]: The system should provide constant voltage to single-phase and three-phase loads upto the rated conditions. The system should provide the output voltage to the linear and nonlinear loads connected to the DG system with minimum total harmonic distortion (THD). The non-sinusoidal currents drawn by the nonlinear loads can distort the output voltage provided by the DG system to other loads and can lead to the generation of harmonic currents which can have a detrimental effect on the system performance. Suitable control strategies must be designed for the DG system to minimize the presence of unwanted harmonics in the system. Sudden load changes at the load terminals can cause voltage dips at the terminals of the DG system, which can distort the voltage provided by the DG system to other loads. Therefore, the control strategies designed for the DG system should have a fast transient response with minimum overshoot or undershoot under sudden load disturbances.

The dc/dc boost converter, storage element such as lead-acid battery, and the dc/ac single-phase and three-phase inverters are essential elements of the PEM fuel cell-based

DG system, as shown in Figure 1.7. The dc/dc boost converter is required to boost the output voltage of the PEM fuel cell. Typically, the output voltage of a 5-kW PEM fuel cell varies between 45 V - 75 V [14]. The boost converter boosts this voltage to charge the lead-acid battery bank. The desired dc bus voltage needed for proper operation of a single-phase or three-phase inverter is provided from the battery bank. Also, the battery bank must be properly sized. The dc/ac inverter used in the DG system can be a single-phase or a three-phase. It converts dc power generated by the PEM fuel cell to the ac power required by the residential and industrial loads. A suitable control technique must be properly designed to perform the voltage and current control of the single-phase or three-phase inverter, so that it can provide constant ac voltage to all types of loads – linear loads (balanced and unbalanced) and nonlinear loads – with minimum THD upto the rated conditions.

In this dissertation, aforementioned issues of the PEM fuel cell-based DG system are addressed. Solutions are provided by developing models of different units of the DG system, performing mathematical analyses, applying engineering theories, and designing suitable control strategies for specific units of the DG system. The literature is reviewed relevant to the research issues of the fuel cell-based DG system considered in this study.

1.5 Literature Review

Research on fuel cell-based DG systems has been reported in the literature. The literature is reviewed in the following three areas:

- (i) Modeling of fuel cells
- (ii) Control of fuel cell based Distributed Generation (DG) systems

(iii) Modeling of energy storage devices

1.5.1 Modeling of Fuel Cells

The behavior of fuel cells must be well-understood in order to make their successful use for different applications. It is important to obtain $V-I$ characteristics, also known as polarization characteristics, of fuel cells to understand how the output voltage and the output power of a fuel cell are affected as a result of load change at its output. It is also essential to understand their steady state as well as transient behavior. In DG applications, fuel cells may be subjected to fast load changes and hence, transient response of fuel cells over short and long-time periods must be properly studied in order to design proper controllers for fuel cell-based DG systems.

1.5.1.1 Analytical Modeling of Fuel Cells

In the literature, prior work has been reported to understand the dynamics of fuel cells. In [15] and [16], advantages of mechanistic modeling techniques and empirical modeling techniques are combined, and a parametric model predicting the performance of the PEM fuel cell is developed using a combination of mechanistic and empirical modeling techniques. These techniques were employed to determine the characteristics of the PEM fuel cell. The mechanistic model is developed by studying mass transport properties, thermodynamic equilibrium potentials, and overvoltages in the PEM fuel cell. The empirical model is developed by determining numerical parametric equations based on experimental data.

In [17], an isothermal, one-dimensional, steady state model of the PEM fuel cell with a 117 Nafion membrane is presented. The model calculates the distribution of water

through the PEM fuel cell. The model includes transport through the porous electrodes based on computed diffusivities and transport through the membrane electrolyte based on experimentally determined transport parameters.

Research reported in [18]-[27] focuses on developing mathematical models of the PEM fuel cell. The work is aimed at modeling the dynamic behavior of the PEM fuel cell using electrical circuits.

In [28], a small-signal model of the PEM fuel cell is proposed. The PEM fuel cell is modeled as a linear system by linearizing its dynamics around an operating point. The dynamic response of the linearized fuel cell system is obtained for small-perturbations of input variables.

The dynamic behavior SOFC is modeled in [29] and [30]. In [29], a physically based dynamic model for tubular SOFC is presented, based on electrochemical and thermodynamic characteristics of SOFC. The effect of temperature on the $V-I$ and $P-I$ characteristics of the SOFC is analyzed and model responses are obtained for constant fuel flow operating mode and constant fuel utilization operating mode. In [30], a simulation model of the SOFC-based power plant is created for use in a well-known power systems simulation package. The $V-I$ characteristics obtained by simulating the SOFC stack model and the safe operating limits for the SOFC-based power plant are identified. The steady state response of the plant to load current change is also studied.

Based on the above literature review, it is found that there exists an opportunity to improve the PEM fuel cell models reported in the literature. The detailed physical model of the PEM fuel cell which models important processes inside the PEM fuel cell system

can be developed. The formation of charge double-layer on the surface of the cathode inside the PEM fuel cell plays an important role in the dynamic behavior of the PEM fuel cell. However, most of the PEM fuel cell models reported in the literature do not take this effect into account. It is also noted that development of the PEM fuel cell system model in state space format would greatly help in designing sophisticated control techniques for the fuel cell system.

1.5.1.2 Nonparametric Modeling of Fuel Cells

The analytical PEM fuel cell models reviewed in the previous section make use of the first principles, and the model development is based on expressing various electrochemical and thermodynamic processes occurring inside the PEM fuel cell. The relationship between the PEM fuel cell's output voltage, stack temperature, and the input variables is highly nonlinear. As a result, these PEM fuel cell models are generally complex and mathematically quite involved. Also, developing precise models using this approach requires proper knowledge of various process parameters which are not always easily known. Moreover, it is fairly difficult to estimate these parameters for PEM fuel cell systems.

The use of these models for PEM fuel cell system studies could be ineffective unless right parameter values are known or determined. Compared to these conventional modeling techniques, a nonparametric modeling approach such as - neural network modeling – has the potential to provide certain unique modeling advantages.

The development of a neural network model does not require knowledge of the process parameters. The neural network model can learn from a set of input-output data

without the need of full specifications of the PEM fuel cell system. Once correctly trained, a neural network model can provide very good mapping between the output voltage, stack temperature, and the input variables of the PEM fuel cell. Also, unlike conventional techniques, neural network models do not need any linearization or assumptions in model development. In the conventional modeling approach, such assumptions and/or linearization may be necessary to reduce the overall complexity of the model. Also, since neural networks can map highly nonlinear relationships, without the necessity of determining the process parameters, the model development process can be relatively less tedious, which can help reduce the time required for developing the model.

In the literature, research on PEM fuel cell modeling using the neural network approach is reported. In [31], recurrent neural network models are proposed for on-board fuel cell power supply. However, the models are proposed only for different fuel cell load current frequencies without any further study of the dynamic behavior of the PEM fuel cell. In [32] and [33], the PEM fuel cell is modeled using feedforward neural networks, but the work does not provide any detailed analysis of PEM fuel cell systems using these models. In [34], the PEM fuel cell stack temperature is modeled using artificial neural networks. However, the model is not trained for PEM fuel cell stack voltage values.

Based on the above review, it is found that there exists an opportunity to improve recurrent neural network models of the PEM fuel cell reported in the literature. The model can be trained for the PEM fuel cell's output voltage and stack temperature values and then can be used to analyze the dynamic response of the PEM fuel cell system.

1.5.2 Control of Fuel Cell-based Distributed Generation (DG) Systems

Research on modeling and control of fuel cell-based DG systems is also reported in the literature.

Research in [35]-[40] is aimed at modeling fuel cell-based DG systems and developing control techniques for the systems. The work in [35] presents modeling and control of the PEM fuel cell-based DG system feeding to the AC grid with real and reactive power control capability. The dynamic models for the PEM fuel cell power plant and its power electronic interfacing are briefly described. The controller design methodologies for the power conditioning unit to control the power flow from the fuel cell power plant to the utility grid are presented. The simplified model of a three-phase inverter is presented by modeling the inverter as the first-order system. The PI controllers are designed for the dc/dc boost converter and also for the three-phase inverter. The load following analysis of the PEM fuel cell power plant is also performed.

The work in [36] focuses on developing a design methodology and a dynamic model of a combined PEM fuel cell and ultracapacitor-based energy source for stand-alone residential applications. It is shown that the combined use of the fuel cell and the ultracapacitor has the potential for better energy efficiency, reduction in cost of fuel cell technology and improvement in fuel usage. The power control strategies are also proposed for the combined fuel cell and ultracapacitor system. The system does not use a dc/dc boost converter in the power conditioning unit of the PEM fuel cell. The PI type controller is developed for the three-phase inverter.

Research in [37] focuses on the modeling, control and simulation of the PEM fuel cell-based power supply for residential applications. A PI type voltage and active power controllers are implemented by controlling the fuel input to fuel cell stack and by adjusting the inverter modulation index. The power quality issues are also evaluated based on the transformer connection type and harmonic content of the load for residential applications.

In [38] and [39], modeling and control of the solid oxide fuel cell (SOFC) based DG system is demonstrated. In [38], a comprehensive nonlinear dynamic model of SOFC is developed which can be used for dynamic and transient stability studies of SOFC based DG systems. A method for interfacing the proposed fuel cell models to a power system stability package is also developed. Research in [39] focuses on analyzing the dynamics of the distribution system that contain fuel cells and presents PI controller based techniques to enhance the stability of these systems.

Based on the above review, it is found that there exists an opportunity to improve the control methodologies applied to control the operation of the dc/dc converter, single-phase, and three-phase inverters used in the DG system. It is found that most of the control work reported to control the operation of the dc/dc converter and single-phase and three-phase inverters used in the DG system is oriented around PI/PID type control designs. There are few limitations of PI/PID type controllers used for the power converter and power inverter used in DG systems. These PI/PID type controllers can perform very well under linear and balanced linear loads. The properly tuned PI/PID controllers can deliver low THD output voltages to the linear and balanced linear loads. However, under

unbalanced linear loads and nonlinear loads, they cannot achieve a satisfactory performance and cannot control THD in the output voltage below the desired level (generally less than 5%).

In [12] and [13], the voltage and current control strategy for the three-phase inverter system is proposed. The control strategy is developed based on the robust servomechanism problem (RSP) theory proposed by Davison in [40]-[43]. The method combines the RSP voltage controller with the sliding mode current controller to satisfy the control objectives of the three-phase inverter system operating under linear as well as nonlinear loads. The effectiveness of this control strategy for the three-phase inverter system (three-phase, three-wire as well as three-phase, four-wire) is demonstrated in [12] and [13]. In this dissertation, this control strategy is formulated for single-phase inverter systems. The strategy is also further applied to the three-phase systems. The results of the control performance are compared with the results obtained by applying PI/PID controllers to single-phase and three-phase inverter systems.

The control of the dc/dc converter is performed by designing a sliding mode control law. The sliding mode control is designed based on an equivalent control method explained in [44]. The sliding mode control law determines the duty cycle of the converter and regulates the output voltage of the boost converter.

1.5.3 Modeling of Energy Storage Devices

Two most commonly used energy storage devices for DG systems are ultracapacitors and lead-Acid batteries. In certain cases, a combination of both is also preferred [36], [37]. Ultracapacitors have a very long life and generally do not need maintenance or extra

circuitry. However, they are expensive and their availability is limited [45]. Lead-acid batteries require maintenance and have a limited life span. However, they are widely available at a fairly low cost [45]. For the PEM fuel cell-based DG system considered in this work, the lead-acid battery is selected as the energy storage device primarily due to its moderate cost and wide availability compared to ultracapacitors.

In order to design the battery bank and simulate its charging, a model of the lead-acid battery is needed. The various battery models reported in [46]-[48], and [50] are reviewed and the dynamic model of the lead-acid battery proposed by *Jantharamin N. and Zhang, L.* in [51] is used to design the battery bank for the PEM fuel cell based DG system.

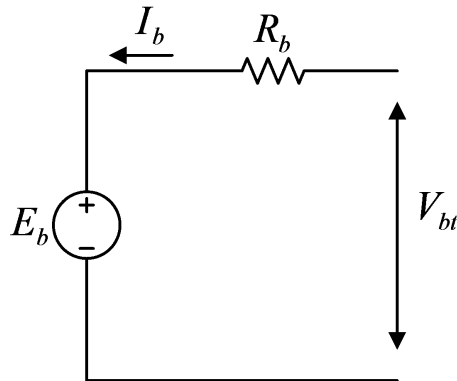


Figure 1.8 A Simple Battery Model

The simplest battery model is shown in Figure 1.8 [46], [51]. The model uses a simple resistor (R_b) connected in series with an ideal voltage source (E_b) to simulate the

battery behavior. The representation of a battery by such a model, although very convenient, is unrealistic, since the model parameters are considered constant, which is not true [46].

Another model reported in [47] is the Thevenin battery model shown in Figure 1.9. This model includes a parallel resistor-capacitor network ($R_{ov} \parallel C_{ov}$), in addition to the voltage source (E_b) connected in series with a resistor (R_b), to model overvoltage effects within the battery. However, again all model parameters are considered constant, and hence this model is inaccurate.

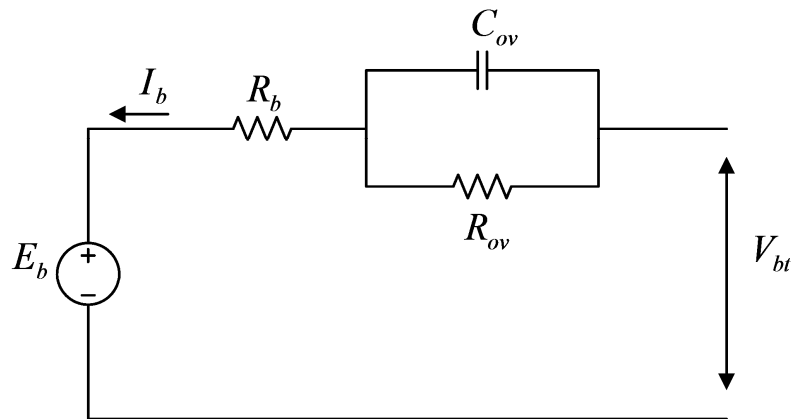


Figure 1.9 Thevenin Battery Model

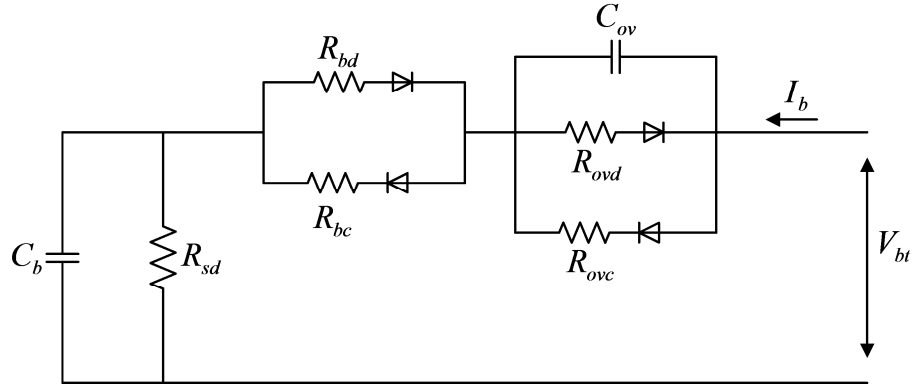


Figure 1.10 Improved Thevenin Battery Model

A further improvement in the Thevenin battery model is proposed in [48], as shown in Figure 1.10. The battery emf is represented by the voltage across the capacitor (C_b). The shunt resistor (R_{sd}) models self-discharge losses in the battery. The ohmic voltage drop and overvoltage effect are modeled by separate resistors as shown in Figure 1.10. During charging, the current flows through the ohmic resistance (R_{bc}) and overvoltage resistance (R_{ovc}), and when the battery is discharging, the current flows through (R_{bd}) and (R_{ovd}). Ideal diodes are connected in their respective paths to allow the current flowing through the desired resistances. All values of the model parameters are a function of the battery emf. However, in practice, the ohmic voltage drop and overvoltage effects can be identified together and polarization resistance can be described by a single equivalent resistance for each operating mode, which makes the battery model compact [48]-[50].

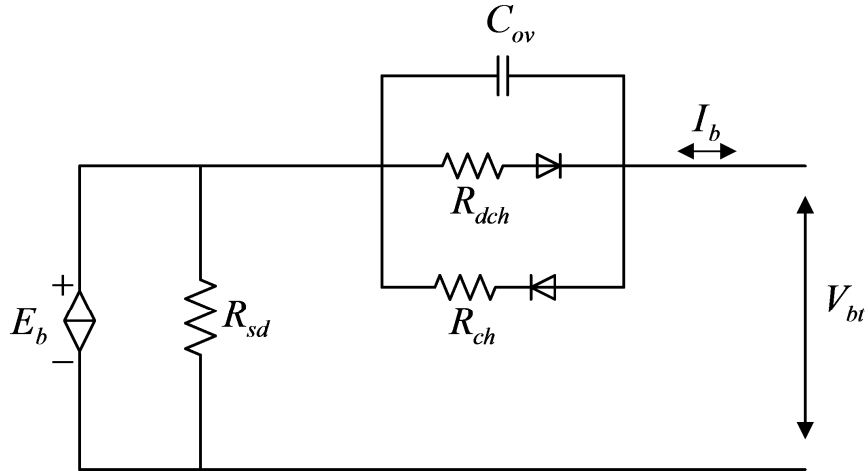


Figure 1.11 Dynamic Model of A Lead-Acid Battery

Figure 1.11 shows the dynamic model of lead-acid proposed by *Jantharamin N. and Zhang, L.* in [51]. The battery model shown in Figure 1.11, is the modification of the model shown in Figure 1.10. The ohmic voltage drop and overvoltage effects are identified together and polarization resistance is described by a single equivalent resistor (R_{ch} or R_{dch}) for each operating mode [51]. The charge stored in the battery can be given as an integral of the battery current (I_b) [46]. This battery model, shown in Figure 1.11, is used to design the battery bank for the PEM fuel cell-based DG system analyzed in this dissertation.

1.6 Research Objectives

In this dissertation, the performance of the PEM fuel cell-based DG system is analyzed by integrating different units of the DG system. In order to achieve the desired

performance of the DG system, suitable control techniques are designed for specific units of the PEM fuel cell-based DG system. An outline of the research objectives and their description is given below –

1.6.1 Development of the PEM fuel cell Model

The nonlinear state space model of a 500-W PEM fuel cell is developed based on physical processes inside the PEM fuel cell system. An open-circuit output voltage of the PEM fuel cell, irreversible voltage losses in the PEM fuel cell, formation of a charge double-layer in the PEM fuel cell, along with a mass balance and thermodynamic energy balance, in the PEM fuel cell system are modeled. The model is validated and then used to study the dynamic behavior of the PEM fuel cell [20]. The polarization curves ($V-I$ characteristics of the PEM fuel cell) are obtained for different values of input variables. The transient response of the PEM fuel cell model over short and long-time periods is analyzed. The behavior of the PEM fuel cell model is also studied under a resistive load.

The model of the PEM fuel cell is also proposed using a neural network approach and the nonlinear auto regressive model of a 500-W PEM fuel cell with external inputs (NARMAX) is developed using the recurrent neural network. It is shown that the nonlinear dynamics of the PEM fuel cell can be effectively modeled using a two-layer recurrent neural network. The data required to train the neural network model is generated by simulating a nonlinear state space model of the PEM fuel cell and the model is trained for the PEM fuel cell's output voltage and the stack temperature values. The effectiveness of the model is demonstrated by validating it with the experimental results of the *Avista Labs SR-12* (500-W) PEM fuel cell stack presented in [20]. A neural

network model is also used to analyze the dynamic behavior of the PEM fuel cell. Finally, the robustness of the a neural network model toward noise is investigated and the results are shown.

The formulation of a 5-kW PEM fuel cell array is demonstrated in MATLAB/Simulink by combining 2 (series) x 4 (parallel) 500-W fuel cells [35]. Each 500-W fuel cell used in the PEM fuel cell array has the rated current of 25 A, while, the PEM fuel cell array has the rated current of 100 A. The variation in the output voltage of the PEM fuel cell array is shown by obtaining $V-I$ characteristics.

1.6.2 Charging of the Lead-Acid Battery Bank from the PEM Fuel Cell Array

The sizing of the lead-acid battery bank, which is the energy storage element required for the DG system, is performed, and charging of the battery bank is simulated in MATLAB/Simulink. In order to design the battery bank and simulate its charging, a model of the dc/dc boost converter and a model of the lead-acid battery are presented. The parameters of the battery model are identified using curve fitting techniques and the battery model is validated with a 12 V, 4 Ah *Yuasa (NP4-12)* battery [51], [52]. The discharge characteristics of the battery model are studied and the model is then appropriately scaled to design the battery bank. The dc/dc boost converter is modeled based on the state space averaging technique proposed by *Middlebrook and Cuk* and a sliding mode control law is designed for the dc/dc boost converter to control its output voltage [44], [53].

1.6.3 Control of a Single-Phase Inverter

Control of the single-phase inverter system is demonstrated by applying two different control strategies to the single-phase inverter system operating under linear and nonlinear loads. The objective of the control design is to achieve low THD output voltage, fast transient response and asymptotic tracking of reference output voltage under linear and nonlinear loads minimizing the effect of harmonic frequencies. First, the PID control technique is used to control the operation of the single-phase inverter system and it is shown that the PID controller works very well for the linear loads and achieves an acceptable level of harmonic reduction. However, with the nonlinear loads, the PID controller does not achieve a satisfactory level of harmonic suppression. The second control technique – a discrete-time RSP control design combined with a discrete-time sliding mode control – eliminates this problem and achieves a satisfactory level of harmonic suppression in the presence of nonlinear loads [12]- [13],[40]-[43].

For both control techniques mentioned above, the controller structure is defined, necessary controller parameters are determined, and the simulation of a complete closed-loop system is performed in MATLAB/Simulink.

1.6.4 Control of a Three-Phase Inverter

The application of these control strategies is also extended to the three-phase inverter system operating under balanced linear loads, unbalanced linear loads, and nonlinear loads; and it is shown that the PID control technique works very well for balanced linear loads and achieves an acceptable level of harmonic reduction. However, with unbalanced linear loads and nonlinear loads, the PID controller cannot achieve a satisfactory level of

harmonic suppression. It is again shown that the second control technique – a discrete-time RSP control design combined with a discrete-time sliding mode control –eliminates this problem and achieves a satisfactory level of harmonic suppression in the presence of balanced linear loads, unbalanced linear loads, and nonlinear loads[12]- [13],[40]-[43].

1.7 Organization of the Dissertation

This dissertation is organized as follows: In Chapter 2, development of the nonlinear state space model of a 500-W PEM fuel cell-based on physical processes inside the PEM fuel cell system is performed. The dynamic behavior of the PEM fuel cell is analyzed using the model and the *V-I* Characteristics of the PEM fuel cell. The transient response of the model over short and long-time periods is analyzed, and the behavior of the model under a resistive load is shown.

In Chapter 3, an application of a neural network technique to model the behavior of the PEM fuel cell is demonstrated. The development of the two-layer recurrent neural network to model the nonlinear behavior of the PEM fuel cell system is shown. The model is used to analyze the dynamic response of the PEM fuel cell under different conditions.

In Chapter 4, sizing of the lead-acid battery bank, required for the PEM fuel cell-based DG system is demonstrated. The charging of the battery bank from the PEM fuel cell array is also explained. A sliding mode control law is designed to regulate the output of the dc/dc boost converter.

In Chapter 5, control of a single-phase and three-phase inverter, used in the DG system, is demonstrated. Two different control strategies are applied to these inverters

operating under linear and nonlinear loads. The performance of these inverters is compared for the applied control strategies.

Chapter 6 presents the conclusions of this dissertation, along with the suggestions for the future work, which may be performed based on the research presented in this dissertation.

CHAPTER 2

STATE SPACE MODELING OF PROTON EXCHANGE MEMBRANE FUEL CELL

2.1 Introduction

In this chapter, a nonlinear state space model of a 500-W proton exchange membrane (PEM) fuel cell is developed. An open-circuit output voltage of the PEM fuel cell, irreversible voltage losses in the PEM fuel cell, formation of charge double-layer in the PEM fuel cell, along with a mass balance and thermodynamic energy balance in the PEM fuel cell system are modeled. The model is simulated in MATLAB/Simulink, validated, and is then used to study the dynamic behavior of the PEM fuel cell. The polarization curves ($V-I$ characteristics of the PEM fuel cell) are obtained for different values of input variables. The transient response of the PEM fuel cell model over short and long-time periods is analyzed. Finally, the behavior of the PEM fuel cell model under a resistive load is studied.

2.2 Open-Circuit Output Voltage of the PEM Fuel Cell

The PEM fuel cell consists of a proton exchange membrane placed between two electrodes that are coated with platinum catalyst [54]. The hydrogen gas, extracted using a reformer from the hydrocarbon fuel or by electrolysis of water, is supplied at the anode.

Air, a source of oxygen, is supplied at the cathode. At the anode, hydrogen gas, in the presence of the platinum catalyst, is ionized into positively charged hydrogen ions and negatively charged electrons. The oxidation reaction at anode is [54]:

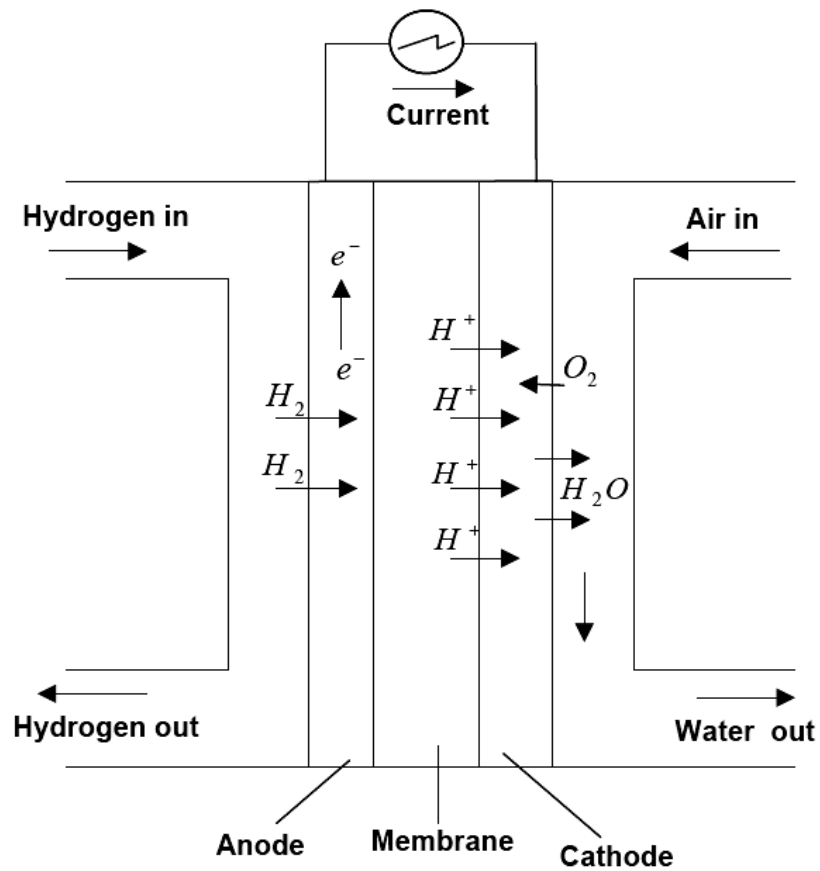


Figure 2.1 Working of the PEM Fuel Cell

The proton exchange membrane permits only positively charged hydrogen ions to flow from the anode to the cathode, as shown in Figure 2.1 [55]. The negatively charged electrons from the anode have to reach the cathode via external circuit. This process leads to the generation of electric current. At the cathode, electrons and protons combine with oxygen from the air to form water that flows out of the fuel cell. The reduction reaction at the cathode is [54]:



The reversible electric potential of one cell can be calculated from the change in Gibb's free energy as follows [54], [56]:

$$E^{Cell} = -\frac{\Delta G}{2F} \quad (2.3)$$

The change in Gibb's free energy can be given as [54]:

$$\Delta G = \Delta G^0 - RT \ln \left[\frac{P_{H_2} \cdot (P_{O_2})^{0.5}}{P_{H_2O}} \right] \quad (2.4)$$

Substituting equation (2.4) into (2.3), we get:

$$E^{Cell} = \left(-\frac{\Delta G^0}{2F} \right) + \frac{RT}{2F} \ln \left[\frac{P_{H_2} \cdot (P_{O_2})^{0.5}}{P_{H_2O}} \right]$$

$$\therefore E^{Cell} = E_0^{Cell} + \frac{RT}{2F} \ln \left[\frac{P_{H_2} \cdot (P_{O_2})^{0.5}}{P_{H_2O}} \right] \quad (2.5)$$

It should be noted that in equation (2.4) and (2.5), the partial pressures must either be expressed in 'atm' or in 'bar'.

The individual open-circuit output voltage of one cell is denoted by E^{Cell} . It can be assumed that parameters of individual cells can be lumped together to form the PEM fuel

cell stack [54]. Hence, the open-circuit output voltage of the PEM fuel cell can be given as:

$$V_{O,FC} = n_S \cdot E^{Cell}$$

$$\therefore V_{O,FC} = n_S \cdot E_0^{Cell} + \frac{n_S RT}{2F} \ln \left[\frac{P_{H_2} \cdot (P_{O_2})^{0.5}}{P_{H_2O}} \right] \quad (2.6)$$

2.3 Irreversible Voltage Losses in the PEM Fuel Cell

The actual output voltage of the PEM fuel cell at normal operating conditions is determined by irreversible voltage losses, also known as polarization, which exist within the PEM fuel cell [54]. Three types of voltage losses exist: activation losses, ohmic losses, and concentration losses.

2.3.1. Activation Losses

The governance of sluggish electrode kinetics by the rate of electrochemical reaction at an electrode surface gives rise to activation losses in the PEM fuel cell [54]. These losses are dominant at low current density (i.e. at the beginning of $V-I$ characteristic curve of the PEM fuel cell). The activation losses for a single PEM fuel cell stack can be modeled based on the Tafel equation, and an empirical equation of activation voltage loss as [15], [20], [54]:

$$V^{Act} = \frac{RT}{2F} \ln \left(\frac{I}{I_d} \right) = a_0 + T \cdot [a + b \ln(I)] \quad (2.7)$$

The term $(a_0 + aT)$ represents the temperature-dependent voltage loss, and the term $[T \cdot b \cdot \ln(I)]$ represents the activation voltage loss, based on both current and temperature.

The equivalent activation resistance R^{Act} corresponding to the activation voltage loss can be found by dividing the term $[T.b.\ln(I)]$ in equation (2.7) by I .

2.3.2 Ohmic Losses

The ohmic losses are due to the ohmic resistance of the PEM fuel cell that includes the resistance of the anode and cathode due to imperfections in the electrode manufacturing and the resistance of the polymer electrolyte membrane to the movement of ions [57]. The ohmic resistance of the PEM fuel cell can be given as:

$$R^O = R^A + R^C + R^M \quad (2.8)$$

The ohmic voltage loss for a single PEM fuel cell stack can be given as [20]:

$$V^O = I.R^O = V_A^O + V_C^O + V_M^O \quad (2.9)$$

The electrode resistances depend on the stack current and temperature, and hence the ohmic resistance of the PEM fuel cell can also be calculated as [20]:

$$R^O = R_c^O + K_I.I + K_T.T \quad (2.10)$$

2.3.3 Concentration Losses

The concentration losses exist due to the formation of concentration gradients of reactants at the surface of the electrodes [57]. The consumption of more fuel reduces the concentrations of hydrogen and oxygen at various points in the PEM fuel cell gas channels, and increases the concentrations of these reactants at the input of the stack. The concentration losses for a single PEM fuel cell stack can be given as [56]:

$$V^{Conc} = -\frac{RT}{eF} \ln\left(1 - \frac{I}{I_L}\right) \quad (2.11)$$

The equivalent resistance R^{Conc} corresponding to the concentration voltage loss can be found by dividing equation (2.11) by I . Also, the limiting current of the PEM fuel cell is determined by the rate of consumption of fuel and rate of fuel supply. Hence, concentration losses grow significant at higher currents, when fuel is consumed at a higher rate (i.e. at the end of the $V-I$ characteristics of the PEM fuel cell).

Hence, the actual output voltage of the PEM fuel cell at normal operating conditions is given by subtracting the voltage losses from the open-circuit output voltage of the PEM fuel cell as follows:

$$V_{fc} = V_{O,FC} - n_s \cdot (V^{Act} + V^O + V^{Conc}) \quad (2.12)$$

2.4 Humidification in the PEM Fuel Cell

In the PEM fuel cell, conduction of the hydrogen ions through the polymer membrane depends on the membrane humidity. The ohmic resistance of the membrane (R^M) increases, as the membrane dries out [54]. Hence, it is essential that the membrane remains humidified for an efficient operation of the PEM fuel cell. Therefore, the hydrogen gas and air are passed through the humidifier before reaching the electrodes. The relative humidity at the anode and cathode of the PEM fuel cell can be given as [54]:

$$\phi_a = \frac{(P_{H_2O})_{in}^a}{P_{H_2O}^{Sat}}, \quad \phi_c = \frac{(P_{H_2O})_{in}^c}{P_{H_2O}^{Sat}}$$

The total vapor transfer through the polymer membrane can be given as [11]:

$$(m_v)_M = M_v \cdot A_s \cdot n_s \left(\frac{n_d I_d}{F} - \frac{\phi_c - \phi_a}{t_m} \right) \quad (2.13)$$

2.5 Mass Balance and Thermodynamic Energy Balance in the PEM Fuel Cell

The net mole flow rate of an oxygen at the cathode is the difference between the mole flow rate of oxygen coming inside the cell and mole flow rate of oxygen going outside the cell. The flow of oxygen and hydrogen in the PEM fuel cell cannot follow changes in the load instantly, and there exists a time lag between the change in the load current, and flow of oxygen and hydrogen [54].

The net mole flow rate of oxygen at the cathode can be given as [20], [54]:

$$\frac{d(m_{O_2})_{net}}{dt} = \frac{1}{\lambda_C} \left[\frac{I}{4F} - (m_{O_2})_{net} \right]$$

Let $x_1 = (m_{O_2})_{net}$

$$\Rightarrow \dot{x}_1 = \left(\frac{-1}{\lambda_C} \right) x_1 + \left(\frac{1}{4 \cdot \lambda_C \cdot F} \right) I \quad (2.14)$$

Similarly, net mole flow rate of hydrogen at the anode can be given as [20], [54]:

$$\frac{d(m_{H_2})_{net}}{dt} = \frac{1}{\lambda_A} \left[\frac{I}{2F} - (m_{H_2})_{net} \right]$$

Let $x_2 = (m_{H_2})_{net}$

$$\Rightarrow \dot{x}_2 = \left(\frac{-1}{\lambda_A} \right) x_2 + \left(\frac{1}{2 \cdot \lambda_A \cdot F} \right) I \quad (2.15)$$

The material conservation of water can be given by subtracting the rate of net flow water vapor across the cell from the rate of generation of water in the cell [28], [54].

$$\frac{d(m_{H_2O})_{net}}{dt} = \frac{1}{\lambda_C} \left[\frac{I}{2F} - (m_{H_2O})_{net} \right]$$

Let $x_3 = (m_{H_2O})_{net}$

$$\Rightarrow \dot{x}_3 = \left(\frac{-1}{\lambda_c} \right) x_3 + \left(\frac{1}{2 \cdot \lambda_c \cdot F} \right) I \quad (2.16)$$

Let $x_4 = T, x_5 = P_{H_2}, x_6 = P_{O_2}, x_7 = P_{H_2O}$

The dynamic equation of the partial pressure of hydrogen can be written based on an ideal gas law $P.V = n.R.T$ as [20], [28]- [29]:

$$\frac{dP_{H_2}}{dt} = \left(\frac{RT}{V_a} \right) \cdot (m_{H_2})_{in} - \left(\frac{RT}{V_a} \right) \cdot (m_{H_2})_{out} - \left(\frac{RT}{V_a} \right) \cdot \frac{I}{2F} \quad (2.17)$$

$(m_{H_2})_{in}$ and $(m_{H_2})_{out}$ can be expressed in terms of the channel input pressure of hydrogen as [20],[28]-[29]:

$$(m_{H_2})_{in} = \frac{(m_{H_2O})_{in}^a}{(P_{H_2O})_{in}^a} \cdot u_{P_A}, \quad (m_{H_2})_{out} = (m_{H_2})_{in} \cdot \frac{(2x_5 - u_{P_A})}{u_{P_A}} \quad (2.18)$$

Substituting equation (2.18) into equation (2.17) and solving further, we get,

$$\dot{x}_5 = 2 \cdot \theta_1(x_4) \cdot u_{P_A} - 2 \cdot \theta_1(x_4) \cdot x_5 - \theta_2(x_4) \cdot I \quad (2.19)$$

$$\text{where, } \theta_1(x_4) = \left[\frac{R \cdot (m_{H_2O})_{in}^a \cdot x_4}{V_a \cdot (P_{H_2O})_{in}^a} \right], \quad \theta_2(x_4) = \left(\frac{R x_4}{2 V_a F} \right)$$

Similarly, the dynamic equation of the partial pressure of oxygen can be given as:

$$\dot{x}_6 = 2 \cdot \theta_3(x_4) \cdot u_{P_c} - 2 \cdot \theta_3(x_4) \cdot x_6 - \theta_4(x_4) \cdot I \quad (2.20)$$

$$\text{where, } \theta_3(x_4) = \left[\frac{R \cdot (m_{H_2O})_{in}^c \cdot x_4}{V_c \cdot (P_{H_2O})_{in}^c} \right], \quad \theta_4(x_4) = \left(\frac{R x_4}{4 V_c F} \right)$$

The rate of change of the partial pressure of water depends on the net flow rate of water across the cell and the rate of generation of water during the reaction at the cathode [20], [28], [29]. It can be given in state space form as:

$$\dot{x}_7 = 2 \cdot \theta_5(x_7) \cdot x_4 + 2 \cdot \theta_4(x_4) \cdot I \quad (2.21)$$

$$\text{where, } \theta_5(x_7) = \left[\frac{R.(m_{H_2O})_{in}^c.(P_{H_2O}^{in} - x_7)}{V_c.(P_{H_2O})_{in}^c} \right]$$

As electrochemical reaction takes place in the PEM fuel cell, temperature of the PEM fuel cell assembly increases [58]. The net increase in the temperature of the PEM fuel cell assembly can be given by equation (2.22) as [58]:

$$\text{Let } x_8 = Q_C, x_9 = Q_E, x_{10} = Q_L$$

$$\therefore \dot{x}_4 = \frac{1}{M_{fc} C_{fc}} (\dot{x}_8 - \dot{x}_9 - \dot{x}_{10}) \quad (2.22)$$

The generation of heat during an electrochemical reaction is a function of the change in Gibbs's free energy and the rate of consumption of molar mass of hydrogen during the reaction [58].

$$\begin{aligned} \therefore \dot{x}_8 &= \Delta G \left(\frac{n_s I}{2F} \right) \\ \Rightarrow \dot{x}_8 &= \theta_6(x_4, x_5, x_6, x_7).I \end{aligned} \quad (2.23)$$

$$\text{where, } \theta_6(x_4, x_5, x_6, x_7) = \left[\frac{n_s \Delta G^0}{2F} - \frac{n_s R.x_4}{2F} \ln \left(\frac{x_5.x_6^{0.5}}{x_7} \right) \right]$$

The generation of heat due to an electrical output power in the PEM fuel cell depends on the output voltage and stack current of the PEM fuel cell [58].

$$\begin{aligned} \therefore \dot{x}_9 &= [V_{fc}] . I \\ \Rightarrow \dot{x}_9 &= \theta_7(x_4, x_5, x_6, x_7).I \end{aligned} \quad (2.24)$$

$$\text{where, } \theta_7(x_4, x_5, x_6, x_7) = n_s \cdot \left[E_0^{Cell} + \frac{R.x_4}{2F} \ln \left(\frac{x_5.x_6^{0.5}}{x_7} \right) - V^{Act} - V^{Conc} - V^O \right]$$

The heat loss due to the air convection can be given by equation (2.25) as [58]:

$$\frac{dQ_L}{dt} = (T - u_{T_R}) h_S n_S A_S$$

$$\therefore \dot{x}_{10} = [h_S n_S A_S] x_4 - [h_S n_S A_S] u_{T_R} \quad (2.25)$$

Substituting equations (2.23), (2.24) and (2.25) into equation (2.22), we can write,

$$\dot{x}_4 = \left[\frac{-h_S n_S A_S}{M_{fc} C_{fc}} \right] x_4 - \theta_8(x_4, x_5, x_6, x_7) \cdot I + \left[\frac{h_S n_S A_S}{M_{fc} C_{fc}} \right] u_{T_R} \quad (2.26)$$

$$\text{where, } \theta_8(x_4, x_5, x_6, x_7) = n_S \cdot \left[\frac{2E_0^{Cell}}{M_{fc} C_{fc}} + \frac{R \cdot x_4}{FM_{fc} C_{fc}} \ln \left(\frac{x_5 \cdot x_6^{0.5}}{x_7} \right) - V^{Act} - V^{Conc} - V^O \right]$$

2.6 Formation of a Charge Double Layer in the PEM Fuel Cell

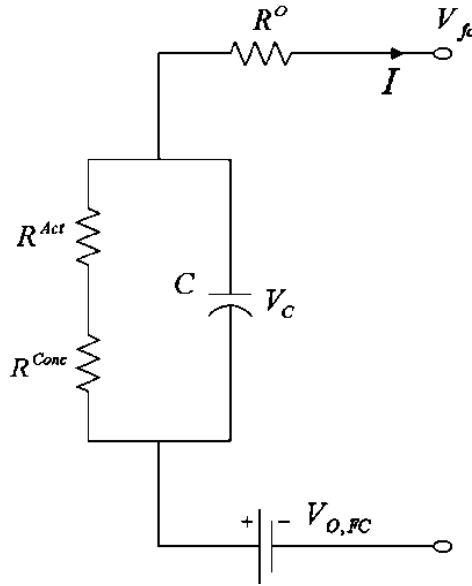


Figure 2.2 Formation of a Charge Double Layer in the PEM Fuel Cell

In the PEM fuel cell, due to the presence of polymer membrane, electrons (e^-) from the anode flow towards the cathode via an external circuit, while, positive hydrogen ions (H^+) reach the cathode through the polymer membrane. As a result, two charged layers of opposite polarities are formed at the cathode. This charge double-layer can store an electrical charge, and behaves like a capacitor [54]. Hence, voltage formed due to this charge double-layer will take certain time to respond to sudden change in the current. Therefore, in the PEM fuel cell, when the current is increased by sudden increase in the load, the output voltage shows an immediate drop due to the drop across R^o of the PEM fuel cell, but then the voltage reaches its new value in an exponential manner, due to the capacitance of the charge double-layer [20],[54]. The electric charge formed at the cathode can be modeled by the capacitor as shown in Figure 2.2 [54].

The capacitance due to the charge double-layer effect is a function of the surface area of the cathode A_s , the distance between the two charged layers dl , and the electrical permittivity ε . The value of the capacitance is given as [54]:

$$C = \varepsilon \cdot \left(\frac{A_s}{dl} \right) \quad (2.27)$$

The voltage across the capacitor is given as [54]:

$$V_C = \left(I - C \frac{dV_C}{dt} \right) (R^{Act} + R^{Conc})$$

$$\text{Let } x_{11} = V_C \Rightarrow \dot{x}_{11} = \left[\frac{-1}{C(R^{Act} + R^{Conc})} \right] x_{11} + \left[\frac{1}{C} \right] I \quad (2.28)$$

The effect of formation of the charge double-layer can be incorporated in the output voltage of the PEM fuel cell. Hence, the output voltage equation given by equation (2.12) can be rewritten as:

$$V_{fc} = \left[n_s \cdot E_0^{Cell} + \frac{n_s R \cdot x_4}{2F} \ln \left(\frac{x_5 \cdot x_6^{0.5}}{x_7} \right) - n_s (a_0 + ax_4) - n_s \cdot x_{11} - (n_s R^o) I \right] \quad (2.29)$$

Based on equations (2.14)-(2.29), an overall state space model of the PEM fuel cell system can be given as:

$$\begin{aligned} \dot{x}(t) &= A(\theta) \cdot x(t) + B(\theta) \cdot u(t) + G(\theta) \cdot w(t) \\ y(t) &= C(\theta) \cdot x(t) + v(t) \end{aligned} \quad (2.30)$$

where, $x(t)$ represents the system states, $y(t)$ represents the system output, $u(t)$ is the control input, $w(t)$ is the disturbance input, which is the load current, $v(t)$ is the measurement noise. The description of vectors $x(t)$, $u(t)$, $y(t)$ along with matrices A , B , C , G , and the state-dependent parameter vector θ are given below:

$$\begin{aligned} x &= \left[(m_{O_2})_{net} \quad (m_{H_2})_{net} \quad (m_{H_2O})_{net} \quad T \quad P_{H_2} \quad P_{O_2} \quad P_{H_2O} \quad Q_C \quad Q_E \quad Q_L \quad V_C \right]^T \\ u &= \left[u_{P_A} \quad u_{P_C} \quad u_{T_R} \right]^T, \quad w = [I] \end{aligned}$$

$$A = \begin{bmatrix} \frac{-1}{\lambda_c} & 0 & 0 & 0 & 0 & 0 & 0_{1 \times 4} & 0 \\ 0 & \frac{-1}{\lambda_A} & 0 & 0 & 0 & 0 & 0_{1 \times 4} & 0 \\ 0 & 0 & \frac{-1}{\lambda_c} & 0 & 0 & 0 & 0_{1 \times 4} & 0 \\ 0 & 0 & 0 & \left(\frac{-h_S \cdot n_S \cdot A_S}{M_{fc} \cdot C_{fc}} \right) & 0 & 0 & 0_{1 \times 4} & 0 \\ 0 & 0 & 0 & 0 & -2\theta_1(x_4) & 0 & 0_{1 \times 4} & 0 \\ 0 & 0 & 0 & 0 & 0 & -2\theta_3(x_4) & 0_{1 \times 4} & 0 \\ 0 & 0 & 0 & 2\theta_5(x_7) & 0 & 0 & 0_{1 \times 4} & 0 \\ 0_{2 \times 1} & 0_{2 \times 4} & 0_{2 \times 1} \\ 0 & 0 & 0 & (h_S \cdot n_S \cdot A_S) & 0 & 0 & 0 & 0 \\ 0 & 0 & 0 & 0 & 0 & 0 & 0_{1 \times 4} & \left(\frac{-1}{C(R^{Act} + R^{Conc})} \right) \end{bmatrix}$$

$$\theta = [\theta_1(x_4) \quad \theta_2(x_4) \quad \theta_3(x_4) \quad \theta_4(x_4) \quad \theta_5(x_7) \quad \theta_6(x_4, x_5, x_6, x_7)$$

$$\theta_7(x_4, x_5, x_6, x_7) \quad \theta_8(x_4, x_5, x_6, x_7)]^T$$

$$G = \begin{bmatrix} \left(\frac{1}{4\lambda_c F} \right) & \left(\frac{1}{2\lambda_A F} \right) & \left(\frac{1}{2\lambda_c F} \right) & -\theta_8(x_4, x_5, x_6, x_7) & -\theta_2(x_4) \\ -\theta_4(x_4) & 2\theta_4(x_4) & \theta_6(x_4, x_5, x_6, x_7) & \theta_7(x_4, x_5, x_6, x_7) & 0 & \frac{1}{C} \end{bmatrix}^T$$

2.7 Simulation of the PEM Fuel Cell Model

A nonlinear state space model of the PEM fuel cell, developed in sections 2.2 to 2.6, is simulated in MATLAB/Simulink. The main block diagram of the Simulink implementation of the PEM fuel cell model is shown in Figure 2.3. The parameters of the PEM fuel cell model used in the simulation are listed in Table 2.1.

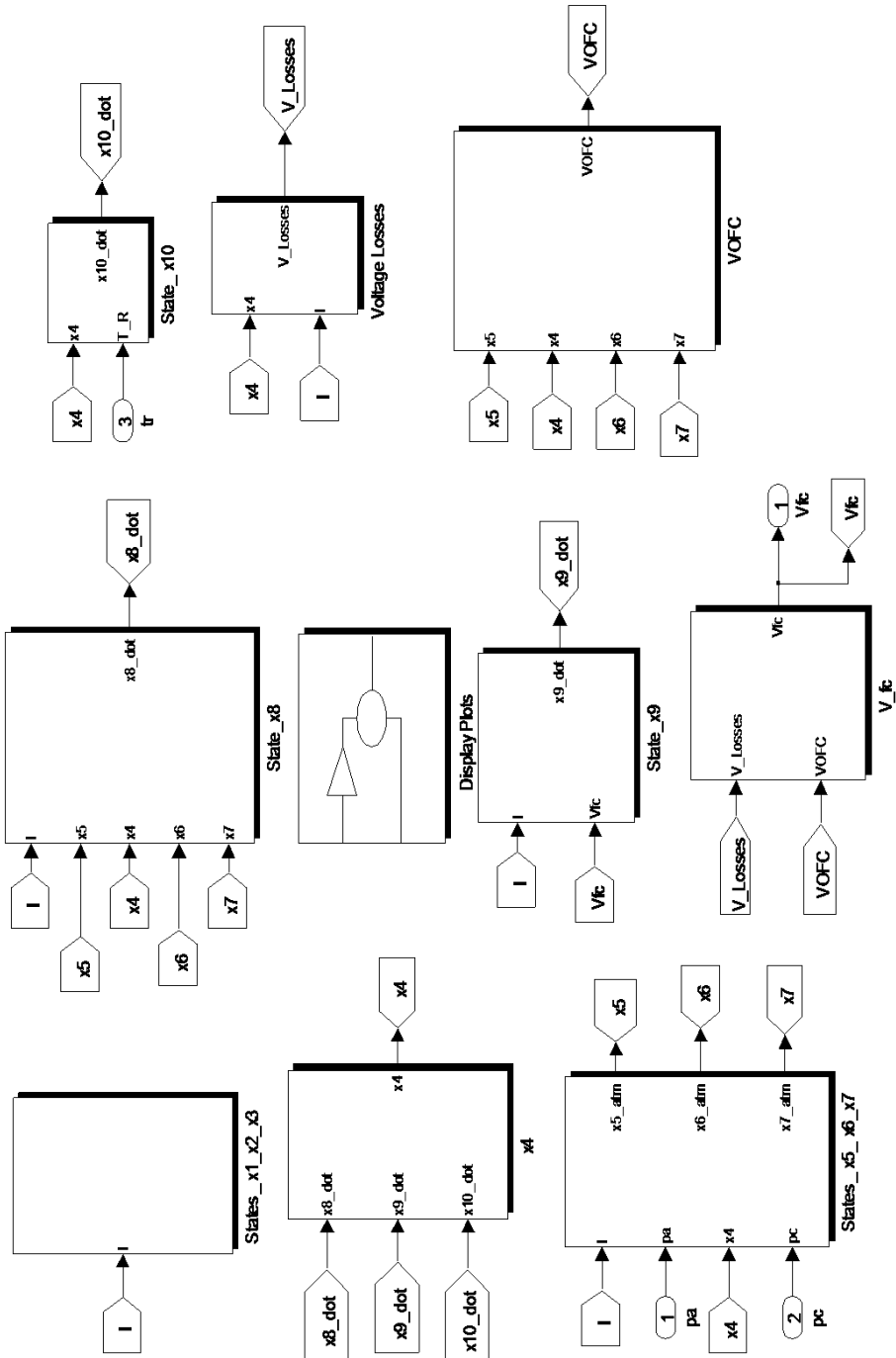


Figure 2.3 Implementation of the PEM Fuel Cell Model in MATLAB/Simulink

The parameters of the PEM fuel cell model are given below in Table 2.1 [3], [8], [17].

$A_s = 3.2 \cdot 10^{-2} \text{ m}^2$	$M_{fc} = 44 \text{ kg}$
$a = -3.08 \cdot 10^{-3} \text{ V/K}$	$(m_{H_2O})_{in}^a = 8.614 \cdot 10^{-5} \text{ mol/s}$
$a_0 = 1.3697 \text{ V}$	$(m_{H_2O})_{in}^c = 8.614 \cdot 10^{-5} \text{ mol/s}$
$b = 9.724 \cdot 10^{-5} \text{ V/K}$	$n_s = 48$
$C_{fc} = 500 \text{ J/(molK)}$	$(P_{H_2O})_{in} = 2 \text{ atm}$
$C = 10 \text{ F}$	$R = 8.31 \text{ J/(molK)}$
$E_0^{Cell} = 1.23 \text{ V}$	$R_c^0 = 0.28 \text{ } \Omega$
$e = 2$	$V_a = 10^{-3} \text{ m}^3$
$F = 96487 \text{ C/mol}$	$V_c = 10^{-3} \text{ m}^3$
$\Delta G^0 = 237.2 \cdot 10^3 \text{ J/mol}$	$\lambda_A = 60 \text{ s}$
$h_s = 37.5 \text{ W/(m}^2 \cdot \text{K)}$	$\lambda_c = 60 \text{ s}$
$K_I = 1.87 \cdot 10^{-3} \text{ } \Omega/\text{A}$	$(P_{H_2O})_{in}^a = 1 \text{ atm}$
$K_T = -2.37 \cdot 10^{-3} \text{ } \Omega/\text{K}$	$(P_{H_2O})_{in}^c = 1 \text{ atm}$

Table 2.1 Parameters of the PEM Fuel Cell Model

2.8 Simulation Results

2.8.1 V-I Characteristics of the PEM Fuel Cell Model

To obtain the V-I characteristics of the PEM fuel cell, the model is simulated for 2720 seconds for the following values of input variables:

$u_{P_A} = 2 \text{ atm}$, $u_{P_C} = 1 \text{ atm}$, $u_{T_R} = 308 \text{ K}$. The V-I characteristics obtained by simulation are shown in Figure 2.4.

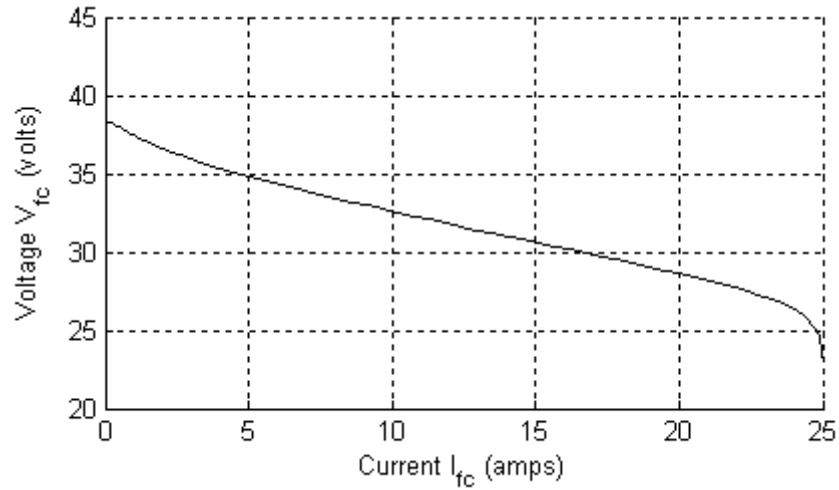


Figure 2.4. V-I characteristics of the PEM Fuel Cell Model

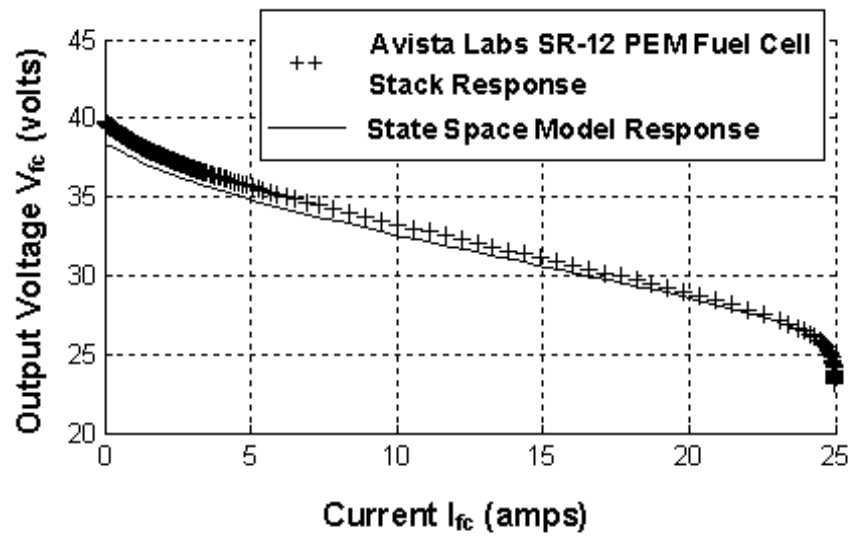


Figure 2.5 Validation of the PEM Fuel Cell Model

The simulation results obtained in Figure 2.4 are validated with the experimental results of the *Avista Labs SR-12* (500W) PEM fuel cell stack given in [20]. Figure 2.5 shows the model validation, and the validation results show close match.

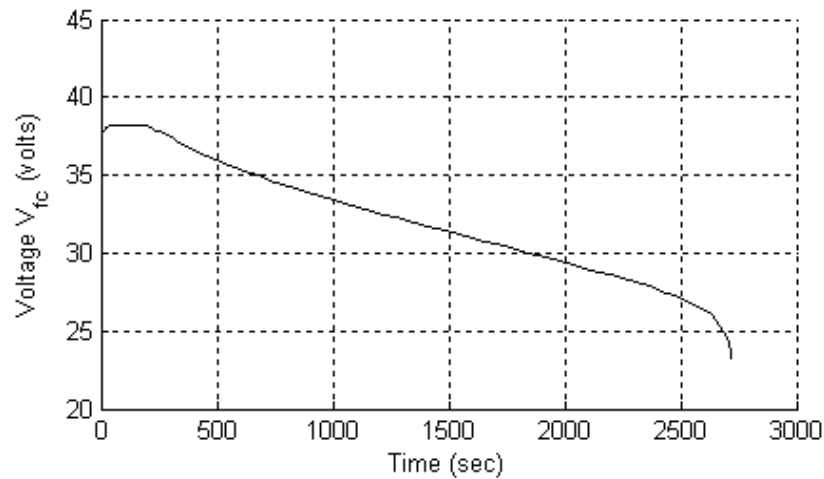


Figure 2.6 Output Voltage Response of the PEM Fuel Cell Model

The output voltage response of the PEM fuel cell model is shown in Figure 2.6. The response is obtained by varying the current from 1A to 25 A in steps of 0.4 A every 40 seconds, over a total simulation period of 2720 seconds. The output voltage decreases from about 38 volts to 23 volts.

The temperature response of the PEM fuel cell model is shown in Figure 2.7. As more current is drawn from the PEM fuel cell stack, the electron activity at the surface of the electrodes increases. This results in an increase in the PEM fuel cell stack

temperature. It can be seen in Figure 2.7 that the stack temperature rises from 308 K to 320 K, as more current is drawn from the PEM fuel cell.

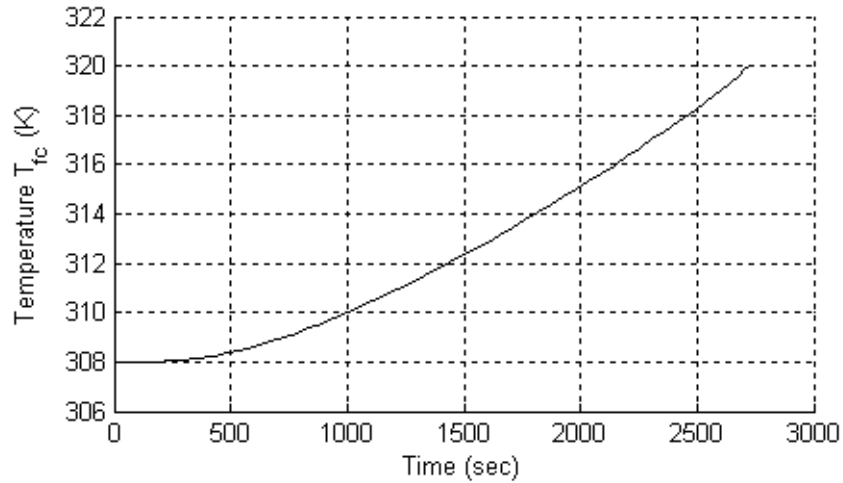


Figure 2.7 Temperature Response of the PEM Fuel Cell Model

The $P-I$ characteristics of the PEM fuel cell model are shown in Figure 2.8. The maximum output power is obtained at a point close to the rated current of the fuel cell (25A), but not exactly at the rated current. The PEM fuel cell goes in the concentration region near the rated current value, wherein the output power decreases with the increasing load current due to the potential decrease in the PEM fuel cell's output voltage [11], [20].

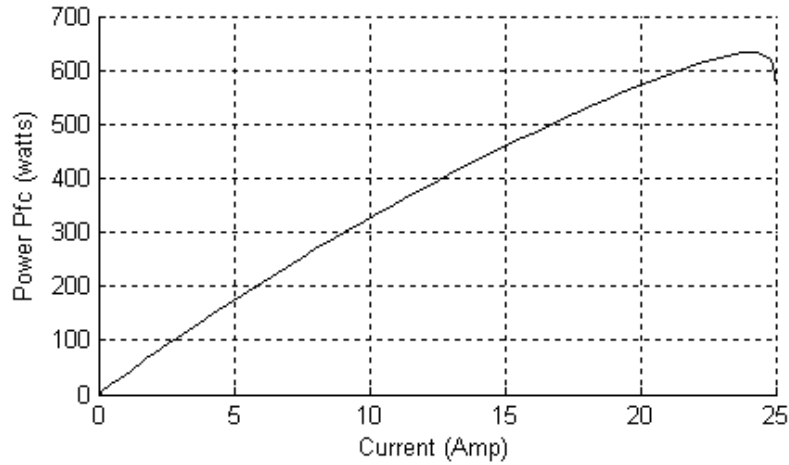


Figure 2.8 P - I Characteristics of the PEM Fuel Cell Model

2.8.2 Polarization Curves of the PEM Fuel Cell Model for Different Values of Input Variables

The PEM fuel cell model is subjected to different values of input variables in order to study their effect on the V - I characteristics, the output voltage of the PEM fuel cell, and voltage losses.

2.8.2.1 V - I Characteristics of the PEM Fuel Cell Model for Increasing Values of the Anode Channel Pressure (u_{P_A})

Figure 2.9 shows the V - I characteristics of the PEM fuel cell model for increasing values of u_{P_A} . The characteristics are obtained for: $u_{P_A} = 2$ atm, 10 atm, 30 atm, 50 atm. The other two input variables u_{P_C} and u_{T_R} are kept constant at 1 atm and 308 K, respectively. As u_{P_A} is increased, the partial pressure of hydrogen at the anode increases.

Hence, the output voltage of the PEM fuel cell increases. This increase in the output voltage reduces voltage losses in the PEM fuel cell. Thus, voltage losses in the PEM fuel cell can be reduced by operating the PEM fuel cell at higher values of u_{P_A} . It can be seen from Figure 2.9, that the losses are smaller for the higher values of u_{P_A} .

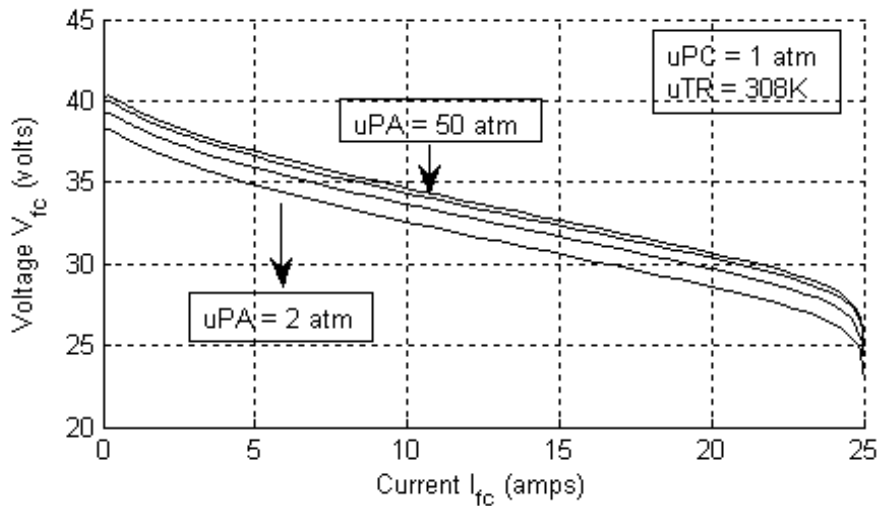


Figure 2.9 V - I Characteristics of the PEM Fuel Cell Model for Increasing u_{P_A}

2.8.2.2 V - I Characteristics of the PEM Fuel Cell Model for Increasing Values of the Cathode Channel Pressure (u_{P_C})

Figure 2.10 shows the V - I characteristics of the PEM fuel cell model for increasing values of u_{P_C} . Physically, u_{P_C} can be increased by compressing the air or oxygen at the higher pressure before supplying it to the cathode. The characteristics are obtained for:

$u_{p_c} = 1 \text{ atm}, 10 \text{ atm}, 30 \text{ atm}, 50 \text{ atm}$. The other two input variables u_{p_A} and u_{T_R} are kept constant at 2 atm and 308 K, respectively. As u_{p_c} is increased, the partial pressure of oxygen at the cathode increases. It increases the output voltage of the PEM fuel cell. This increase in the output voltage, reduces voltage losses. I.e. for higher values of u_{p_c} , voltage losses are smaller. Hence, voltage losses in the PEM fuel cell can also be reduced by operating the PEM fuel cell at higher values of u_{p_c} .

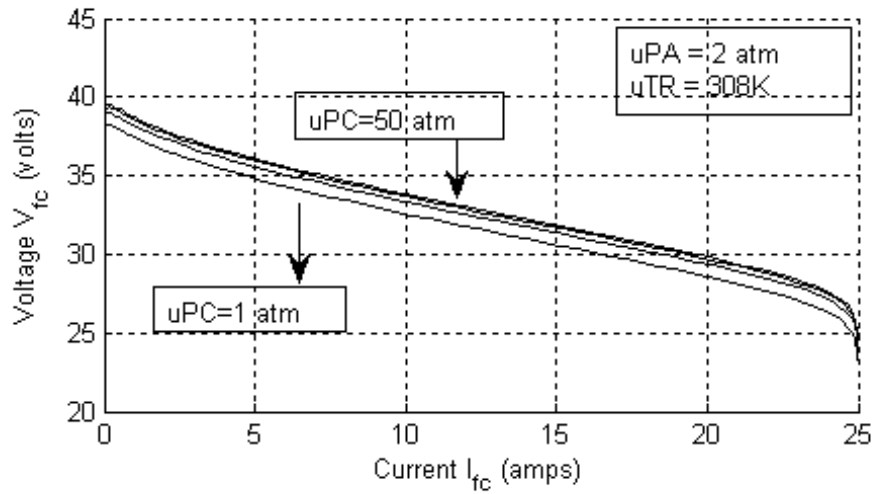


Figure 2.10 V - I Characteristics of the PEM Fuel Cell Model for Increasing u_{p_c}

2.8.3 Transient Response of the PEM Fuel Cell Model

2.8.3.1 Transient Response of the PEM Fuel Cell Model over a Short-Time Period

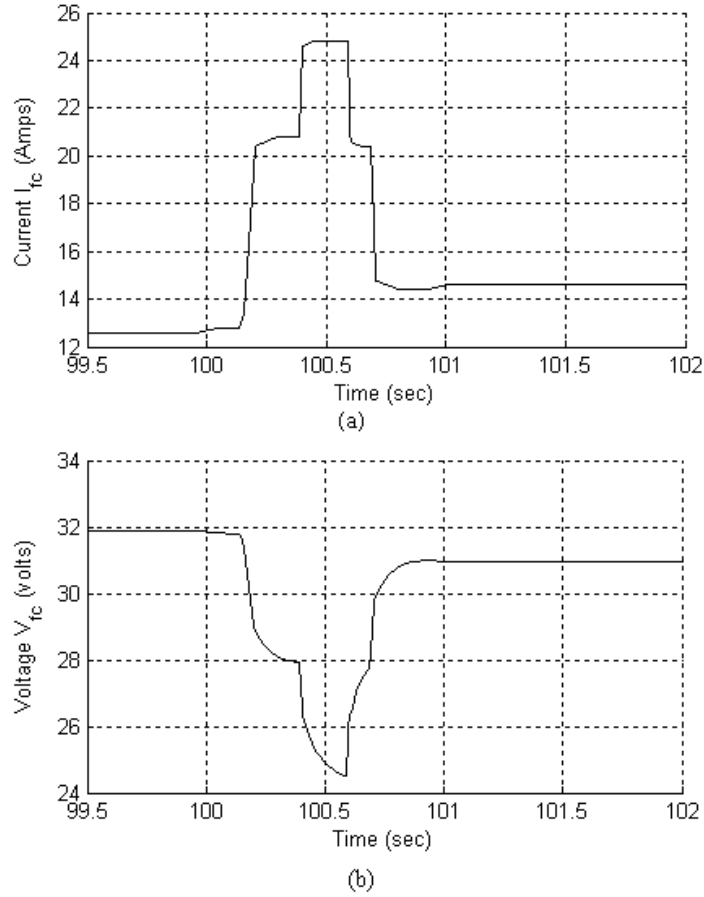


Figure 2.11 Transient Response of the PEM Fuel Cell Model over a Short-time Period
(**Top:** Stack current, **Bottom:** Output Voltage)

A transient response of the PEM fuel cell model over a short-period is obtained by simulating the model for following values of input variables: $u_{P_A} = 5$ atm, $u_{P_C} = 5$ atm, $u_{T_R} = 308$ K. The load is changed in the steps over a small time period, and the response

of the model is observed. Figures 2.11(a) and (b) show the plots of the change in load current, and corresponding change in the output voltage of the PEM fuel cell model, respectively. It can be seen that as the load is increased, the output voltage drops, and vice-versa. However, the output voltage does not reach a new value instantly. As the load is increased, the voltage drops to a certain value immediately but from there it reaches to its new value in an exponential manner. This is due to the capacitance of the charge double-layer formed on the surface of the cathode.

Time constant of the first-order equation (2.29) can be given as $\tau = C(R^{Act} + R^{Conc})$ [54]. In the PEM fuel cell, the surface area of the cathode is greater than the distance between two charged layers, and hence, according to equation (2.28), the value of the capacitance C is high. Moreover, the values of R^{Act} and R^{Conc} are quite small when the PEM fuel cell operates in the linear region [54]. Therefore, the transient response of the PEM fuel cell over a short-time period will be largely determined by the value of the capacitance C . Higher the value of C , higher will be τ , and longer it will take for the voltage to reach its new value.

2.8.3.2 Transient Response of the PEM Fuel Cell Model over a Long-Time Period

A transient response of the PEM fuel cell model over a long-time period is shown in Figure 2.12. The figure shows the output voltage response of the model. It is observed that, as the load current is reduced, the output voltage increases to a certain value, but from there, it reaches to its final value in few hundred seconds. When the load current is increased, the output voltage drops to a certain value, and again takes few hundred seconds to reach to its final value. This is due to the higher thermodynamic time constant,

as well as due to the air and hydrogen flow delays inside the PEM fuel cell. They both can vary from few seconds to even few minutes [11], [20]. As seen from Figure 2.12, the temperature of the stack takes certain time to change as the electrochemical reaction proceeds in the PEM fuel cell. The stack temperature does not rise instantly. Also, the hydrogen and air flow to the anode and cathode cannot instantly follow the changes in the load [20]. Therefore, the thermodynamic time constant and flow delays largely determine the transient response of the PEM fuel cell over a long-time period [11], [20].

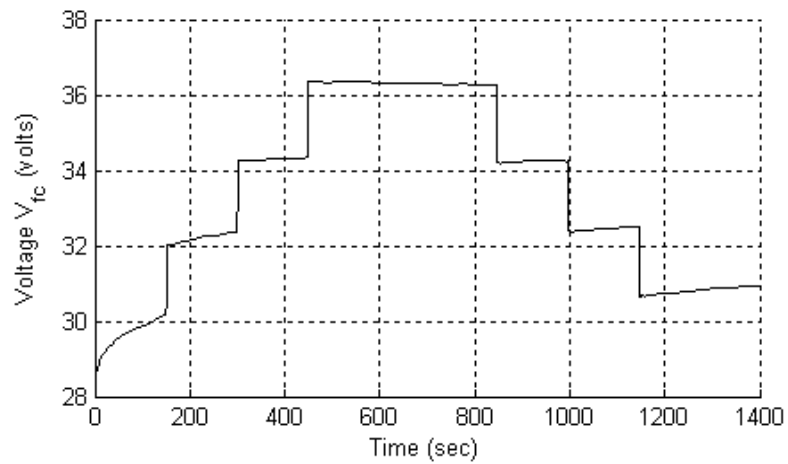


Figure 2.12 Transient Response of the PEM Fuel Cell Model over a Long-time Period

2.8.4 Behavior of the PEM Fuel Cell Model under a Resistive (R) Load

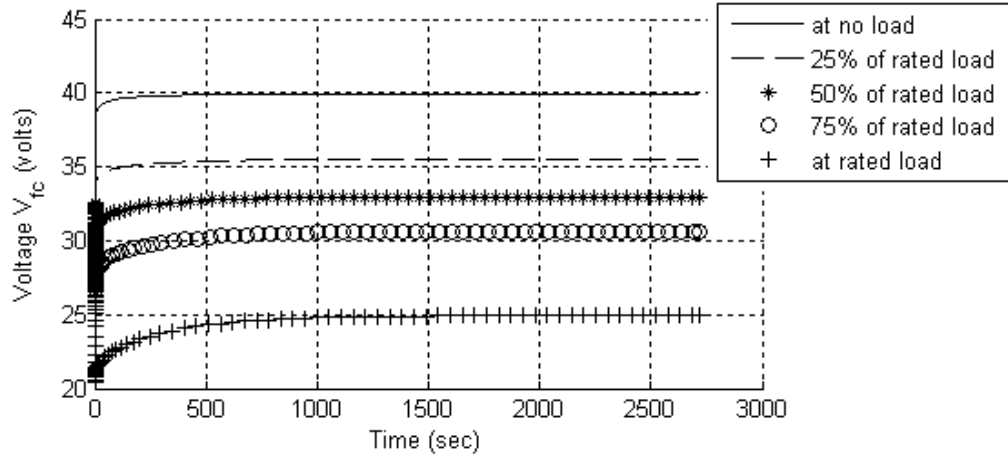


Figure 2.13 Output Voltage of the PEM Fuel Cell Model under a Resistive Load

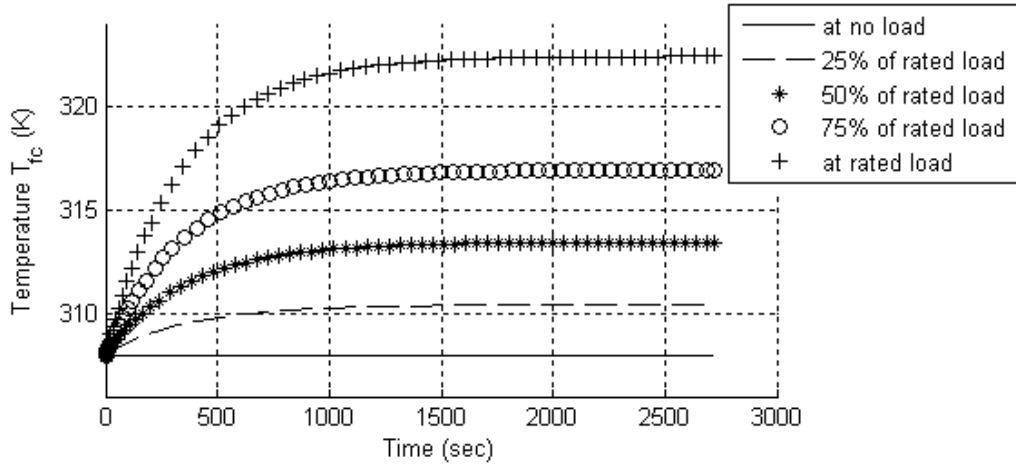


Figure 2.14 Stack Temperature of the PEM Fuel Cell Model under a Resistive Load

To study the behavior of the PEM fuel cell model under a resistive load, the model is simulated for the following values of input variables: $u_{P_A} = 5$ atm, $u_{P_C} = 5$ atm, $u_{T_R} = 308$ K. The simulation is performed under different load conditions: at no load, at 1/4th rated load current, at 1/2 rated load, at 3/4th rated load, and at rated load (25A). Figures 2.13 and 2.14 show the output voltage and stack temperature response of the model, respectively. It is observed that, as the load is increased from the no-load to the full-load condition, the output voltage is reduced. At no load, the output voltage of the PEM fuel cell model is 40 volts, while, at the full load condition (at rated load current = 25 A), the output voltage drops to about 25 volts. Also, an increase in stack temperature with the corresponding increase in the load is depicted Figure 2.14 The maximum stack temperature observed at the full-load is about 322 K.

2.9 Formulation of the PEM Fuel Cell Array

The 5-kW PEM fuel cell array is formulated by combining 2 (series) x 4 (parallel) 500-W fuel cells [35]. Figure 2.15 shows the formulation of the PEM fuel cell array in MATLAB/Simulink.

Each 500-W fuel cell used in the PEM fuel cell array has the rated current of 25 A, while, the PEM fuel cell array has the rated current of 100 A. Variation in the output voltage of the PEM fuel cell array is shown in Figure 2.16, by plotting the $V-I$ characteristics of the array.

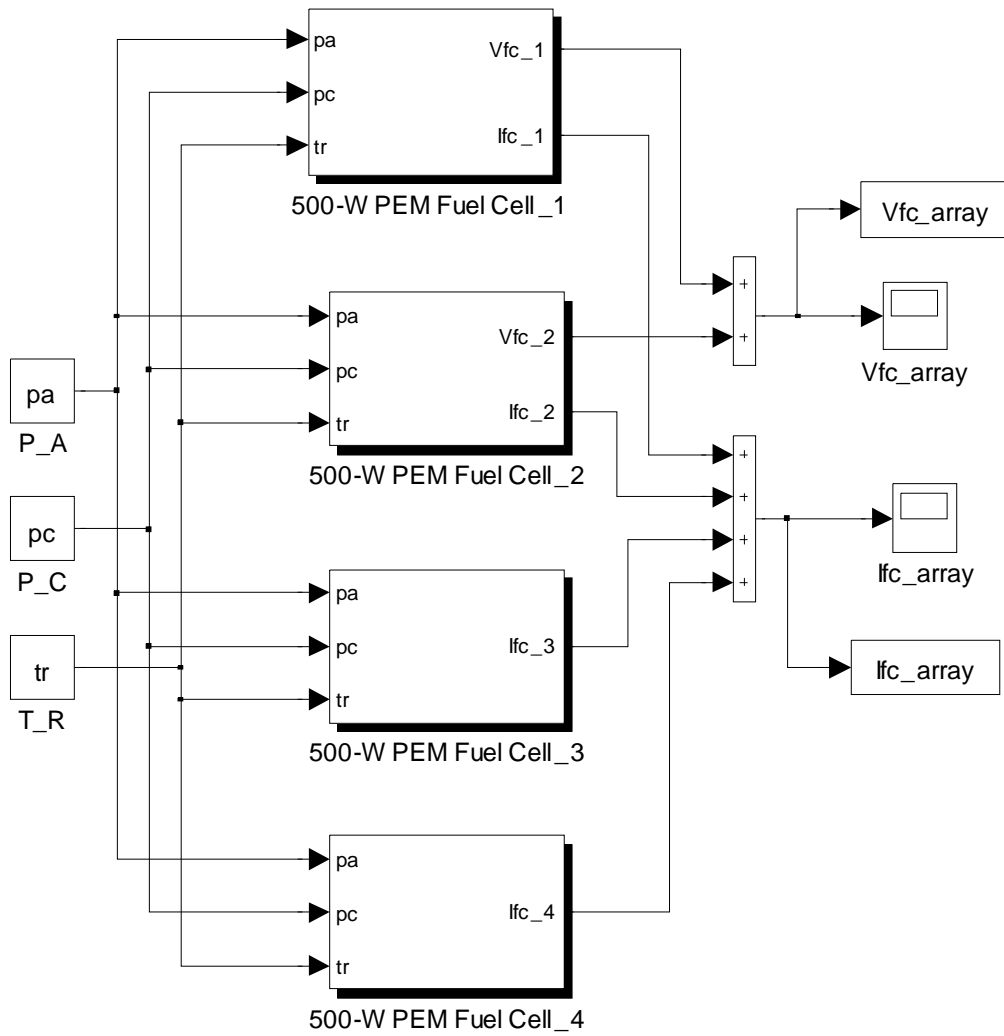


Figure 2.15 Formulation of the PEM Fuel Cell array in MATLAB/Simulink

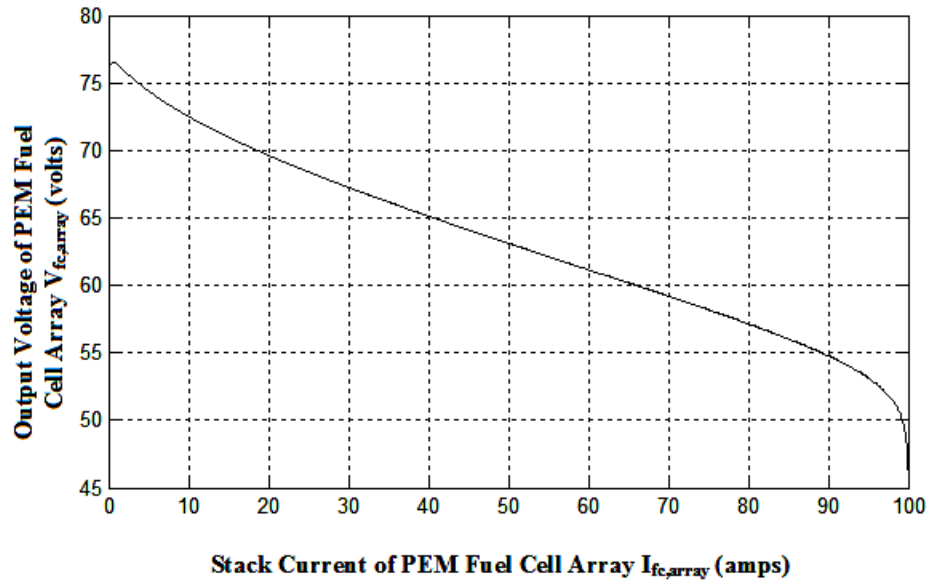


Figure 2.16 V - I Characteristics of the PEM Fuel Cell Array

2.10 Chapter Summary

In this chapter, a nonlinear state space model of a 500-W PEM fuel cell is proposed, which models an open-circuit output voltage of the PEM fuel cell, voltage losses in the PEM fuel cell, formation of a charge double-layer on the surface of the cathode in the PEM fuel cell, along with a mass balance and thermodynamic energy balance inside the PEM fuel cell system. After validating the model, it is used to study the dynamic behavior of the PEM fuel cell. The results and discussions of this study are presented in this chapter.

First, polarization curves (V - I characteristics of the PEM fuel cell) are obtained by simulating the model for different values of input variables, and it is found that by

operating the PEM fuel cell at the higher values of input variables, voltage losses in the PEM fuel cell can be reduced. Further, a transient response of the model over short and long-time periods is analyzed. It is found that the transient response of the PEM fuel cell over a short-time period mainly depends on the capacitance of a charge double-layer formed on the surface of the cathode of the PEM fuel cell, while, the transient response of the PEM fuel cell over a long-time period, depends on the thermodynamic processes and flow delays inside the PEM fuel cell system. Finally, the behavior of the model under a resistive load is studied and variation in the output voltage and stack temperature of the PEM fuel cell model, under resistive load is analyzed.

CHAPTER 3

NEURAL NETWORK MODELING OF PROTON EXCHANGE MEMBRANE FUEL CELL

3.1 Introduction

In this chapter, a neural network model of a 500-W proton exchange membrane (PEM) fuel cell is proposed. The nonlinear autoregressive moving average model of the 500-W PEM fuel cell with external inputs (NARMAX) is developed using recurrent neural network. It is shown that the two-layer neural network with a hyperbolic tangent sigmoid function, as an activation function, in the first layer and a pure linear function, as an activation function, in the second layer can effectively model the nonlinear dynamics of the PEM fuel cell. After the model is trained and validated, it is used to analyze the dynamic behavior of PEM fuel cell. Finally, the effect of measurement noise on the performance of the neural network model is investigated and the results are shown.

3.2 The Neural Network Modeling Approach

A state space model of the PEM fuel cell based on physical processes inside the PEM fuel system is developed in Chapter 2 of this dissertation. From this model development, it is learned that the relationship between the PEM fuel cell's output voltage, stack temperature, and input variables is highly nonlinear. As a result, the state space model of PEM fuel cell, developed in Chapter 2 is considerably complex,

and mathematically quite involved. Also, the development of the model required proper knowledge of various process parameters.

The neural network modeling approach provides certain unique modeling advantages. It does not require knowledge of the process parameters. Instead, the neural network possesses the ability to learn from a set of input-output data. Therefore, a neural network model proposed for the PEM fuel cell system can be trained from a set of input-output data without the need of full specifications of the PEM fuel cell system. Once correctly trained, a neural network model can provide very good mapping between the output voltage, stack temperature, and input variables of the PEM fuel cell. Also, unlike conventional modeling techniques, neural network models do not need any linearization or assumptions in model development. In the conventional modeling approach, sometimes such assumptions and/or linearization may be necessary to reduce the overall complexity of the model. Also, since neural networks are able to map highly nonlinear relationships, without the necessity of knowing the process parameters, the model development process is relatively less tedious, which helps in reducing the time required for developing the model.

3.3 Neural Network Model Development

A neural network is composed of simple elements (artificial neurons) operating in parallel. The network function is determined by the connections (weights) between the elements [59] - [60]. Also, by adjusting the values of the connections between elements, the neural network can be trained to approximate a given function. Generally, in a system

identification problem, neural networks are trained, such that that the specific set of inputs lead to the desired target output [59].

The simplest type of neural network is the feedforward network, shown in Figure 3.1, which has no feedback in its structure [61]. Hence, it can only perform memoryless mapping. I.e. at any time, the output of the neural network is determined by the current inputs to the network.

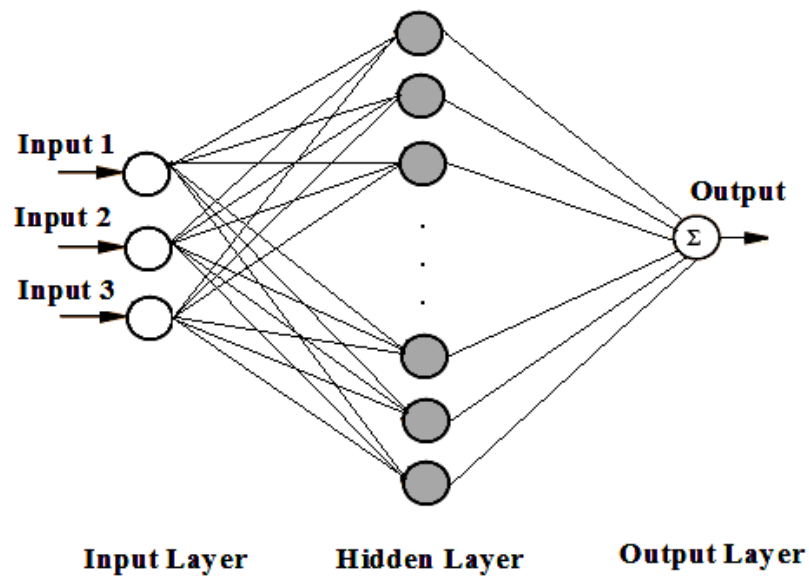


Figure 3.1 Structure of A Multilayer Feedforward Neural Network

Another type of a neural network is the recurrent neural network, shown in Figure 3.2, which has feedback from the output of the later layers to the input of the previous layers in its structure with appropriate time delays. The time delays in the recurrent

network store the values from previous time steps, which can be used in the current time step. These recurrent connections allow the neural network to both detect and generate time-varying patterns [62].

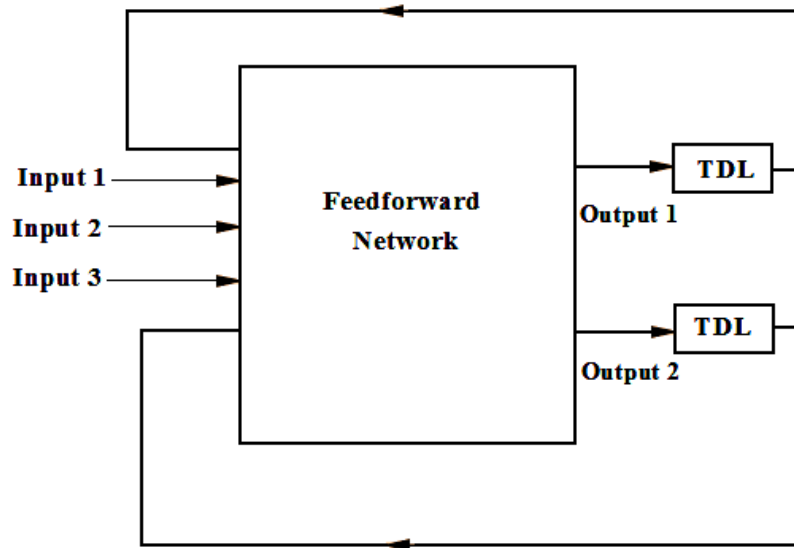


Figure 3.2 Structure of A Recurrent Neural Network

To develop the model of the PEM fuel cell system, recurrent neural network model is used. The number of time-delays to be used in the proposed network is determined by performing a cross-correlation analysis [63]-[64].

3.3.1 Cross-Correlation Analysis

The cross-correlation analysis can be used to detect the interaction strength between two signals. The analysis can also be used to detect whether a time lag exists between the

signals [63]. It has been proved in the literature that time-delay estimation between two continuous signals can be done by detecting peaks in the cross-correlation function [64].

In this work, a cross-correlation analysis is performed to determine the interaction strength between the inputs variables and output voltage of the PEM fuel cell. Equation (3.1) shows the computation of the cross-correlation function [65].

$$\varphi_{uy} = \lim_{T \rightarrow \infty} \frac{1}{2T} \int_{-T}^T u(t)y(t+\tau)dt \quad (3.1)$$

Figure 3.3, Figure 3.4, and Figure 3.5 show the results of cross-correlation between the output voltage V_{fc} of the PEM fuel cell and input vectors u_{P_A} , u_{P_C} and u_{T_R} , respectively. The presence of peaks in these figures indicates a high degree of correlation between the data separated by the corresponding discrete time instant. The contributions of the output voltage V_{fc} on input variables u_{P_A} , u_{P_C} and u_{T_R} decrease gradually with an increase in the value of lag.

Thus, based on this study, it can be seen that the input vectors u_{P_A} , u_{P_C} and u_{T_R} of the neural network model can be made sufficiently large to incorporate a large window of delayed measurements. However, very large number of lags will increase the size of the neural network's input layer and the network will require more time to converge. Therefore, the sizing of the input vectors of the network is done based on the concept of parsimony [62]. I.e. if the performance of the neural network model does not show any significant improvement with increase in the size of the input vector, then a fewer number of delays is used in the input vector [62].

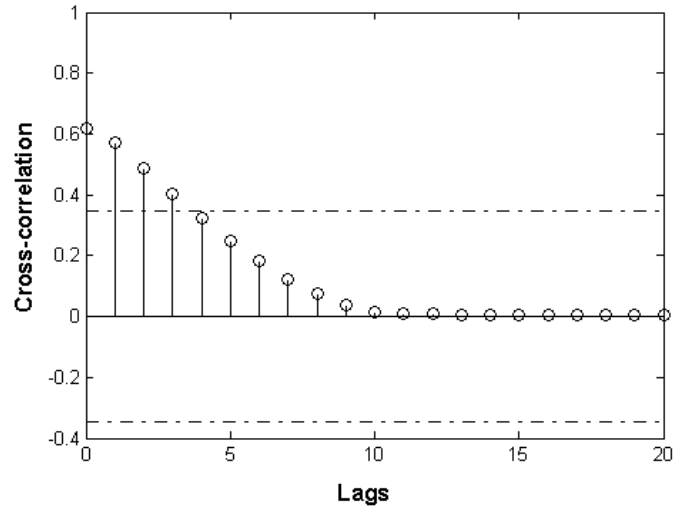


Figure 3.3 Cross-correlation between V_{fc} and u_{P_A}

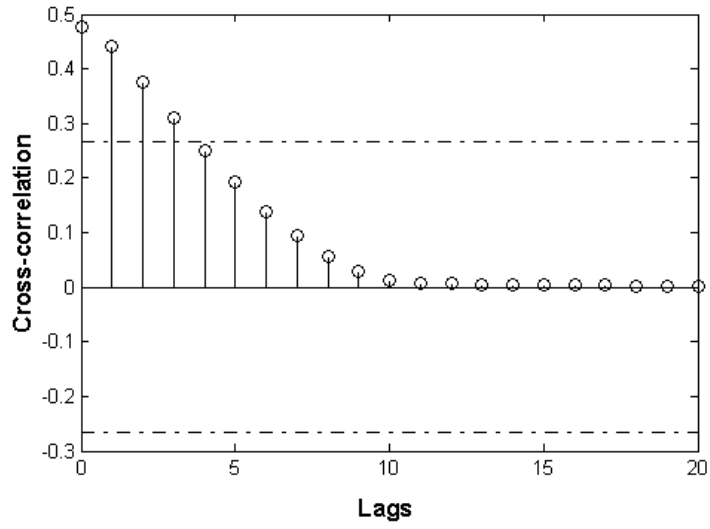


Figure 3.4 Cross-correlation between V_{fc} and u_{P_C}

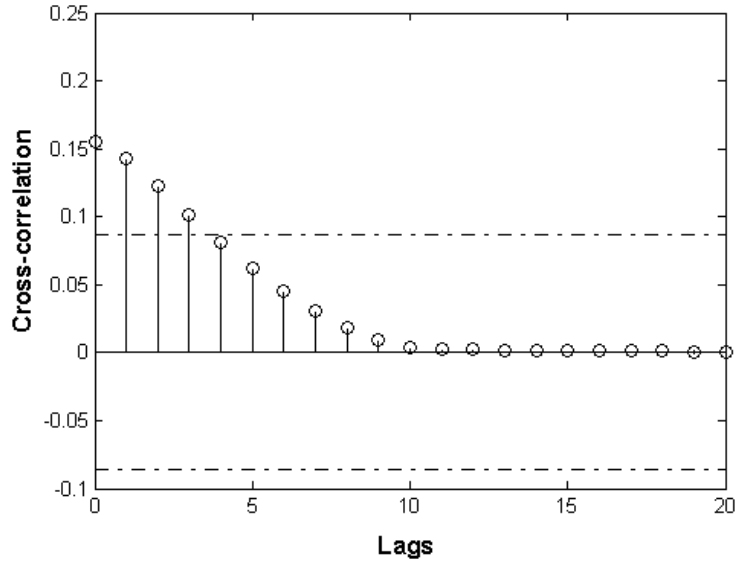


Figure 3.5 Cross-correlation between V_{fc} and u_{Tr}

Therefore, a different number of delays for input vectors u_{P_A} , u_{P_C} and u_{T_R} are tried in neural network model and finally, input vectors u_{P_A} , u_{P_C} and u_{T_R} are sized to incorporate 6 delays. It is observed that with the number of lags in the input vectors to be 6, the neural network model can be trained satisfactorily. The lags are represented by the ‘TDL’ block in neural network model in Figure 3.6.

3.3.2 The Proposed Neural Network Model for the PEM Fuel Cell

The structure of the proposed neural network to model the dynamic behavior of the PEM fuel cell is shown in Figure 3.6 [60]. The dynamic behavior of the PEM fuel cell depends on change in the output current of the the fuel cell. Hence, the output current is fed back to the model. The first layer is the input layer and the second layer is the output layer.

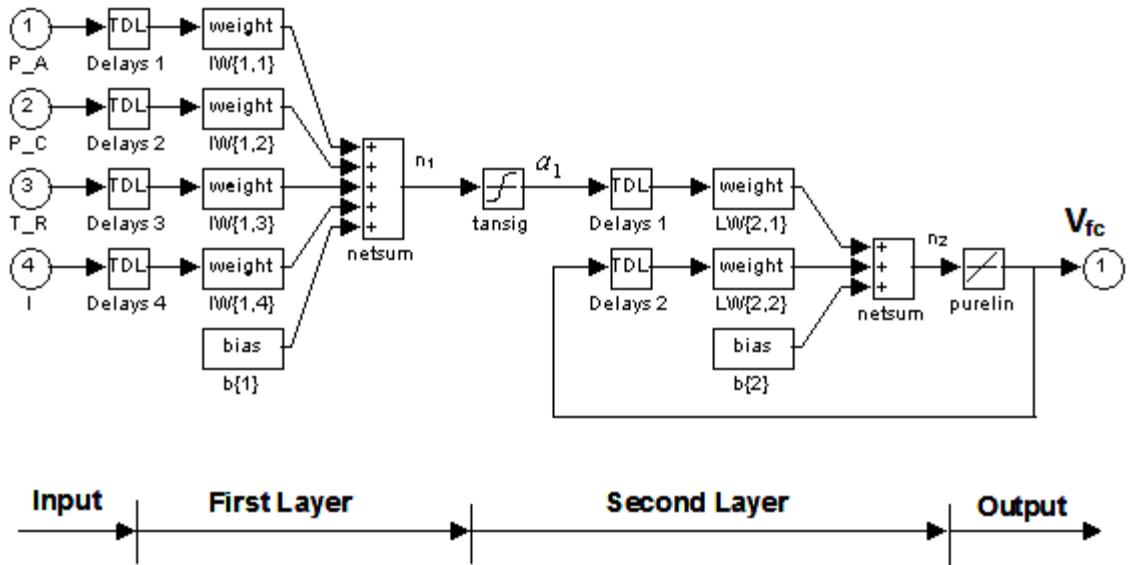


Figure 3.6 Structure of the Proposed Neural Network Model of the PEM Fuel Cell

A network with a different number of hidden neurons in the input layer is tried, and finally, the number of hidden neurons selected in the first layer are 35. A two-layer network with a hyperbolic tangent sigmoid function, as an activation function in the first

layer. and a pure linear function, as an activation function in the second layer, can be used to model most nonlinearities [59], [60]. Hence, the hyperbolic tangent sigmoid function – “tansig (..)” is chosen to be the activation function of the input layer. The relationship between a_1 , the output of the first layer, and the input variables $u_{p_A}, u_{p_C}, u_{T_R}, I$ is given by equation (3.2) [60].

$$n_1 = IW\{1,1\} u_{p_A} + IW\{1,2\} u_{p_C} + IW\{1,3\} u_{T_R} + IW\{1,4\} I + b\{1\} \quad (3.2)$$

n_1 is the weighted sum of the input variables which is fed to the hyperbolic tangent sigmoid transfer function.

$$a_1 = \text{tansig}(n_1) = \left[\frac{2}{1 + e^{-2n_1}} - 1 \right] \quad (3.3)$$

The output of the first layer, a_1 , is then fed to the second layer. A pure linear function is chosen to be the activation function of the second layer, which yields [60],

$$n_2 = LW\{2,1\} a_1 + LW\{2,2\} V_{fc} + b\{2\} \quad (3.4)$$

$$V_{fc} = \text{purelin}(n_2) \quad (3.5)$$

n_2 is the weighted sum fed to the linear function in the second layer of the network, and V_{fc} is the output of the network (output voltage of the PEM fuel cell). The output V_{fc} is fed back at the input of the second layer to create the recurrent network that helps in quicker convergence. The linear activation function is chosen in the output layer, as it can distribute the target values and can handle potential deficiencies associated with the requirements to extrapolate beyond the range of the training dataset. It also restricts

potential impact and distortions associated with upper limit and lower limit saturation effects [66].

3.3.3 Training of the Neural Network Model

The training of the proposed neural network model, shown in Figure 3.6, is performed for the PEM fuel cell's output voltage, and the stack temperature values. The data required to train the neural network model is generated by simulating the nonlinear state space model of a 500-W PEM fuel cell developed in Chapter 2. Five input-output data sets with different values of $u_{P_A}, u_{P_C}, u_{T_R}, I$ are used as the training data set. Each data set consists of 120 data samples of each input variable. The values utilized for the input variables are: u_{P_A} is varied from 5 atm to 30 atm, u_{P_C} is varied from 5 atm to 40 atm, u_{T_R} is varied from 298 K to 318 K and I is varied from 1A to 25A. Overall, 4,800 data points are used to train the model for the PEM fuel cell's output voltage, and stack temperature values. The Levenberg-Marquardt back propagation algorithm is used for training, which is performed in the neural network toolbox of MATLAB/Simulink [60].

The performance of the trained network for the output voltage values is shown in Figure 3.7. The convergence criterion for training the model is set to 10^{-5} V. After training the model for 400 epochs, the mean squared voltage error observed is $1.866 \cdot 10^{-3}$ V.

The performance of the trained network for the stack temperature values is shown in Figure 3.8. The convergence criterion for training is set to 10^{-5} K. After training the model for 200 epochs, the mean squared temperature error observed is $2.779 \cdot 10^{-5}$ K.

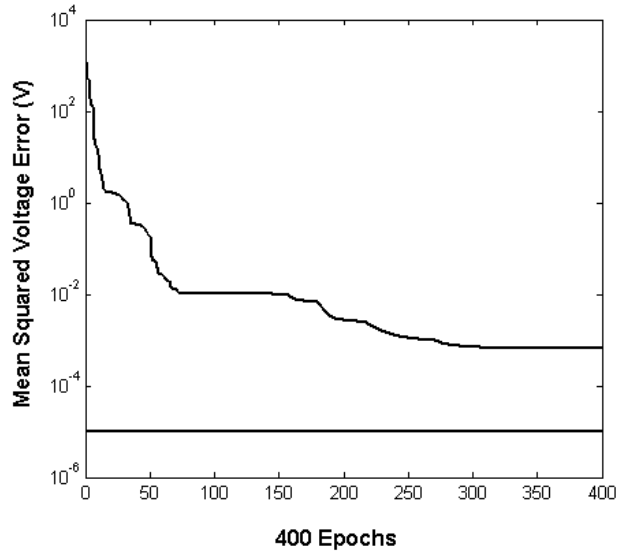


Figure 3.7 Training of the Neural Network Model for the Output Voltage Values

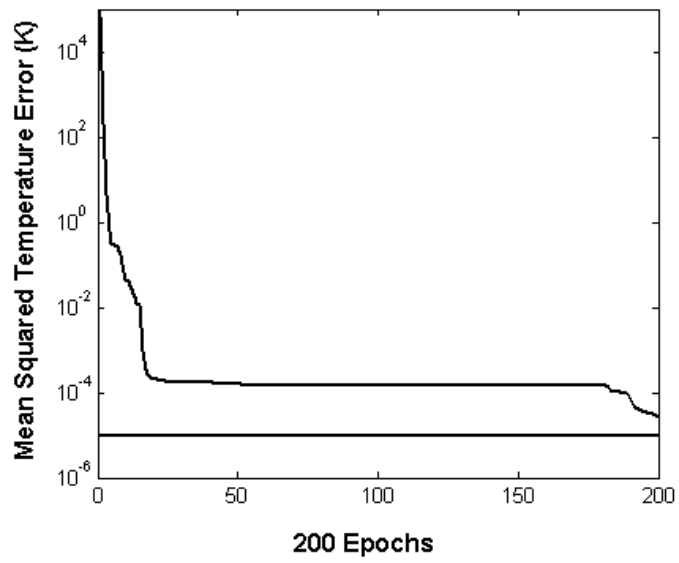


Figure 3.8 Training of the Neural Network Model for the Stack Temperature Values

3.4 Simulation Results

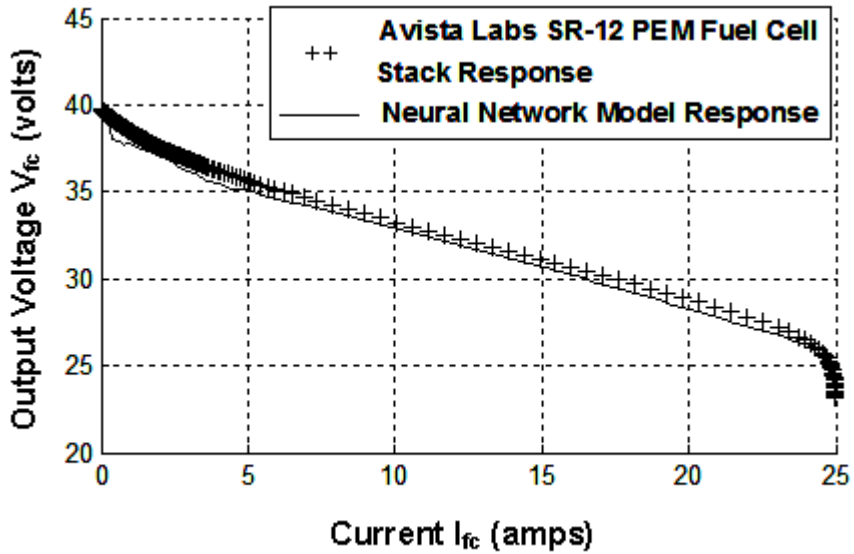


Figure 3.9 Validation of the Neural Network Model of the PEM Fuel Cell

A trained neural network model is simulated for the following values of input variables: $u_{p_A} = 1.8 \text{ atm}$, $u_{p_C} = 1 \text{ atm}$, $u_{T_R} = 308 \text{ K}$. The simulation results are validated with the experimental results of the *Avista Labs SR-12* PEM fuel cell stack presented in [20]. Figure 3.9 shows the comparison of the $V-I$ characteristics of the neural network model with the $V-I$ characteristics of the *Avista Labs SR-12* PEM fuel cell stack obtained experimentally. The validation results show a close match. Please note that, in [20], the experimental results of the *Avista Labs SR-12* (500-W) PEM fuel cell stack are given and the $V-I$ characteristics obtained by simulating the neural network model

developed in this paper are compared with the experimental $V-I$ characteristics presented in [20].

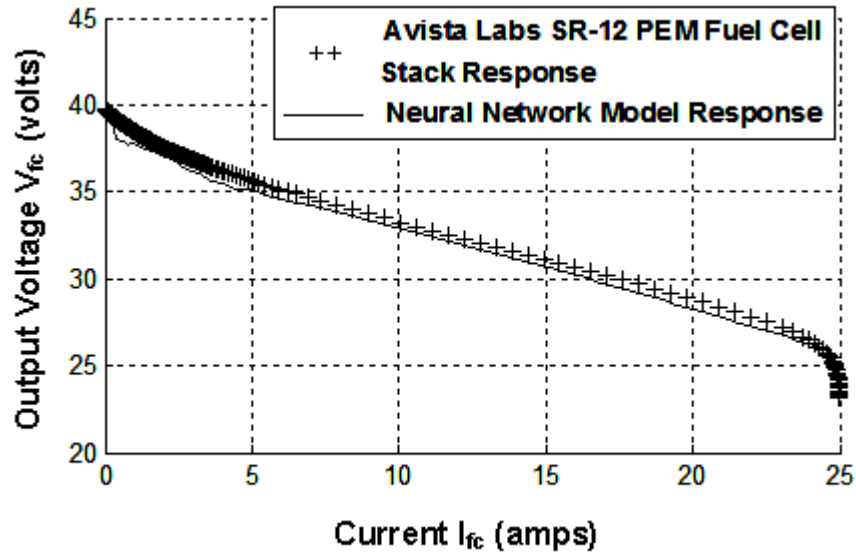


Figure 3.10 Validation of the State Space Model of the PEM Fuel Cell

As training of a neural network model is performed with the data generated by the state space model and not directly with the experimental PEM fuel cell data, it is important to check the degree of compliance of the state space model with the actual experimental results. Hence, the simulation results of the state space model are also validated with the experimental data of the *Avista Labs SR-12* PEM fuel cell stack given in [20]. The comparison is shown in Figure 3.10.

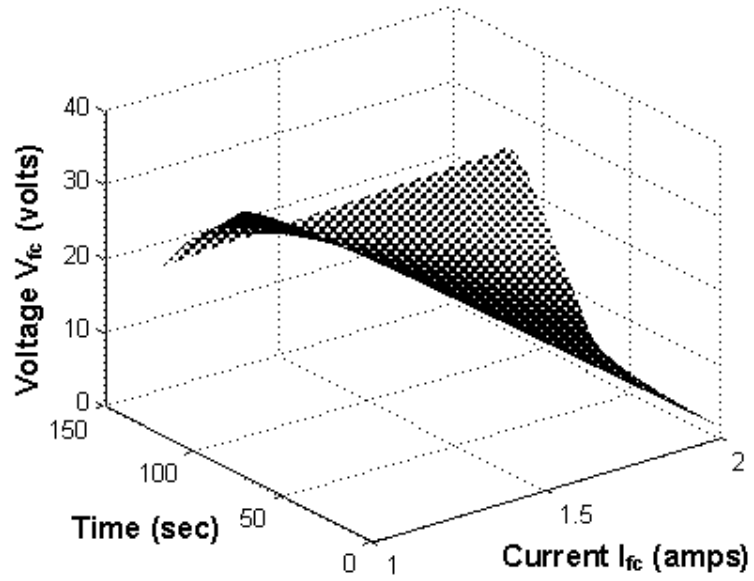


Figure 3.11 Polarization Characteristics of the Neural Network Model

Figure 3.11 shows polarization characteristics or $V-I$ characteristics of the PEM fuel cell model with respect to time, in three-dimensional plane obtained by simulating the model at $u_{p_A} = 1.5 \text{ atm}$, $u_{p_C} = 1 \text{ atm}$, $u_{T_R} = 303 \text{ K}$

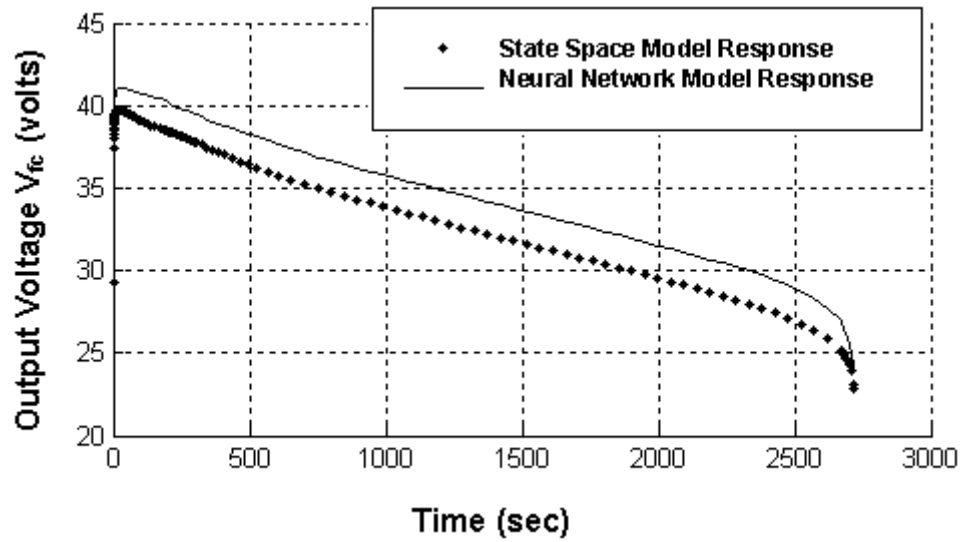


Figure 3.12 Output Voltage Response of the Neural Network Model

The output voltage response of the neural network model is shown in Figure 3.12. To obtain this output voltage response, the current is varied from 1A to 25 A in steps of 0.4 A every 40 seconds over a total simulation period of 2720 seconds. It is seen that the output voltage decreases from about 41 volts to 24 volts as the current is increased. The response is compared with the output voltage response of the state space model.

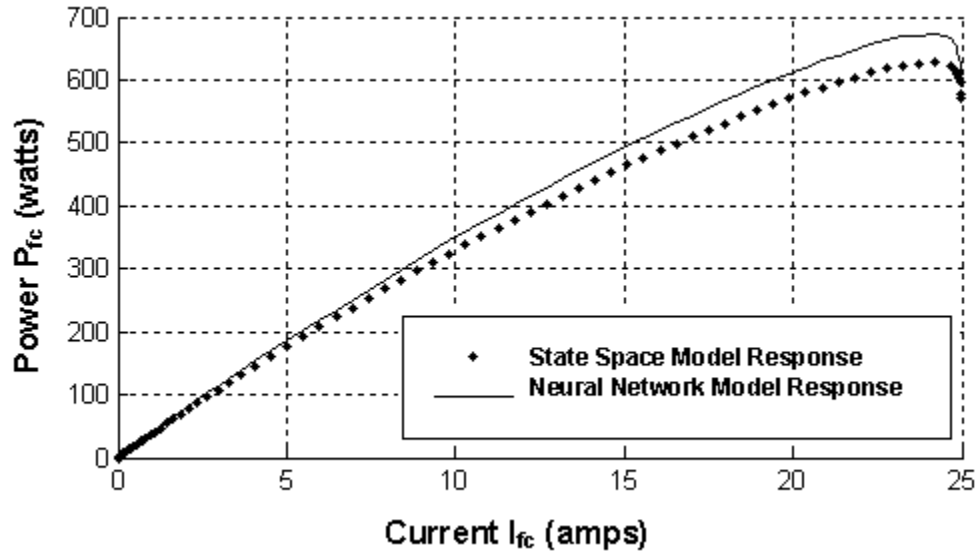


Figure 3.13 P - I Characteristics of the Neural Network Model

Figure 3.13. shows the P - I characteristics obtained by simulating the neural network model. It can be seen that the maximum output power is obtained close to the rated current of the fuel cell (25A) but not exactly at the rated current. A PEM fuel cell goes in the concentration region near the rated current value. In this region, the output voltage of the PEM fuel cell drops sharply due to an increase in the current. This leads to the decrease in the output power of the PEM fuel cell [20], [54].

To obtain the temperature response, a neural network model is simulated for the following values of input variables: $u_{P_A} = 2.5 \text{ atm}$, $u_{P_C} = 1 \text{ atm}$, $u_{T_R} = 308 \text{ K}$. Figure 3.14 shows the temperature response of the model. The response is compared with the temperature response of the state space model developed in Chapter 2, and comparison

shows a close match. It can be seen that, as electrochemical reaction proceeds within the PEM fuel cell, the stack temperature rises from 308 K to 316 K.

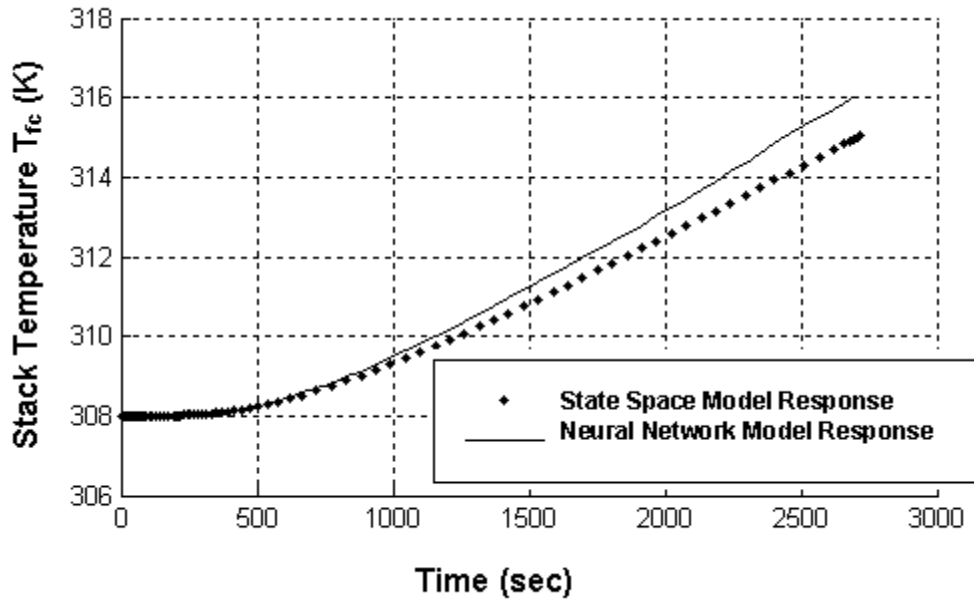


Figure 3.14 Temperature Response of the Neural Network Model

3.4.1 Polarization Curves of the PEM Fuel Cell Model for Different Values of Input Variables

A neural network model is subjected to different values of input variables in order to study their effect on the $V-I$ characteristics, output voltage of the PEM fuel cell, and, voltage losses.

Figure 3.15 shows the $V-I$ characteristics obtained by simulating a neural network model for different values of u_{P_A} . The model is simulated for:

$u_{P_A} = 2 \text{ atm}, 5 \text{ atm}, 8 \text{ atm}, 15 \text{ atm}$. The other two input variables u_{P_C} and u_{T_R} are kept constant at 1 atm and 308 K , respectively. It is seen that, as u_{P_A} is increased, the output voltage of the PEM fuel cell increases and it reduces voltage losses in the PEM fuel cell. From Figure 3.15, it can be seen that voltage losses are smaller for the higher values of u_{P_A} . Hence, it is possible to reduce voltage losses in the PEM fuel cell by operating the fuel cell at higher values of u_{P_A} .

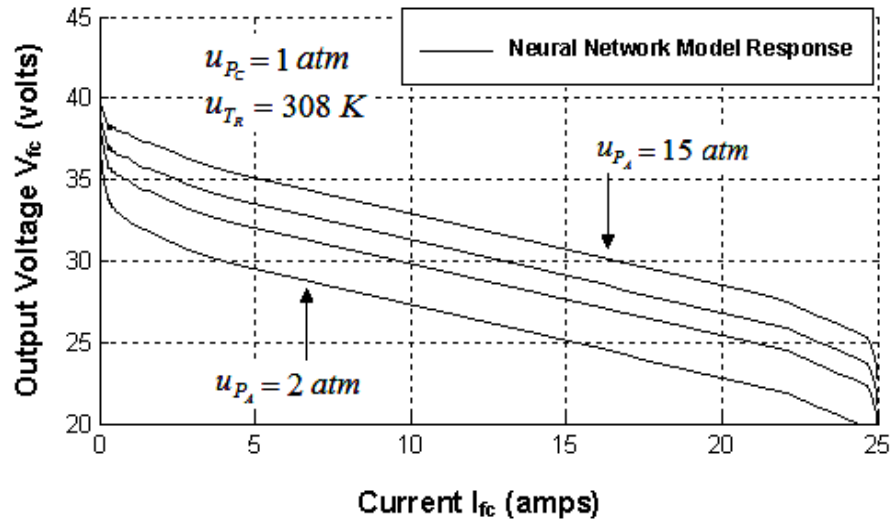


Figure 3.15 V-I Characteristics of the PEM Fuel Cell Model for Increasing u_{P_A}

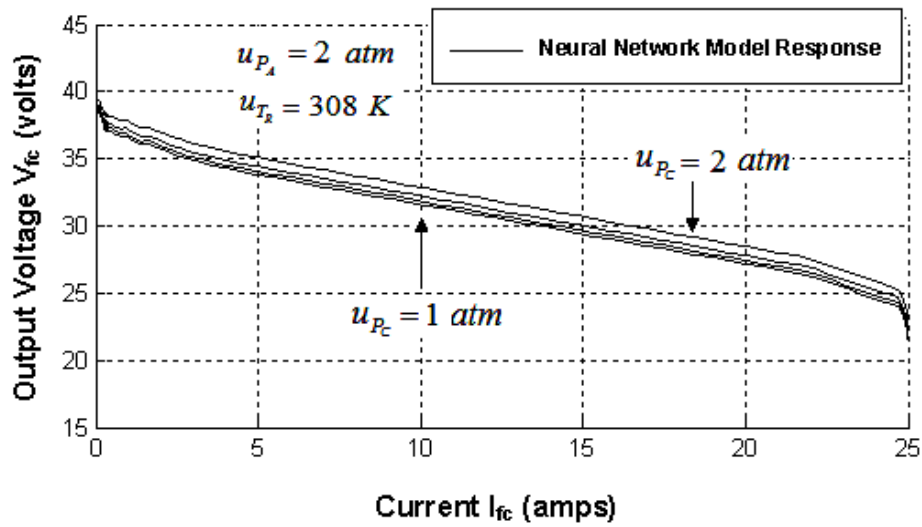


Figure 3.16 V - I Characteristics of the PEM Fuel Cell Model for Increasing u_{P_C}

Figure 3.16 shows the V - I characteristics obtained by simulating a neural network model for the increasing values of u_{P_C} . The model is simulated for: $u_{P_C} = 1 \text{ atm}$, 1.5 atm , 1.8 atm , 2 atm . The other two input variables u_{P_A} and u_{T_R} are kept constant at 2 atm and 308 K , respectively. Again, it can be seen that, as u_{P_C} is increased, the output voltage of the PEM fuel cell increases which reduces voltage losses in the PEM fuel cell. For the higher values of u_{P_C} , voltage losses are smaller. It must be noted that a neural network model of the PEM fuel cell cannot be used to compute the value of any individual voltage losses within the PEM fuel cell. The model can only determine overall change in the value of voltage losses as a function of input variables.

3.4.2 Transient Response of the PEM Fuel Cell Model

A trained neural network model of the PEM fuel cell can be used to study the transient response of the PEM fuel cell over short and long-time periods. Figure 3.17 shows the transient response of the model over a short-time period. The model is simulated for $u_{p_A} = 2.5 \text{ atm}$, $u_{p_C} = 1 \text{ atm}$, $u_{T_R} = 308 \text{ K}$. The input variable I of the model is varied in steps over a small time period between 99 sec to 102 sec to observe the transient behavior. It can be seen that, as the load is increased, the output voltage drops and vice-versa. However, the output voltage does not reach the new value immediately. As load is increased, the voltage drops to a certain value immediately but from there it reaches to its new value in an exponential manner. This is due to the capacitance of charge double-layer formed on the surface of the cathode. Higher the value of the capacitance formed due to the charge double-layer, longer it takes for the voltage to reach its new value [20], [54]. Hence, the transient response of the PEM fuel cell over a short-time period is dominated by the capacitance of the charge double-layer.

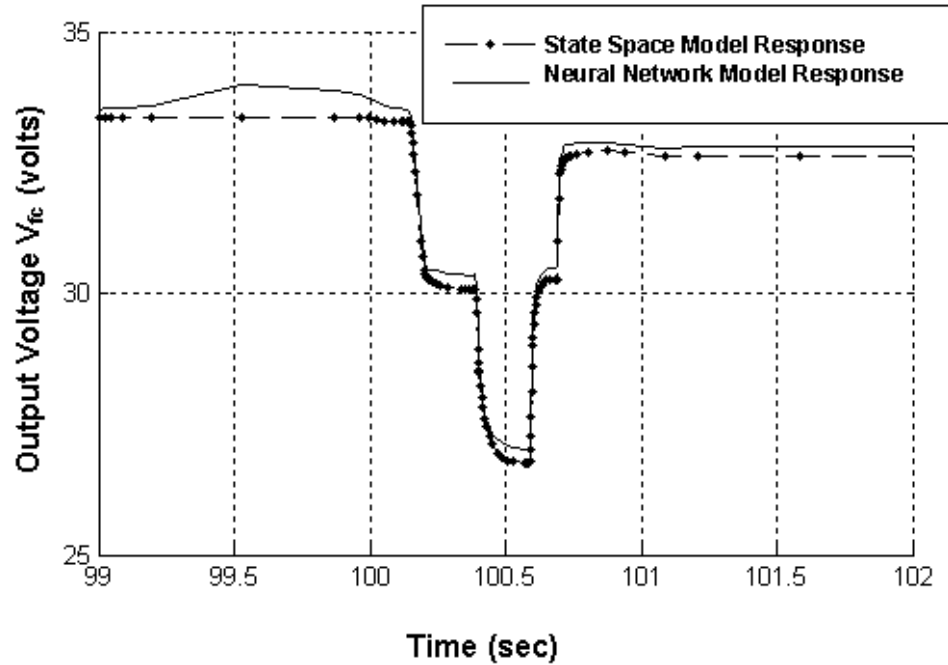


Figure 3.17 Transient Response of the Model over a Short-time Period

The transient response of the neural network model over a long-time period is shown in Figure 3.18. It is observed that, as the load current is changed, the output voltage changes to a certain value and from there it reaches to its final value in few hundred seconds. This type of a response is observed due to the higher thermodynamic time constant, as well as due to air and hydrogen flow delays inside the PEM fuel cell. These delays can vary from few seconds to few minutes in the PEM fuel cell [11], [20].

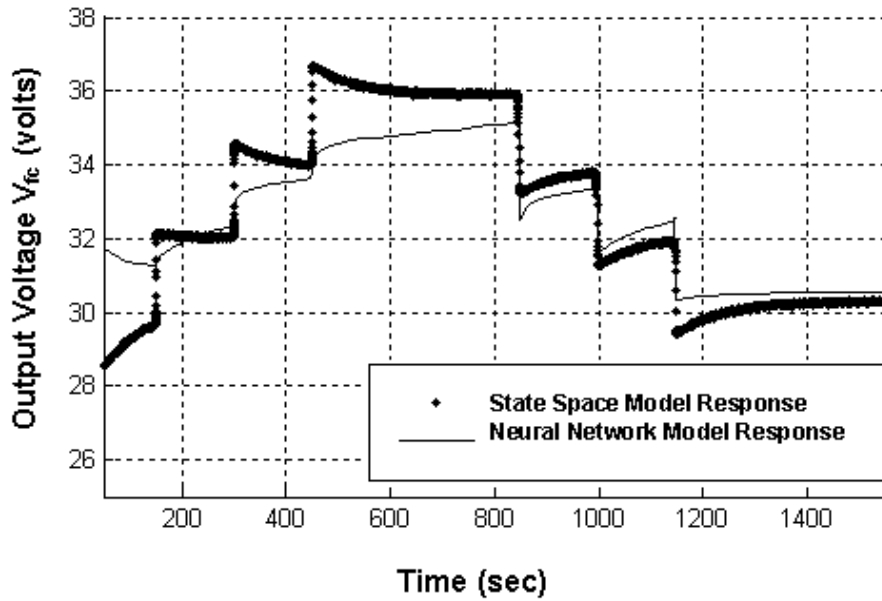


Figure 3.18 Transient Response of the Model over a Long-time Period

It can be seen from Figure 3.14 that change in the temperature of the PEM fuel cell stack takes certain time, as electrochemical reaction proceeds in the PEM fuel cell. I.e. the stack temperature cannot change immediately. This makes thermodynamic time constant of the PEM fuel cell higher. Similarly, the hydrogen and air flow to the anode and cathode cannot immediately follow changes in the load [20]. Hence, it can be concluded that the transient response of the PEM fuel cell over a long-time period depends on the thermodynamic time constant of the PEM fuel cell and flow delays within the PEM fuel cell [11], [20].

3.5 Robustness toward Noise

To investigate the effect of measurement noise on the performance of a neural network model, noise-corrupted measurements are generated by adding zero mean independent white Gaussian noise to noise free signals. These noise-corrupted signals are then applied to the neural network model of the PEM fuel cell. The equations used to generate the noise corrupted signals are given in [67].

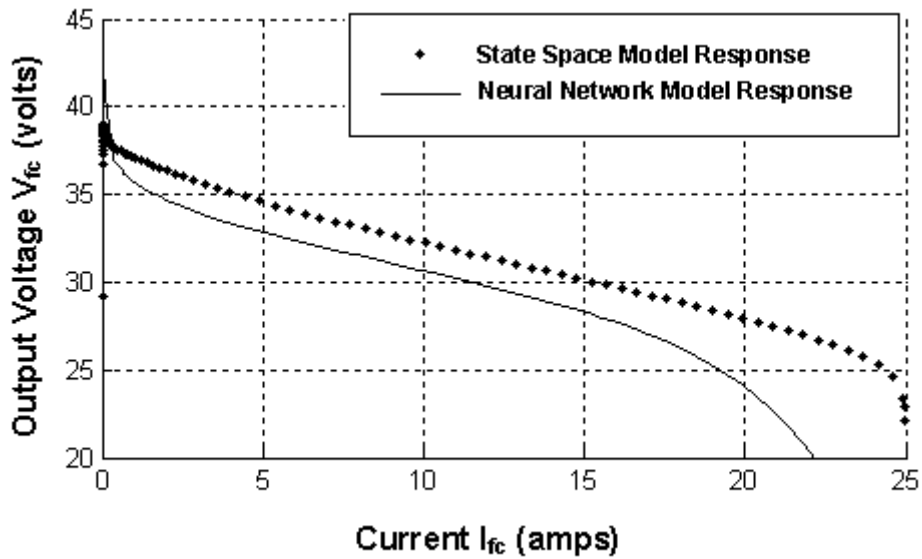


Figure 3.19 Performance of the Neural Network Model for SNR = 200:1

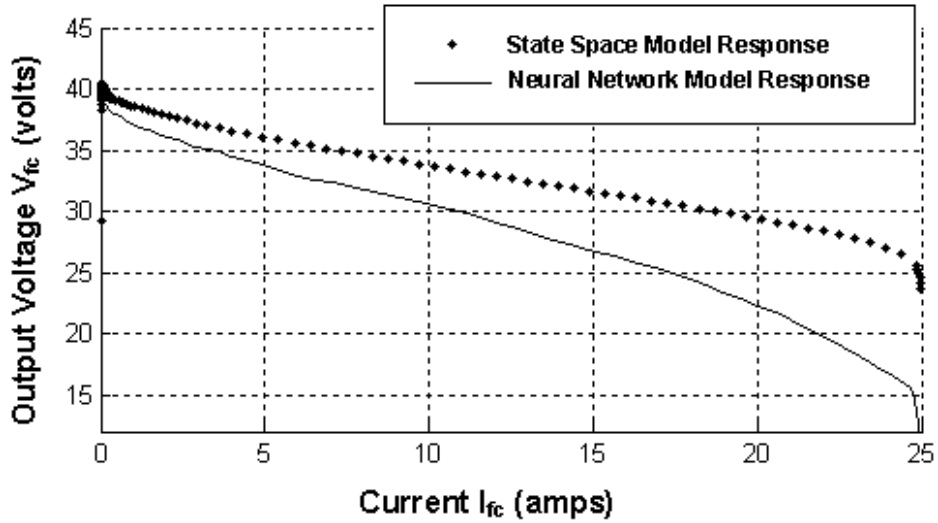


Figure 3.20 Performance of the Neural Network Model for SNR = 50:1

The results of the application of noise-corrupted data, with different SNR levels, to the neural network model are tabulated in Table 3.1. For sake of comparison, the mean squared voltage error for noise free case, is also listed. It can be seen that with low SNR levels (large amount of noise), the performance of the neural network model deteriorate significantly with a corresponding increase in the mean squared voltage error. The performance of the neural network model for SNRs 200:1 and 50:1 is shown in Figures 3.19 and 3.20, respectively.

Signal-to-Noise Ratio (SNR)	Mean Squared Voltage Error
No noise	$1.866 \cdot 10^{-3}$
1000:1	$2.779 \cdot 10^{-3}$
800:1	$8.625 \cdot 10^{-3}$
500:1	$3.39 \cdot 10^{-2}$
200:1	$7.971 \cdot 10^{-2}$
100:1	$9.142 \cdot 10^{-2}$
50:1	$9.912 \cdot 10^{-2}$
10:1	$1.032 \cdot 10^{-1}$

Table 3.1 Mean Squared Voltage Errors for Different Signal-to-Noise Ratios (SNRs)

3.6 Chapter Summary

In this chapter, the nonlinear auto regressive model of a 500-W PEM fuel cell with external inputs (NARMAX) is developed using a recurrent neural network. It is shown that the nonlinear dynamics of the PEM fuel cell can be effectively modeled using the two-layer recurrent neural network. The data required to train the neural network model is generated by simulating the nonlinear state space model of the PEM fuel cell developed in Chapter 2. The neural network model is trained for the PEM fuel cell's output voltage and stack temperature values. To prove the effectiveness of the model, it is validated with the experimental results of the *Avista Labs SR-12* (500-W) PEM fuel cell stack presented in [20]. The model is then used to analyze the dynamic behavior of the PEM fuel cell.

Polarization curves are obtained by subjecting the model to different values of input variables. It is found that voltage losses in the PEM fuel cell can be reduced by operating the PEM fuel cell at the higher values of input variables. The transient behavior of the PEM fuel cell over short and long-time periods is studied. Finally, the robustness of the trained neural network model toward noise is analyzed, and it is shown that the low SNR levels increase the mean squared voltage error, which results in deterioration of the performance of the neural network model.

CHAPTER 4

MODELING OF LEAD-ACID BATTERY AND CONTROL OF DC/DC CONVERTER

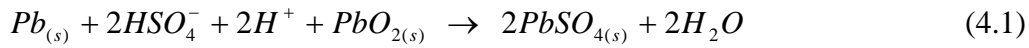
4.1 Introduction

In this chapter, sizing of the lead-acid battery bank, required for the DG system, is performed and charging of the battery bank is simulated in MATLAB/Simulink. In order to design the battery bank and simulate its charging, a model of the PEM fuel cell, the dc/dc boost converter, and the model of lead-acid battery is required. The PEM fuel cell model is already developed in Chapter 2 of this dissertation. The model of the lead-acid battery and the model of the dc/dc converter are given in this chapter. The parameters of the battery model are identified using curve fitting techniques, and the model is validated with a 12 V, 4 Ah *Yuasa (NP4-12)* battery [51]-[52]. The discharge characteristics of the battery are studied using the battery model, and the model is then appropriately scaled to design the battery bank.

The model of the dc/dc boost converter, based on the state space averaging technique is given, and the sliding mode controller is designed for the dc/dc boost converter to control its output voltage.

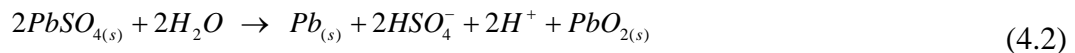
4.2 Modeling of the Lead-Acid Battery

A lead-acid battery is a group of electrochemical cells which can deliver the current at nominal voltage to an electrical load [68]. The number of electrochemical cells connected in series determines the terminal voltage of a battery. An open-circuit voltage of the standard lead-acid battery at full charge is 12.6–12.8 V, while, the current capacity can differ based on a number of cells and the application [69]. In a charged state, each cell inside the battery contains electrodes of a lead (Pb) and lead oxide (PbO_2) in an electrolyte of around 33.5 % (v/v) sulphuric acid (H_2SO_4). When the battery is connected to an external electrical load, there exists a flow of electrons. The overall chemical reaction can be given by [68]:



where, $Pb_{(s)}$ is solid lead, HSO_4^- is hydrogen sulphide ion, H^+ is hydrogen ion. The subscript (s) refers to solid. During this reaction, i.e. during the battery discharging process, insoluble lead sulphate ($PbSO_4$) is formed at each electrode, and the reaction produces water (H_2O), which dilutes the electrolyte [68]-[69].

During the charging process, when the dc voltage source is connected at the battery terminals, direction of the electron flow is reversed, and the lead-sulphate is removed from the electrodes. The electrolyte becomes stronger and hydrogen ions are regenerated. The overall reaction is given by [68]:



The internal chemical processes inside the lead-acid battery can be modeled with their electrical equivalents, and the battery behavior, seen from its terminals, can be analyzed. In other words, the behavior of the lead-acid battery can be modeled in terms of the electrical networks composed of electromotive forces (emfs), resistors, capacitors, and inductors [46].

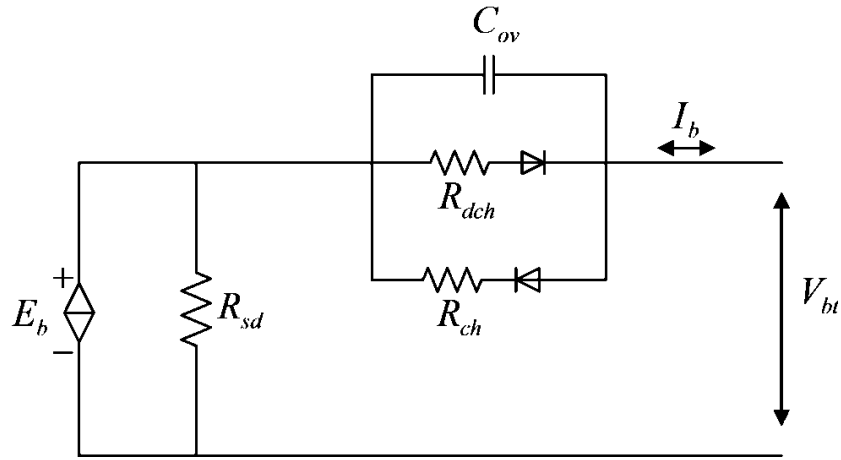


Figure 4.1 The Proposed Lead-Acid Battery Model

The dynamic model of the lead-acid battery, shown in Figure 4.1, is proposed by *Jantharamin N. and Zhang, L.* in [51]. The battery emf, (E_b) , is modeled by a dependent voltage source as shown in Figure 4.1. The battery emf (E_b) is a linear function of the SOC (state of charge) of the battery. In lead-acid batteries, there exist a difference between the battery emf (E_b) and terminal voltage (V_{bt}) of the battery, known as

polarization effect. This polarization effect, caused due to the ohmic voltage drop and overvoltage effects, in the lead-acid battery is modeled by a resistor-capacitor network, as shown in Figure 4.1. The polarization resistance is represented by a single equivalent resistor (R_{ch} or R_{dch}) for an each operating mode [51]. During the charging process, the current flows through the ohmic resistor R_{ch} , while, during discharging process, the current flows through ohmic resistor R_{dch} . Ideal diodes are connected in their respective paths to allow the current flowing through the desired resistances. The self-discharge losses in the battery are modeled by the resistor (R_{sd}). The battery current is denoted by I_b .

The charge stored in the battery can be given as [46]:

$$Q_e(t) = \int_0^t I_b \cdot d\tau \quad \text{or} \quad \frac{dQ_e}{dt} = I_b \quad (4.3)$$

Also, the terminal voltage of the battery during the charging mode and discharging mode can be given by equations (4.4) and (4.5), respectively [51]:

$$V_{bt,Charging} = E_b - I_b R_{dch} \cdot \left[1 - \exp\left(\frac{-t}{R_{dch} \cdot C_{ov}}\right) \right] \quad (4.4)$$

$$V_{bt,Discharging} = E_b + I_b R_{ch} \cdot \left[1 - \exp\left(\frac{-t}{R_{ch} \cdot C_{ov}}\right) \right] \quad (4.5)$$

During the charge and discharge cycles, the dynamic characteristics of the battery depend on the battery SOC, the charge/discharge rate, and the electrolyte temperature [51]. The battery SOC is defined (in percent) as [51]:

$$SOC = SOC_0 + \left(\frac{1}{C_n} \int_0^t I_b \cdot d\tau \right) \times 100 \quad (4.6)$$

where, SOC_0 is the initial state of charge in per cent, C_n is the nominal battery capacity in amp-hours (Ah), and I_b is the battery current in amperes (A), which is defined positive during charging, and negative during discharging.

To identify, the model parameters E_b , R_{sd} , R_{dch} , C_{ov} , R_{ch} of the proposed battery model to determine the battery terminal voltage during charging and discharging process, the parameter identification process proposed by *Jantharamin N. and Zhang, L.* in [51] is implemented in this work. The model parameters are determined using curve-fitting technique, and using the manufacturer's datasheet for the *Yuasa (NP4-12)* battery, rated 4 Ah, 12V [51]-[52].

4.3 Identification of the Battery Model Parameters

4.3.1 Battery EMF (E_b)

According to the manufacturer's datasheet for the *Yuasa (NP4-12)* battery, the relationship between the open circuit voltage of the battery and remaining battery capacity is approximately linear, as shown by dashed line boundaries in Figure 4.2 [52]. Using the linear approximation technique, a linear function between E_b and SOC can be established as [51]:

$$E_b = 0.01375 \cdot (SOC) + 11.5 \quad (4.7)$$

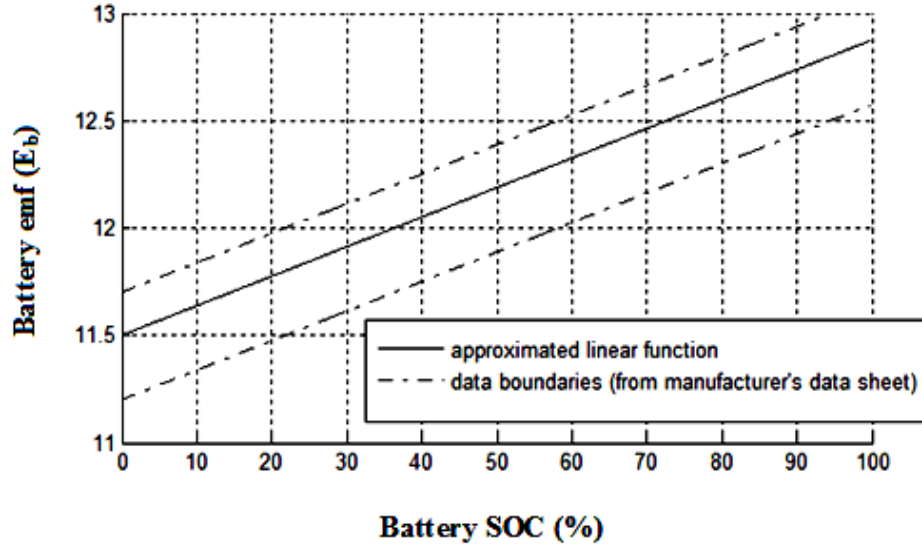


Figure 4.2 Variation in E_b as a Function of the Battery SOC

4.3.2 Self-Discharge Resistance (R_{sd})

The information on the remaining battery capacity against the storage time in the manufacturer's datasheet for the *Yuasa (NP4-12)* battery is used to model the self-discharge resistance R_{sd} [52]. Using a piecewise linear function approximation, the self-discharge current I_{sd} at $25^{\circ}C$ is assumed to be constant within each interval of the storage time [51]:

$$I_{sd} = \frac{\Delta SOC}{100} \cdot \frac{C_n}{\Delta t} \quad (4.8)$$

where, Δt is the storage time interval which is equal to one month in this estimation, and ΔSOC is a decrease in SOC in percent. Subsequently, R_{sd} can be defined as [51]:

$$R_{sd} = \frac{E_b}{I_{sd}} \quad (4.9)$$

The values of R_{sd} are plotted against the SOC as shown in Figure 4.3, and using curve-fitting method, a quadratic polynomial function is chosen to express R_{sd} in $k\Omega$ as:

$$R_{sd} = -0.039.(SOC)^2 + 4.27.(SOC) - 19.23 \quad (4.10)$$

Equation (4.10) is used to simulate the variation of self-discharge resistance R_{sd} of a battery as a function of the battery SOC.

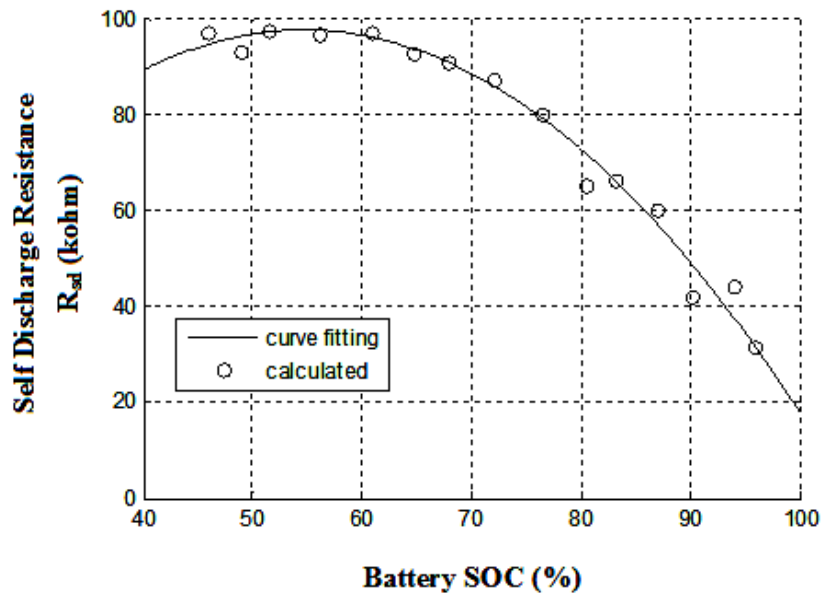


Figure 4.3 Variation in R_{sd} as a Function of the Battery SOC

4.3.3 Discharge Polarization Resistance (R_{dch})

The terminal voltage of the battery during discharge is given as [51]:

$$V_{bt, Discharging} = E_b - I_b R_{dch} \left[1 - \exp\left(\frac{-t}{R_{dch} \cdot C_{ov}}\right) \right] \quad (4.11)$$

The resistance R_{dch} can be divided into two components as [51]:

$$R_{dch} = R_{bdi} + R_{bd} \quad (4.12)$$

The resistance R_{bdi} models the change in the terminal voltage from the battery emf during transient interval, and hence, depends on the discharge current. The resistance R_{bd} models the variation of R_{dch} with the battery SOC as the discharge proceeds [51].

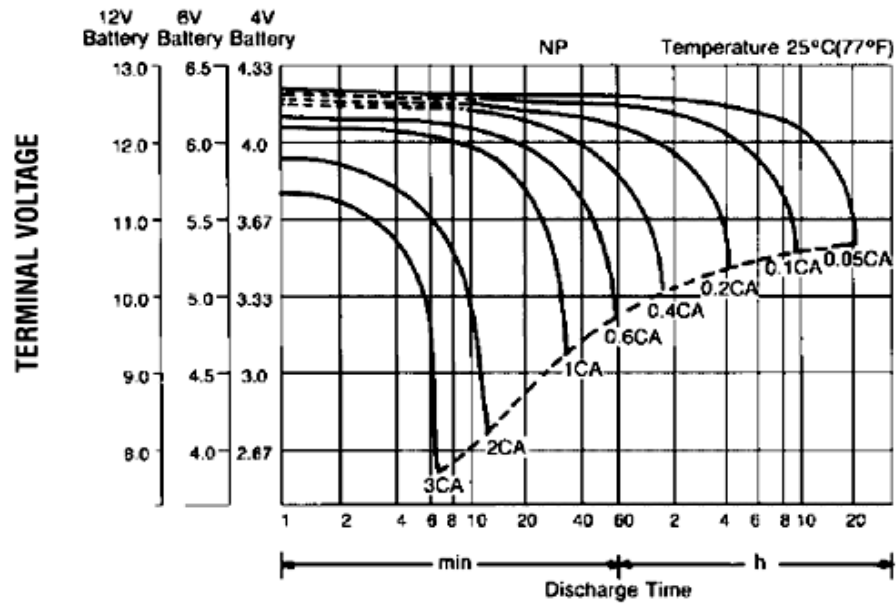


Figure 4.4 Discharge Characteristics of Yuasa NP4-12 Battery (From the manufacturer's data sheet)

The discharge characteristics of a *Yuasa NP4-12* battery from the manufacturer's data sheet are shown in Figure 4.4 [52]. 'C' denotes the given capacity as stated on an each battery in Ah. It can be observed that the first sample of the terminal voltage for each curve is taken, at one minute after the discharge has started. For each discharge rate, the resistance R_{bdi} can be estimated as:

$$R_{bdi} = \left. \frac{E_b - V_{bt}}{I_b} \right|_{t=1 \text{ min}} \quad (4.13)$$

Hence, the values of R_{bdi} are plotted in Figure 4.5. The mathematical expression in a form of two exponential functions is chosen to represent R_{bdi} and given as [51]:

$$R_{bdi} = 1.01 \cdot \exp(-2.21 \cdot I_b) + 0.24 \cdot \exp(-0.06 \cdot I_b) \quad (4.14)$$

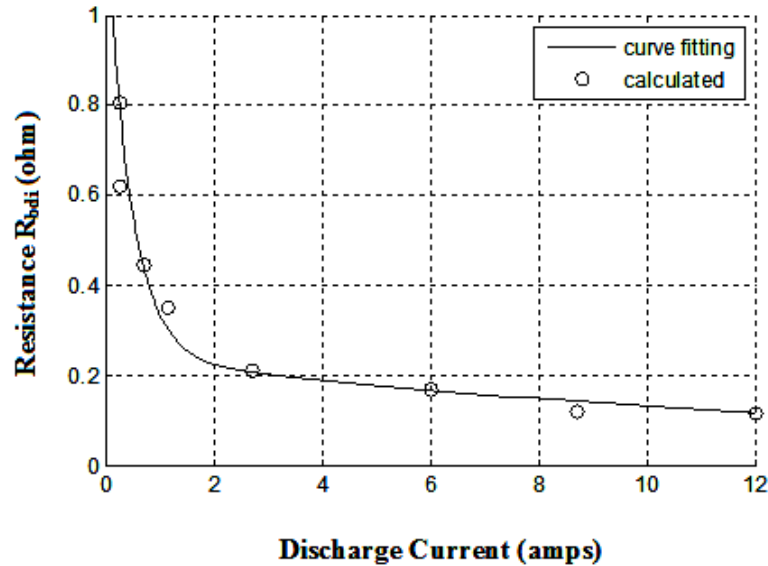


Figure 4.5 Variation in R_{bdi} with the Discharge Current

After transients die away, the resistance R_{bd} for specific discharge rate can be derived as

[51]:

$$R_{bd} = \frac{E_b - V_{bt}}{I_b} - R_{bdi} \quad (4.15)$$

The values of R_{bd} are calculated and plotted in Figure 4.6. Using the curve fitting technique, a mathematical function is established for R_{bd} as [51]:

$$R_{bd} = 2.926 \cdot \exp(-0.042 \cdot SOC) \quad (4.16)$$

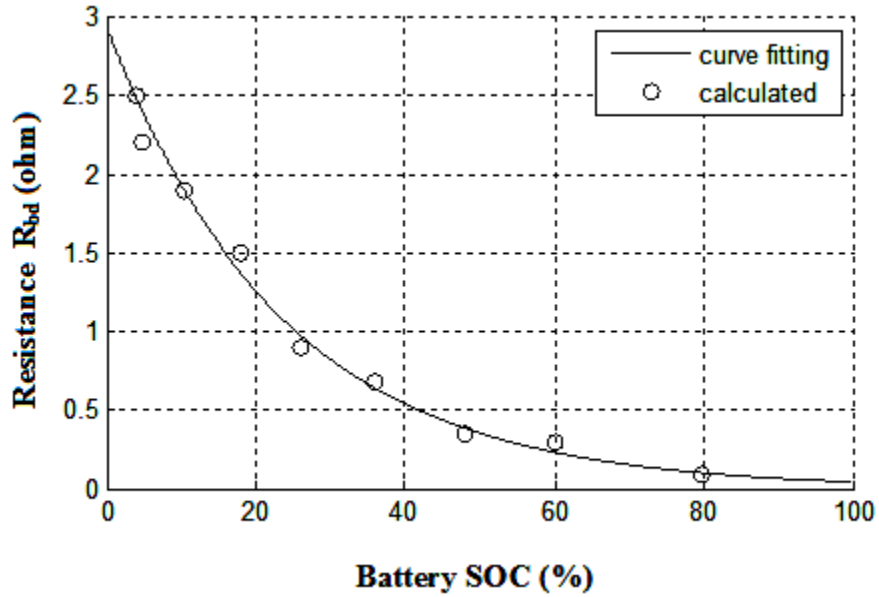


Figure 4.6 Variation in R_{bd} with the Battery SOC

4.3.4 Polarization Capacitance (C_{ov})

Based on the time constant and settling time of the terminal voltage response, the polarization capacitance C_{ov} can be estimated as [51]:

$$C_{ov} = \frac{t_{ov}}{5R_{bdi}} \quad (4.17)$$

where, t_{ov} is the settling time. From the discharge characteristics of the *Yuasa NP4-12* battery, given in Figure 4.4, it can be seen that the lower discharge rate curves have longer transient interval [51]-[52]. So, the capacitance C_{ov} is estimated according to the lowest discharge rate given in the data sheet. The settling time is considered to be one minute. As a result, for this battery, the overvoltage capacitance (C_{ov}) is obtained to be $40F$ [51].

4.3.5 Charging Polarization Resistance (R_{ch})

The battery terminal voltage during the charging process is given by equation (4.4) as [51]:

$$V_{br,Charging} = E_b + I_b R_{ch} \cdot \left[1 - \exp\left(\frac{-t}{R_{ch} \cdot C_{ov}}\right) \right] \quad (4.18)$$

The resistance (R_{ch}) during the charging process can be divided into two components as [51]:

$$R_{ch} = R_{bci} + R_{bc} \quad (4.19)$$

The resistance R_{bci} models the change in the terminal voltage from the battery emf during the transient interval, and hence, depends on the charging rate. The resistance R_{bc}

models the variation of the internal resistance with the battery SOC. The resistance R_{bci} can be estimated as [51]:

$$R_{bci} = \left. \frac{V_{bt} - E_b}{I_b} \right|_{t=5 \text{ min}} \quad (4.20)$$

With the above approximation, the value of 1.5Ω is obtained. After transients die away, the resistance R_{bc} can be expressed as [51]:

$$R_{bc} = \frac{V_{bt} - E_b}{I_b} - R_{bci} \quad (4.21)$$

The variation of R_{bc} with the battery SOC is shown in Figure 4.7.

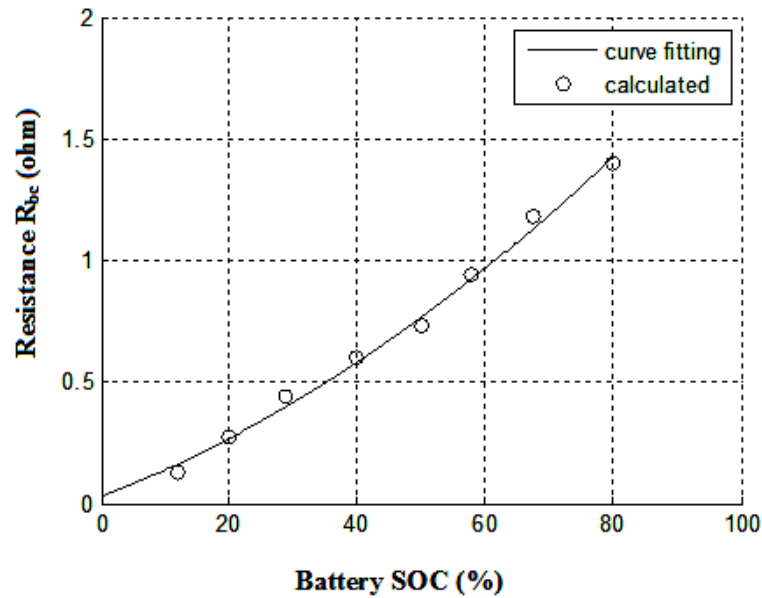


Figure 4.7 Variation in R_{bc} with the Battery SOC

To use the curve fitting technique, a quadratic expression selected to describe the variation of R_{bc} with the battery SOC is given as [51]:

$$R_{bc} = 9.32 \times 10^{-5} \cdot (SOC)^2 + 0.01 \cdot (SOC) + 0.028 \quad (4.22)$$

4.4 Validation of the Lead-Acid Battery Model

To validate the battery model, the model is simulated for two discharge rates – 0.2A and 0.4 A. The terminal voltage (V_{bt}) of the model is obtained in each case. This terminal voltage (V_{bt}) of the battery model is then compared with the discharge characteristics given in the manufacturing data sheet of the 12 V, 4 Ah *Yuasa battery* [52]. The validation results are shown in Figure 4.8. The ‘dotted line (---)’, shown in Figure 4.8, represents the discharge rates of the proposed battery model, while, the ‘solid line (–)’ represents the corresponding discharge rates from the manufacturer’s data sheet. The comparison shows a close match.

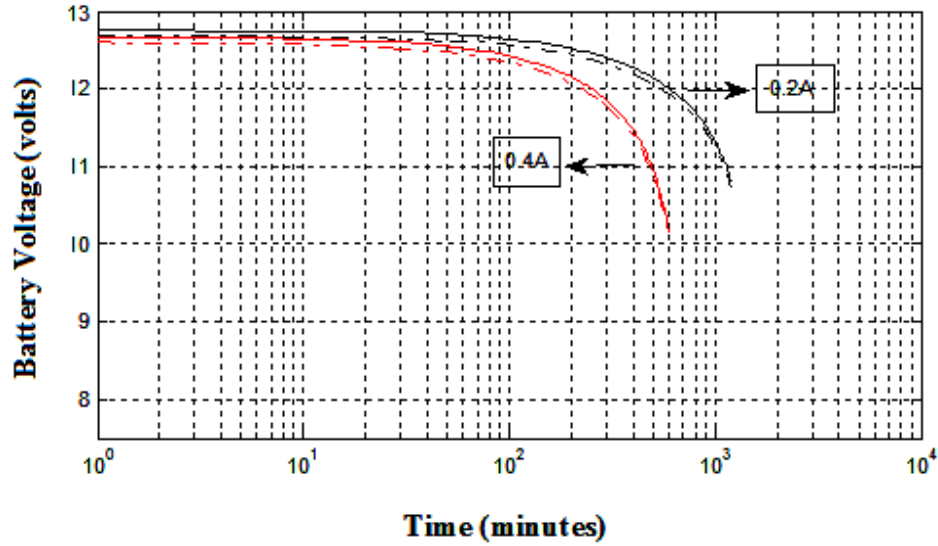


Figure 4.8 Validation of the Battery Model

4.5 Discharge Characteristics of the Battery Model

After the battery model is validated, the discharge characteristics of the model are obtained for four more values of the discharge rates – 0.2A ,0.4A ,0.8A ,1.2A . These discharge characteristics are shown in Figure 4.9. The corresponding change in the battery SOC during the discharge (from 100 % to 0%), is plotted in Figure 4.10. It can be seen, from Figures 4.9 and 4.10, that for the discharge rate of 0.2A , the battery SOC changes to 0% from 100% in 1200 minutes $\left[\frac{4Ah}{0.2A} = 20h = 20 \times 60 = 1200 \text{ min} \right]$. For the higher discharge rates (0.4A ,0.8A ,1.2A), the battery SOC takes lesser time to change to 0% from 100%. It is to be noted that the time-axis (x-axis) of Figures 4.8, 4.9 and 4.10 is in the logarithmic scale.

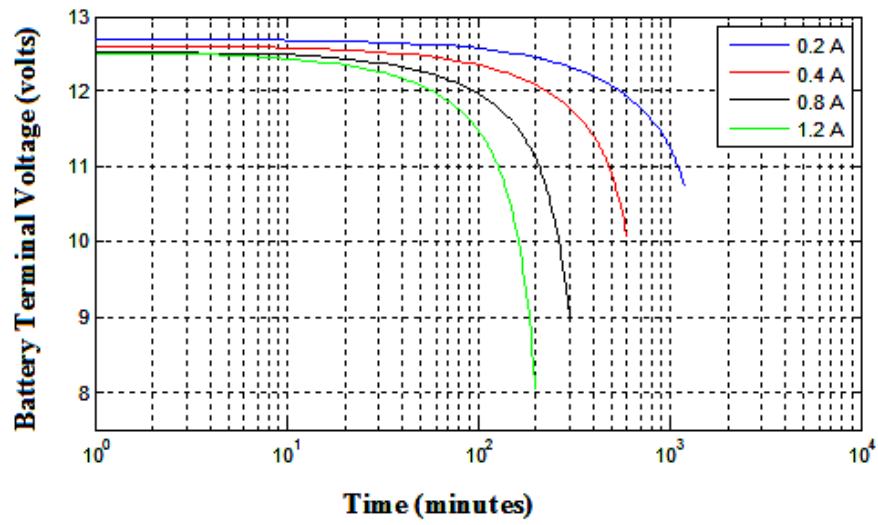


Figure 4.9 Discharge Characteristics of the Battery Model (12 V, 4Ah)

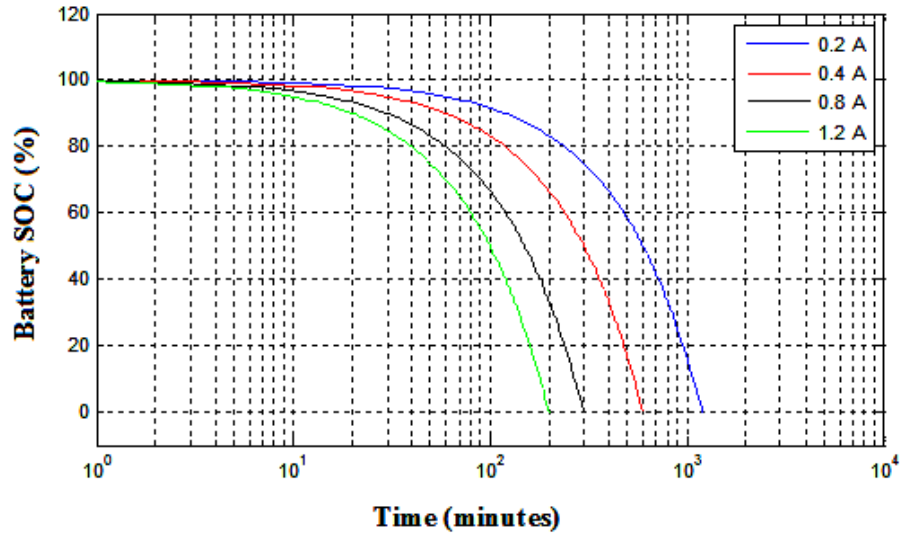


Figure 4.10 Variation in the Battery SOC for Different Discharge Currents

4.6 Scaling of the Battery Model for Different Battery Capacities

The parameters of the proposed battery model can be scaled to match with the other batteries with the different nominal capacities [51]. As all the batteries in the NP series (*from Yuasa*) have the same discharge characteristics for the discharge currents scaled in proportion to the nominal capacity, the fitting coefficients of the mathematical expressions of the proposed battery model can be scaled as [51]- [52]:

$$[R \text{ at } C_{n2}] = \frac{C_{n1}}{C_{n2}} [R \text{ at } C_{n1}] \quad (4.23)$$

and

$$[C_{ov} \text{ at } C_{n2}] = \frac{C_{n2}}{C_{n1}} [C_{ov} \text{ at } C_{n1}] \quad (4.24)$$

where, R refers to R_{sd} , R_{ch} and R_{dch} in the proposed battery model, C_{n1} is the nominal capacity of the battery modeled in this work (4Ah), and C_{n2} is the nominal capacity of any other battery required to be modeled. As the relationship between the battery emf (E_b) and battery SOC remains the same for all the batteries in the series, the coefficients of the emf equation (Equation 4.7) remain unchanged [51].

4.7 Design of the Battery Bank for the Fuel Cell-based DG System

For the PEM fuel cell-based DG system, the battery bank can be formed by connecting the individual lead-acid batteries together. The terminal voltage and capacity of the battery bank are determined based on requirements of the PEM fuel cell-based DG system considered in this research.

4.7.1 Determination of the Terminal Voltage of the Battery bank

To determine the terminal voltage of the battery bank, first, minimum dc bus voltage required for the proper operation of a three-phase dc/ac inverter is found. Equation (4.25) is used to determine the desired dc bus voltage [35], [53].

$$\frac{\sqrt{3}m_a}{2\sqrt{2}}V_{dc} \geq \sqrt{(V_{ac,L-L})^2 + 3(\omega L_f I_{\max})^2} \quad (4.25)$$

where, $V_{ac,L-L}$ is the ac side line-to-line rms voltage, L_f is the inductance of the L-C filter, I_{\max} is the rms value of maximum load current and m_a is the modulation index of the inverter. The linear PWM is used for the inverter, hence here $m_a \leq 1$.

The selected values of the parameters are:

$$V_{ac,L-L} = 208 \text{ V (120V}_{L-N}) , L_f = 10.2 \text{ mH} , I_{\max} = 100\text{A} , \omega = 2\pi.f = 377 \text{ rad/sec}$$

Substituting the values of the parameters into equation (4.26), we get:

$$V_{dc} \geq 390 \text{ V}$$

Therefore, the terminal voltage of the battery bank $V_{dc, \min imum} \geq 390 \text{ V}$

4.7.2 Determination of the Battery Bank Capacity

The capacity of the battery bank is determined based on the following specifications:

- a) Rated nominal power demand $\leq 5 \text{ kW}$
- b) Rated Peak Power demand $\leq 10 \text{ kW}$
- c) When fully charged (SOC = 100%), the terminal voltage of the battery bank \geq

$$V_{dc, \min imum}$$

d) The battery bank should be capable of providing the peak power demand continuously for 2 hrs.

Hence, the required energy capacity of the battery bank = $10 \text{ kW} \times 2\text{h} = 20000 \text{ Wh}$

The minimum terminal voltage of the battery bank = 390V

Required Ampere-hour (Ah) of the battery bank $\geq \frac{20000\text{Wh}}{390\text{V}} \geq 51.28\text{Ah}$

To satisfy the terminal voltage and energy capacity requirements, the battery bank is formulated by connecting 38 lead-acid batteries in series. Each battery in the battery bank has the terminal voltage between $12.6 - 12.8\text{V}$, and 90Ah capacity. Hence, the terminal voltage of the battery bank at a fully charged state (SOC =100%) is $V_{bat} = 480 \text{ V}$, and the energy capacity is 90Ah .

4.8 Summary Specifications

SOC (%)	E_b (V)	R_{sd} (k Ω)	R_{dch} (Ω) @ $I_b = 0.2\text{A}$	R_{ch} (Ω) @ $I_b = 0.2\text{A}$	C_{ov} (F)
100	12.875	17.77	0.9302	3.4600	40
80	12.6	72.77	0.9879	2.9245	40
60	12.325	96.57	1.1217	2.4635	40
40	12.05	89.17	1.4316	2.0771	40
20	11.775	50.57	2.1495	1.7653	40

Table 4.1 Parameters of 12 V, 4Ah Battery Model

SOC (%)	E_b (V)	R_{sd} (k Ω)	R_{dch} (Ω) @ $I_b = 0.2A$	R_{ch} (Ω) @ $I_b = 0.2A$	C_{ov} (F)
100	12.875	17.77	0.9302	3.4600	40
80	12.6	72.77	0.9879	2.9245	40
60	12.325	96.57	1.1217	2.4635	40
40	12.05	89.17	1.4316	2.0771	40
20	11.775	50.57	2.1495	1.7653	40

Table 4.2 Parameters of 480 V, 90Ah Battery Bank

This section lists the summary specifications of a 12 V, 4Ah lead-acid battery along with the specifications of a 12V, 90Ah battery bank designed for the PEM fuel cell based DG system. The Table 4.1 summarizes the parameters of a 12 V, 4Ah battery model and Table 4.2 summarizes the parameters of an individual battery, with energy capacity 90 Ah, used in the battery bank.

4.9 Determination of the Discharge Characteristics of 480 V, 90 Ah Battery Bank

To analyze the response of a 480V, 90Ah battery bank to different loads, the discharge characteristics of the battery are determined by connecting a resistive load box to the battery bank terminals as shown in Figure 4.11. The six different values of resistive loads – 5 Ω , 10 Ω , 25 Ω , 50 Ω , 75 Ω , 100 Ω – are used to obtain the characteristics. The corresponding values of the discharge currents are: 96A, 48A, 19.2A, 9.6A, 6.4A, 4.8A. These discharge characteristics are shown in Figure 4.13. The corresponding change in the battery bank's SOC is shown in Figure 4.13.

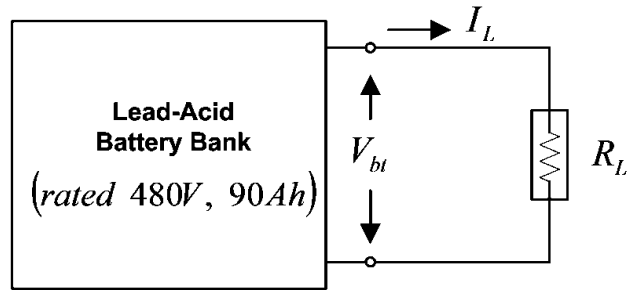


Figure 4.11 Block Diagram for Determining the Discharge Characteristics of the Battery Bank

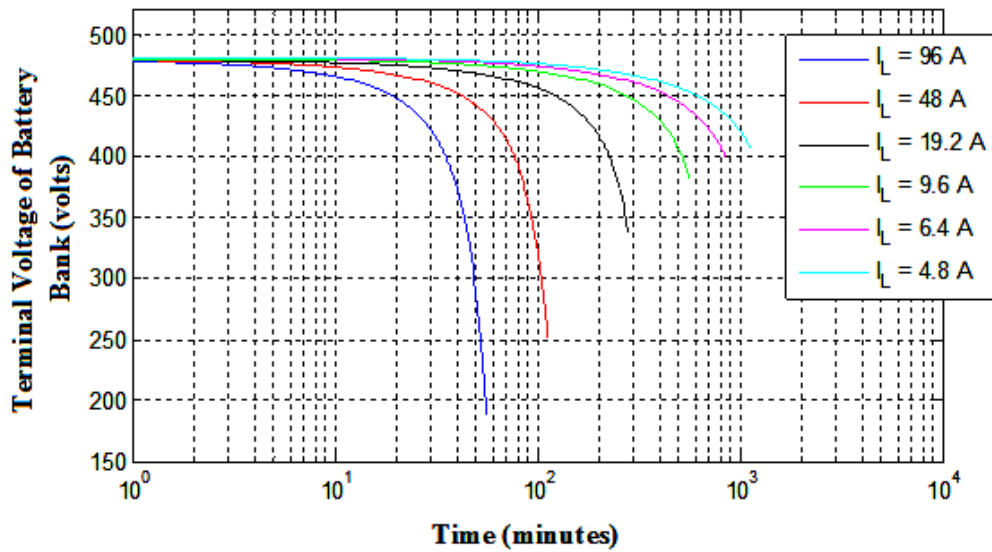


Figure 4.12 Discharge Characteristics of the Battery Bank

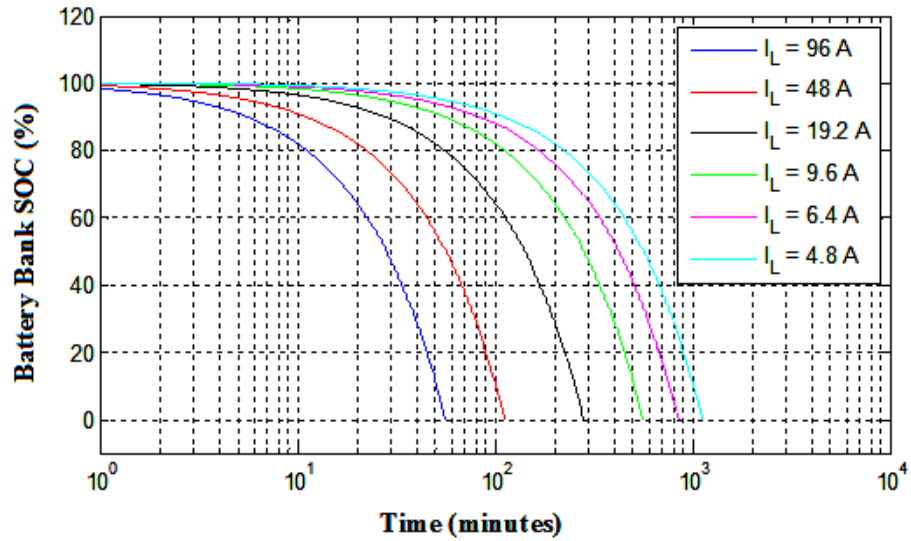


Figure 4.13 Variation in the SOC of the Battery Bank during Discharging

4.10 Control of the DC/DC Boost Converter

To perform charging of the battery bank, the output voltage of the PEM fuel cell array is stepped up using the dc/dc boost converter. The typical value of the output voltage of the PEM fuel cell array is between 45-75 V. This voltage is stepped up to $V_{bat} = 480 V$ which is the desired dc bus voltage of the battery bank.

The topology of the dc/dc boost converter is shown in Figure 4.14 [35], [44], [53]. The inductor current $i_{L,bc}$ and capacitor voltage $v_{c,bc}$ are selected as state variables for the model. The input $u_{bc} = V_{fc}$ is the output of the PEM fuel cell array, and u is the duty cycle of the boost converter.

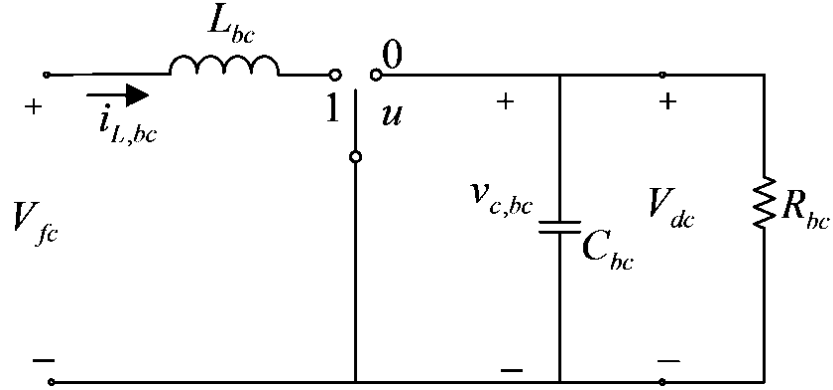


Figure 4.14 The DC/DC Boost Converter

The dynamic model of the boost converter based on the state space averaging technique can be given as [35], [44], [53]:

$$\begin{aligned} \dot{x}_{1bc} &= -(1-u) \frac{1}{L_{bc}} x_{2bc} + \frac{V_{fc}}{L_{bc}} \\ \dot{x}_{2bc} &= (1-u) \frac{1}{C_{bc}} x_{1bc} - \frac{1}{R_{bc} C_{bc}} x_{2bc} \end{aligned} \quad (4.26)$$

where, $x_{1bc} = i_{L,bc}$ and $x_{2bc} = v_{c,bc}$

$$\Rightarrow A_{bc} = \begin{bmatrix} 0 & \frac{-(1-u)}{L_{bc}} \\ \frac{(1-u)}{C_{bc}} & \frac{-1}{R_{bc} C_{bc}} \end{bmatrix}, \quad B_{bc} = \begin{bmatrix} \left(\frac{1}{L_{bc}} \right) \\ 0 \end{bmatrix}, \quad u_{bc} = V_{fc}$$

The parameters of the dc/dc boost converter model are listed below:

$$L_{bc} = 5 \text{ mH} , C_{bc} = 300 \text{ } \mu\text{F} , R_{bc} = 40 \text{ } \Omega , V_{dc,ref} = 480 \text{ V}$$

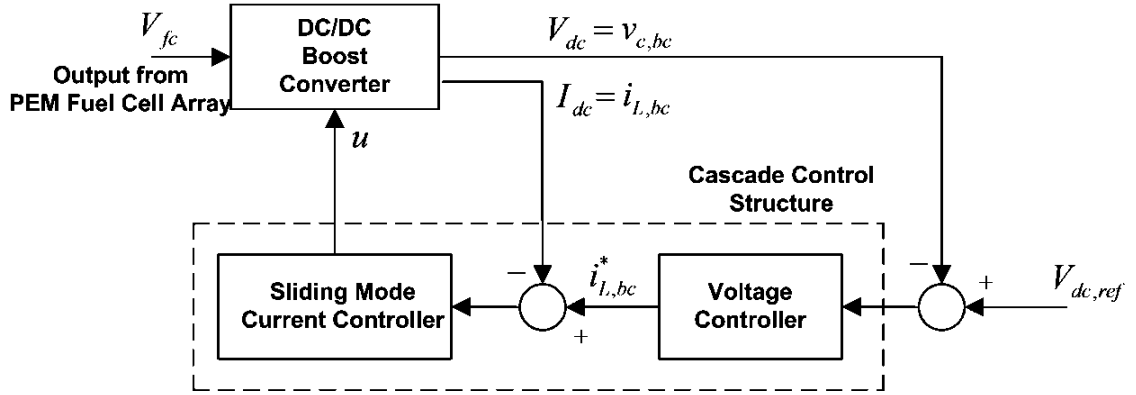


Figure 4.15 Block Diagram of the Sliding Mode Control Design for the DC/DC Boost Converter

The control development is performed to regulate the output voltage of the dc/dc boost converter at $V_{dc,ref} = 480 \text{ V}$. The block diagram of the proposed sliding mode control design is shown in Figure 4.15 [44]. The goal of the control design is to achieve a constant output voltage $V_{dc,ref}$

$$\text{i.e. } x_{2bc} = V_{dc,ref}$$

$$\Rightarrow \dot{x}_{2bc} = \dot{V}_{dc,ref} = 0 \quad (4.27)$$

To design the sliding mode control law, it is assumed that x_{1bc} in equation (4.26) can be handled as a control input. The control goal shown by equation (4.27) is substituted into the voltage loop equation. I.e. the second equation of (4.26), to yield the desired current as follows [44]:

$$(1-u) \frac{1}{C_{bc}} x_{1bc}^* = \frac{1}{RC_{bc}} x_{2bc} \quad (4.28)$$

$$\Rightarrow x_{1bc}^* = \frac{V_{dc,ref}}{(1-u)R} \quad (4.29)$$

To ensure that the actual current x_{1bc} exactly tracks the desired current x_{1bc}^* , the sliding surface is chosen as [44]:

$$S = x_{1bc} - x_{1bc}^* \quad (4.30)$$

To enforce sliding mode in the manifold $s = 0$, the control u can be defined as [44]:

$$u = \frac{1}{2}[1 - \text{sign}(s)] \quad (4.31)$$

The equivalent control of u is derived by solving $\dot{s} = 0$:

$$\dot{s} = \dot{x}_{1bc} = 0 \quad (4.32)$$

$$\Rightarrow (1 - u_{eq}) \frac{1}{L_{bc}} x_{2bc} = \frac{V_{fc}}{L_{bc}} \quad (4.33)$$

$$\Rightarrow (1 - u_{eq}) = \frac{V_{fc}}{x_{2bc}} \quad (4.34)$$

$$u_{eq} = 1 - \frac{V_{fc}}{x_{2bc}} \quad (4.35)$$

Substituting equation (4.35) into equation (4.28), we get the desired current as:

$$x_{1bc}^* = \frac{V_{dc,ref}^2}{R_{bc} \cdot V_{fc}} \quad (4.36)$$

x_{2bc} is the output voltage of the slow voltage loop. The motion equation of the outer voltage is obtained by substituting the equivalent control and desired current into the second equation of (4.26) [44]:

$$\dot{x}_{2bc} = \left[1 - \left(1 - \frac{V_{fc}}{x_{2bc}} \right) \right] \cdot \frac{1}{C_{bc}} \cdot (x_{1bc}^*) - \frac{1}{R_{bc} C_{bc}} x_{2bc}$$

$$\dot{x}_{2bc} = \left(\frac{V_{fc}}{x_{2bc}} \right) \cdot \frac{1}{C_{bc}} \cdot (x_{1bc}^*) - \frac{1}{R_{bc} C_{bc}} x_{2bc}$$

$$\dot{x}_{2bc} = -\frac{1}{R_{bc} \cdot C_{bc}} \left(x_{2bc} - \frac{V_{dc,ref}^2}{x_{2bc}} \right) \quad (4.37)$$

As long as the output voltage of the dc/dc boost converter is higher than the input voltage of the converter, a sliding mode control law can be enforced. This is an imperative requirement to guarantee the convergence to $s = 0$ [44]. Since, in the PEM fuel cell based DG system, desired dc bus voltage (480V) is always higher than the output voltage of the PEM fuel cell, the sliding mode control law can always be enforced.

4.11 Simulation of the PEM Fuel Cell Array with the DC/DC Boost Converter

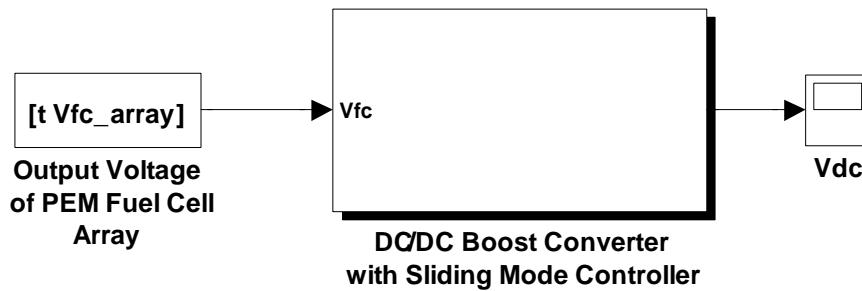


Figure 4.16 Simulation of the DC/DC Boost Converter in MATLAB/Simulink

The output voltage of the PEM fuel cell array is fed to the dc/dc boost converter and the system is simulated in MATLAB/Simulink. The block diagram of the simulation is shown in Figure 4.16. Figure 4.17 shows the implementation of the sliding mode control for dc/dc converter in MATLAB/Simulink.

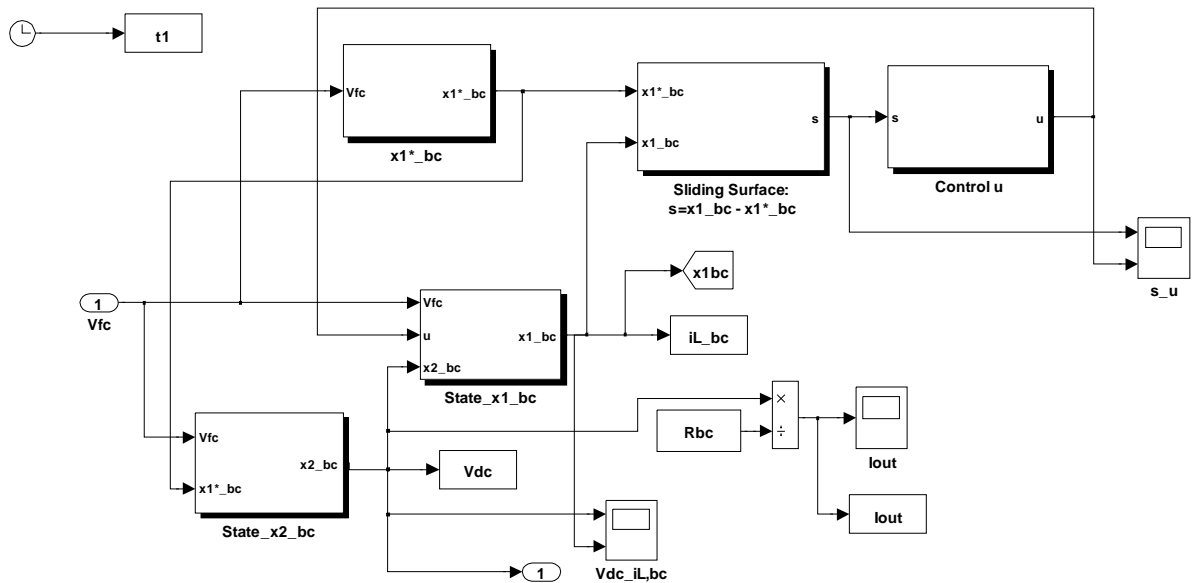


Figure 4.17 DC/DC Boost Converter with the Sliding Mode Controller in MATLAB/Simulink

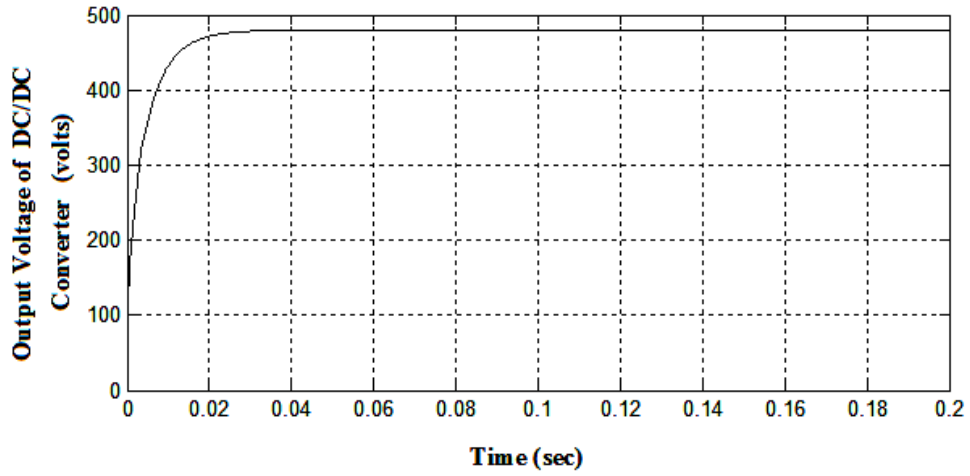


Figure 4.18 Output Voltage of the DC/DC Boost Converter

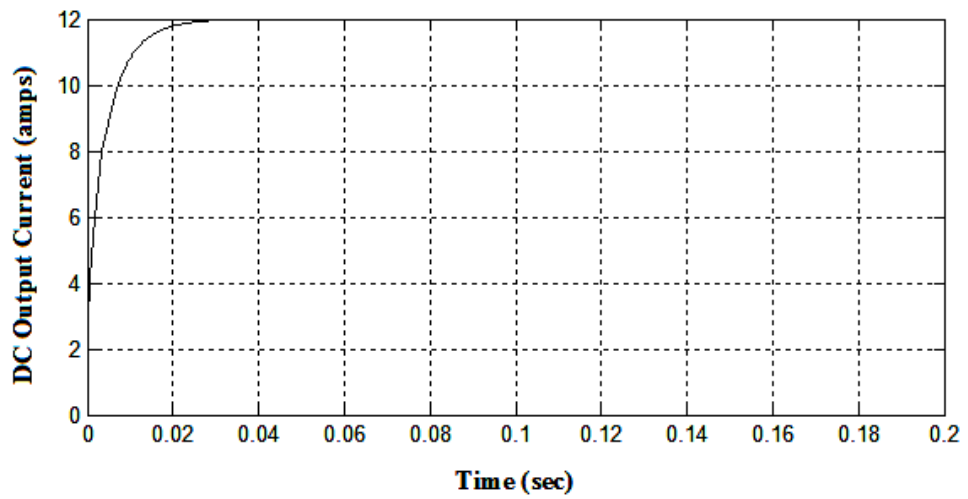


Figure 4.19 DC Output Current

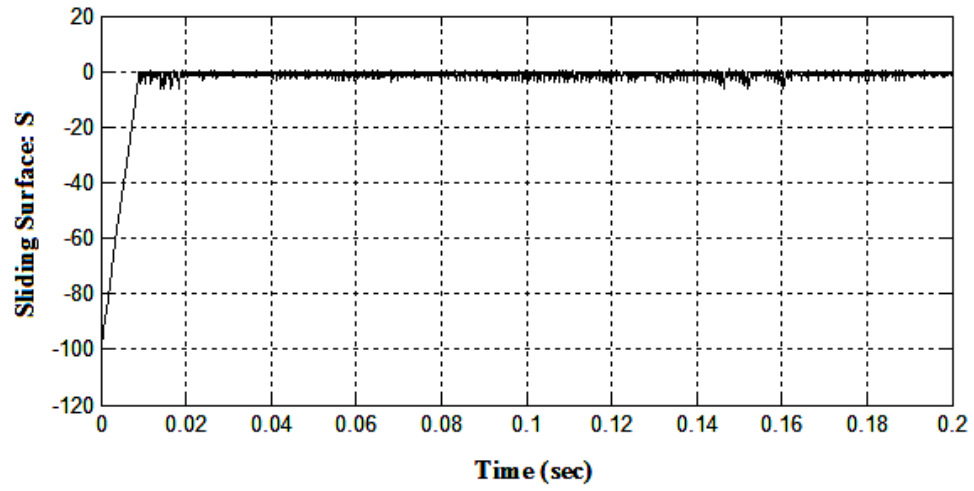


Figure 4.20 Sliding Surface $S = x_{1bc} - x_{1bc}^* = 0$

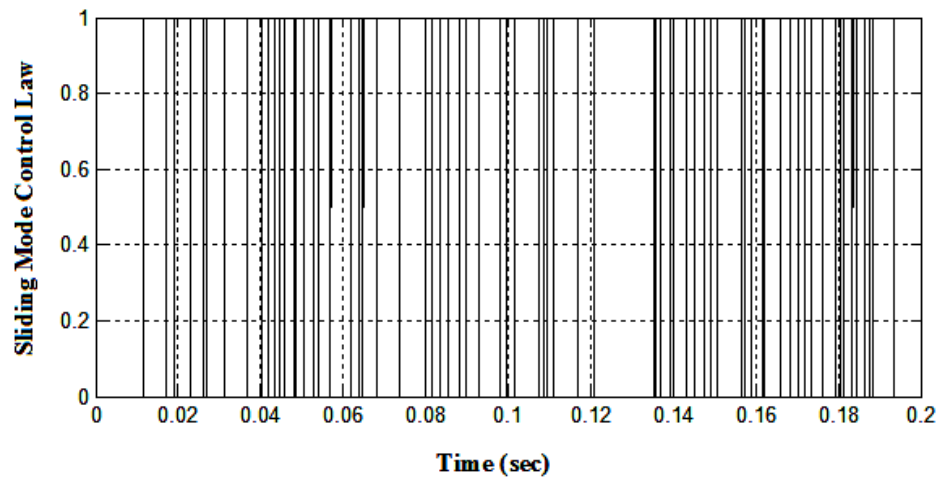


Figure 4.21 Sliding Mode (Equivalent Control u_{eq}) Control Switching Pattern

4.12 Charging of 480V, 90Ah Lead-Acid Battery Bank

The charging of the battery bank for three different charging currents (12A, 18A and 25.5A) is shown in Figures 4.22, 4.24 and 4.26, respectively. Variation in the corresponding battery SOC during charging is shown in Figures 4.23, 4.25 and 4.27, respectively. It can be observed that for the higher values of the charging currents, the charging time is lesser. For the charging current of a 12 A, the battery bank can be charged from 0-100% SOC in 450 minutes while, with the charging current of a 25.5 A, battery bank can be charged from 0-100% SOC in 212 minutes.

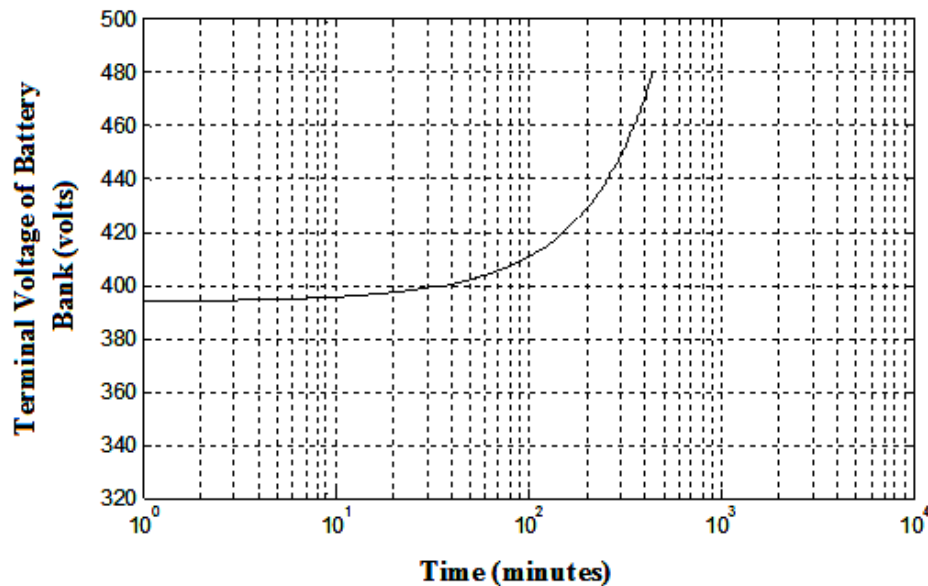


Figure 4.22 Charging Characteristics of the Battery Bank (with charging current = 12A, charging time = 450 minutes)

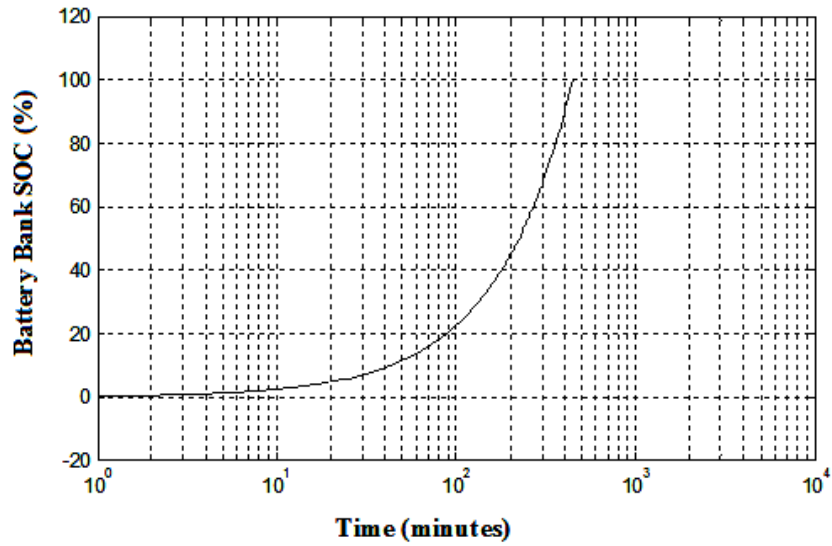


Figure 4.23 Variation in the SOC of the Battery Bank (**Case I**: charging current = 12A)

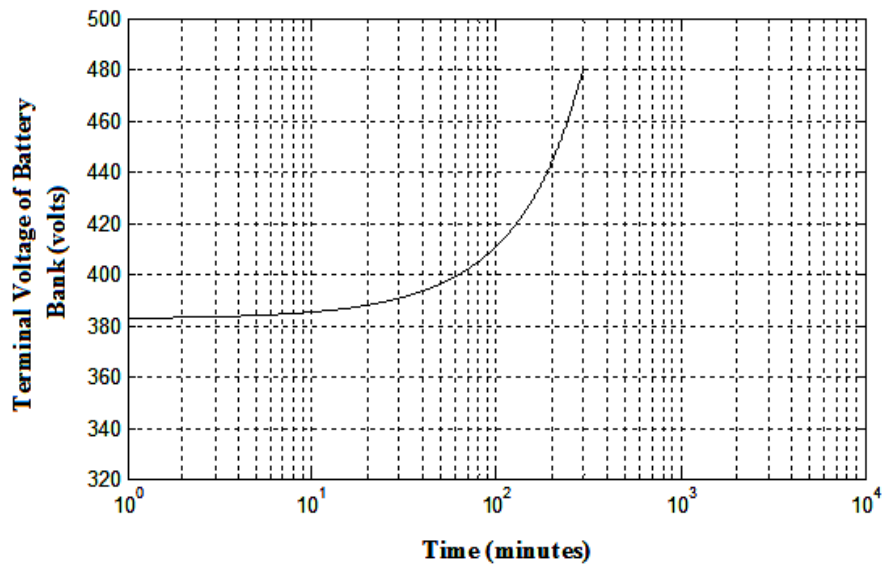


Figure 4.24 Charging Characteristics of the Battery Bank (with charging current = 18A, charging time = 300 minutes)

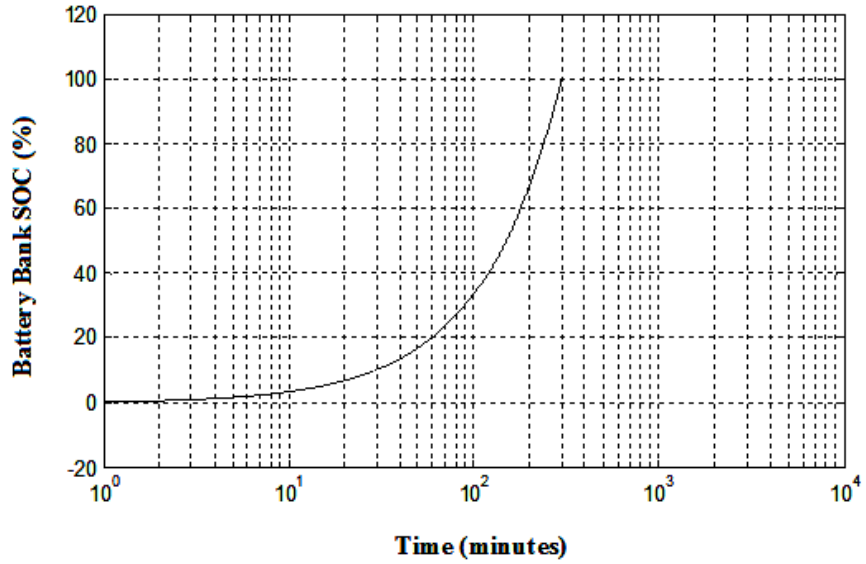


Figure 4.25 Variation in the SOC of the Battery Bank (**Case II**: charging current = 18A)

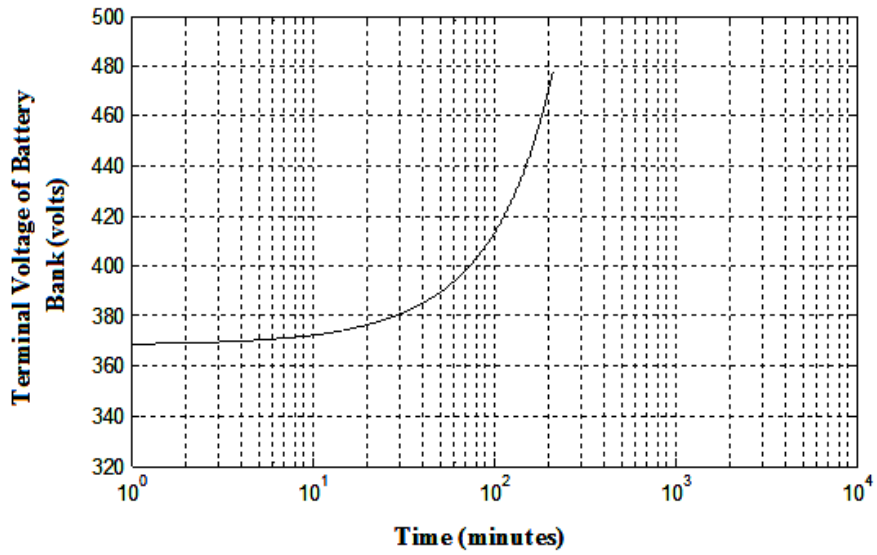


Figure 4.26 Charging Characteristics of the Battery Bank (with charging current = 25.5A, charging time = 212 minutes)

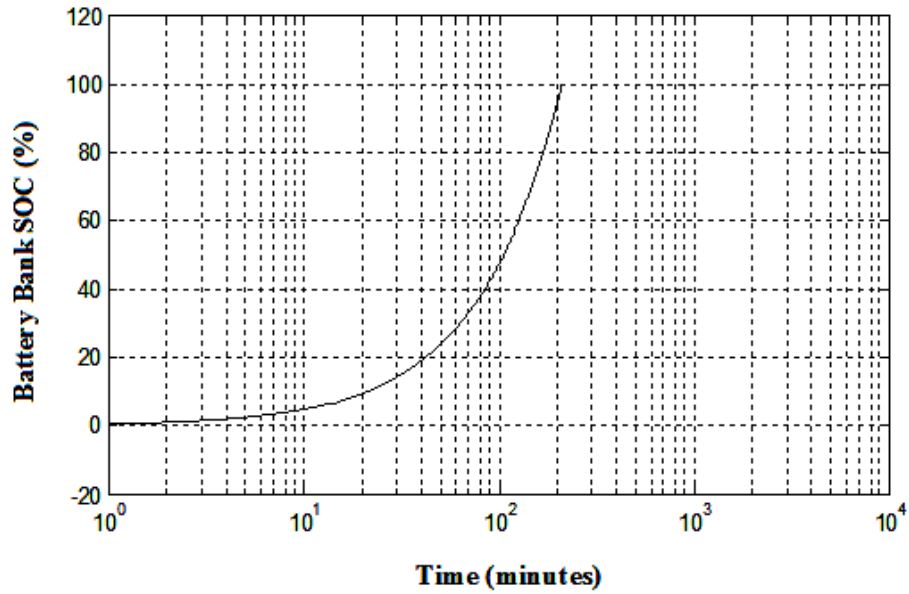


Figure 4.27 Variation in the SOC the Battery Bank (**Case III**: charging current = 25.5A)

4.13 Chapter Summary

In this chapter, a lead-acid battery bank, for the DG system, is designed with the terminal voltage rating of 480 V, and the ampere-hour capacity of 90 Ah.

First, a model of 12 V, 4 Ah lead-acid battery is presented. All the parameters of the battery model are identified, using curve fitting technique, and the manufacturer's data sheet for *NP4-12 YUASA* battery. The discharge characteristics of the battery model are studied. The dc bus voltage required for the proper operation of the dc/ac inverter is then determined, and the terminal voltage of the battery bank is determined.

A 12 V, 4 Ah battery model is then scaled to design the battery bank. The parameters of the 480 V, 90 Ah battery bank are then found and the discharge characteristics of the

battery bank are determined for the different values of discharge currents.

The sliding mode control law is designed for the dc/dc boost converter to control its output voltage. Using models of the PEM fuel cell array and dc/dc boost converter, charging of the battery bank is simulated in MATLAB/Simulink.

CHAPTER 5

CONTROL OF A SINGLE PHASE AND THREE-PHASE INVERTER

5.1 Introduction

In this chapter, the application of two different control strategies to a single-phase and three-phase is analyzed. The objective of the control design is to achieve low THD output voltage, fast transient response, and asymptotic tracking of the reference output voltage under linear and nonlinear loads, minimizing the effect of the harmonic frequencies. First, the proportional-integral-derivative (PID) control technique is used to design the voltage and current controllers for the single-phase and three-phase inverter. The second control technique – the robust servomechanism problem (RSP) voltage controller with the sliding mode current controller – is then designed. The performance of the single-phase and three-phase inverter under these control strategies is compared, and the results are shown.

The control design is performed in a discrete-time domain. For both techniques, the controller structure is defined, necessary controller parameters are determined, and the simulation of a closed-loop system is performed in MATLAB/Simulink.

5.2 Model of a Single-Phase Inverter

Figure 5.1 shows the schematic diagram of a single phase full-bridge inverter system with R-L load. The parameters of the system are given in Table 5.1.

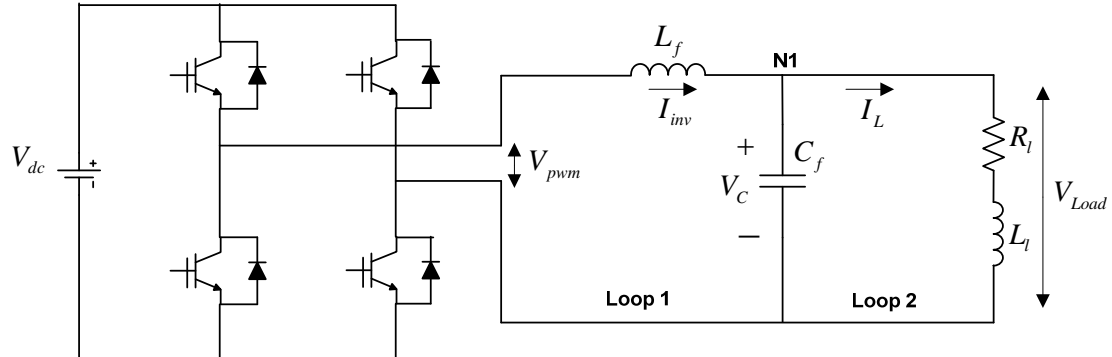


Figure 5.1 Single-Phase Full-Bridge Inverter

$L_f = 25 \text{ mH}$	Modulation index = 0.8
$C_f = 100 \text{ } \mu\text{F}$	$V_{dc} = 300 \text{ V}$
PWM (carrier) frequency = 4 kHz	$R_l = 5.55 \text{ } \Omega$
Fundamental frequency: $f_1 = 60 \text{ Hz}$	$L_l = 15 \text{ mH}$

Table 5.1 Parameters of the Single-Phase Full-Bridge Inverter

The continuous-time state space model of the single-phase inverter, shown in Figure 5.1, can be given as:

$$\begin{aligned} \dot{x}_p &= A_p \cdot x_p + B_p \cdot u \\ y &= C_p \cdot x_p + D_p \cdot u \end{aligned} \quad (5.1)$$

$$\text{Where, } A_p = \begin{bmatrix} 0 & \left(\frac{1}{C_f}\right) & \left(-\frac{1}{C_f}\right) \\ \left(-\frac{1}{L_f}\right) & 0 & 0 \\ \left(\frac{1}{L_l}\right) & 0 & \left(-R_l/L_l\right) \end{bmatrix}, \quad B_p = \begin{bmatrix} 0 \\ \left(\frac{1}{L_f}\right) \\ 0 \end{bmatrix}, \quad x_p = \begin{bmatrix} V_C \\ I_{inv} \\ I_L \end{bmatrix}$$

$$C_p = \begin{bmatrix} 1 & 0 & 0 \\ 0 & 1 & 0 \\ 0 & 0 & 1 \end{bmatrix}, \quad u = V_{pwm}, \quad D_p = \begin{bmatrix} 0 \\ 0 \\ 0 \end{bmatrix}$$

To discretize the model given by equation (5.1), the sampling time selected is the reciprocal of the PWM switching frequency [12]-[13].

$$\Rightarrow T_s = \frac{1}{\text{PWM Switching frequency}} = \frac{1}{4000} = 2.5 * 10^{-4} \text{ sec}$$

The discrete-time state space model of the single-phase inverter, shown in Figure 5.1, can be given as:

$$\begin{aligned} x_p(k+1) &= A_{pd} \cdot x_p(k) + B_{pd} \cdot u(k) \\ y(k) &= C_{pd} \cdot x_p(k) + D_{pd} \cdot u(k) \end{aligned} \quad (5.2)$$

$$\text{Where, } A_{pd} = e^{A_p \cdot T_s}, \quad B_{pd} = \int_0^{T_s} e^{A_p \cdot (T_s - \tau)} \cdot B_p \cdot d\tau, \quad C_{pd} = C_p, \quad D_{pd} = D_p, \quad u(k) = V_{pwm}$$

5.3. Control Development for the Single-Phase Inverter

In power inverter topologies, the rate of change of current is greater than the rate of change of voltage. It is shown in the literature that, for these type of systems, cascade

dual loop control structure (outer voltage loop and inner current loop) can be effectively designed [44]. First, the voltage error signal ($e_v = V_{ref} - V_{Load}$) is given to the outer voltage loop, which controls the load voltage V_{Load} by making it follow 60 Hz sinusoidal voltage reference V_{ref} . This outer loop then generates the reference signal (inverter current reference I_{ref}) for the inner current loop. The inner current loop, subsequently, generates the PWM voltage command [12]-[13].

The main objectives of the control design are to achieve: (i) Low THD voltage output (< 2%), (ii) Low load and voltage regulation (<5%), (iii) Zero steady state error (iv) Fast transient response

5.4 Discrete-time PID Voltage and Current Control Design

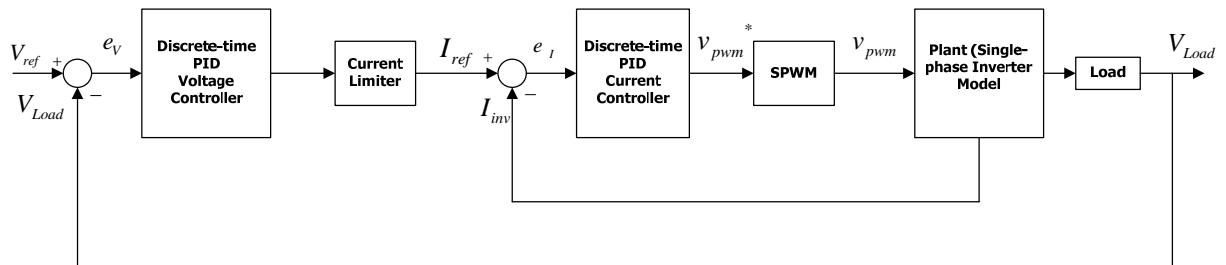


Figure 5.2 Control Block Diagram of the Discrete-time PID Voltage and Current Control for Single-Phase Inverter

First, the PID controller is used in the outer voltage loop, as well as in the inner current loop, and the control design is tested for different loading conditions. The advantage of using the PID controller, is its simplicity, and ease of implementation. The

control block diagram of the discrete-time PID voltage and current control design is shown in Figure 5.2.

The standard transfer function of the PID controller, in continuous-time domain, is given as [70]:

$$u(s) = K_p + \frac{K_i}{s} + K_d \cdot s \quad \Rightarrow \quad u(s) = \frac{K_d \cdot s^2 + K_p \cdot s + K_i}{s} \quad (5.3)$$

The controller has two zeros, and a single pole. In the discrete-time domain (z-domain), a transfer function of the PID controller can be given as [70]:

$$u(z) = K_p + K_i \cdot \frac{T_s}{2} \cdot \left(\frac{z+1}{z-1} \right) + K_d \cdot \left(\frac{z-1}{T_s \cdot z} \right)$$

$$\Rightarrow u(z) = \frac{a_0 \cdot z^2 + a_1 \cdot z + a_2}{z(z-1)} \quad (5.4)$$

Where, $a_0 = \left[K_p + \frac{K_i \cdot T_s}{2} + \frac{K_d}{T_s} \right]$, $a_1 = \left[-K_p + \frac{K_i \cdot T_s}{2} - \frac{2 \cdot K_d}{T_s} \right]$, $a_2 = \left[\frac{K_d}{T_s} \right]$

The discrete-time PID voltage controller block and the discrete-time PID current controller block are shown by Figures 5.3 and 5.4, respectively.

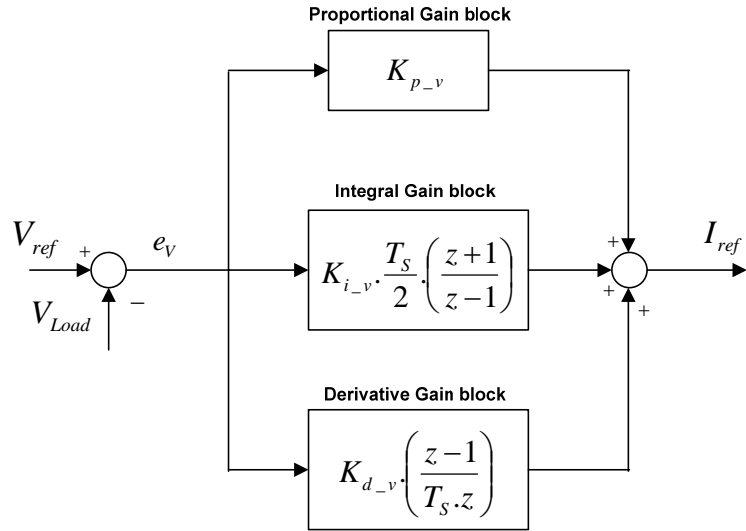


Figure 5.3 Discrete-time PID Voltage Controller for the Single-Phase Inverter

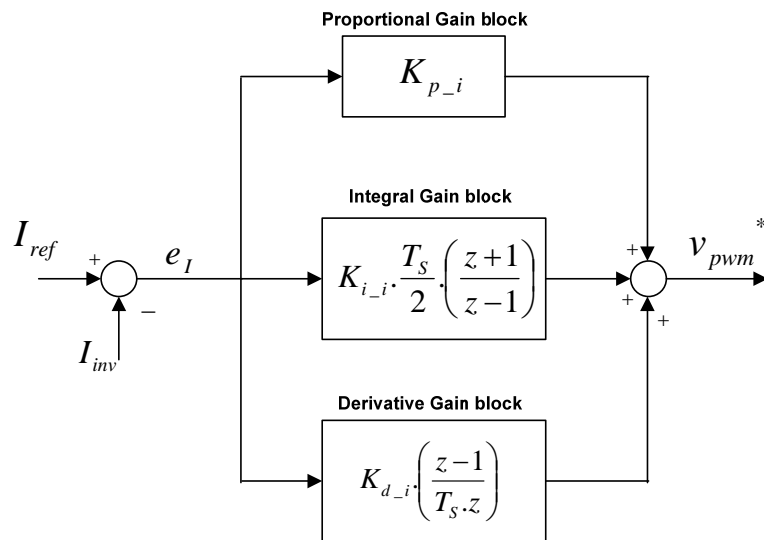


Figure 5.4 Discrete-time PID Current Controller for the Single-Phase Inverter

5.5 Discrete-time Robust Servomechanism Problem (RSP) Voltage Control and Discrete-time Sliding Mode Current Control Design

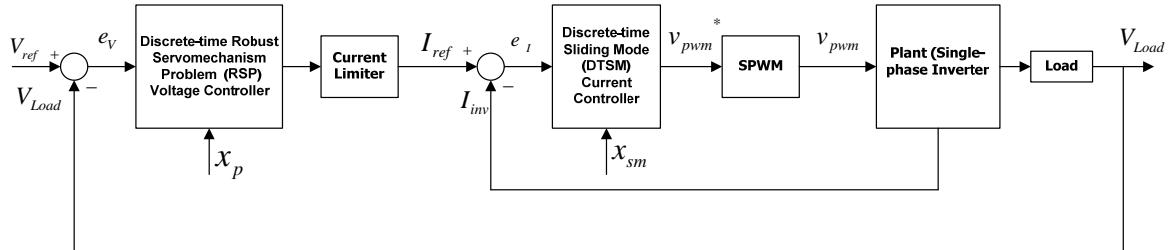


Figure 5.5 Control Block Diagram of the Discrete-time RSP Voltage Control and Discrete-time Sliding Mode Current Control for the Single-Phase Inverter

In the second control approach, the discrete-time robust servomechanism problem (RSP) voltage controller is used in the outer loop, and the discrete-time sliding mode current controller is used in the inner loop. The control block diagram of the proposed control strategy is shown in Figure 5.5 [12]-[13].

5.5.1 Design Steps for the Discrete-time RSP Voltage Controller and Discrete-time Sliding Mode Current Controller

When control design is performed in a cascade dual loop control structure, always the inner-loop controller is designed first, and the outer-loop controller is designed later. The following steps are used to design these controllers[12]-[13]:

Step 1: First, the discrete-time sliding mode current controller is designed.

Step 2: The overall system for the RSP voltage controller is obtained by combining a true plant (single-phase inverter) model, with the discrete-time sliding mode current controller

designed in the first step. Since, the RSP voltage controller is in the outer loop, the overall system for the RSP voltage controller is the combination of a true plant (single-phase inverter), and the discrete-time sliding mode current controller [12]-[13].

Step 3: Finally, the discrete-time RSP voltage controller design is performed. The details of these design steps are explained below.

5.5.2 Step 1 - Design of the Discrete-time Sliding Mode Current Controller

To design the discrete-time sliding mode current controller, the single-phase inverter is considered without any load. The load current I_L is treated as a disturbance [12]. Equation (5.5) gives the continuous-time single-phase inverter plant for the sliding mode current controller.

$$\begin{aligned} \dot{x}_{sm} &= A_{sm} x_{sm} + B_{sm} u + E_{sm} d \\ y &= C_{sm} x_{sm} \end{aligned} \quad (5.5)$$

$$\begin{aligned} \text{Where, } A_{sm} &= \begin{bmatrix} 0 & \left(\frac{1}{C_f}\right) \\ \left(-\frac{1}{L_f}\right) & 0 \end{bmatrix}, \quad B_{sm} = \begin{bmatrix} 0 \\ \left(\frac{1}{L_f}\right) \end{bmatrix}, \quad x_{sm} = \begin{bmatrix} V_C \\ I_{inv} \end{bmatrix} \\ E_{sm} &= \begin{bmatrix} \left(-\frac{1}{C_f}\right) \\ 0 \end{bmatrix}, \quad C_{sm} = [0 \quad 1], \quad d = I_L \end{aligned}$$

Equation (5.5) can be discretized as :

$$x_{sm}(k+1) = A_{smd} x_{sm}(k) + B_{smd} u(k) + E_{smd} d(k) \quad (5.6)$$

$$y(k) = C_{smd}(k) x_{sm}(k)$$

$$\text{Where, } A_{smd} = e^{A_{sm} T_s}, \quad B_{smd} = \int_0^{T_s} e^{A_{sm}(T_s-\tau)} B_{sm} d\tau, \quad E_{smd} = \int_0^{T_s} e^{A_{sm}(T_s-\tau)} E_{sm} d\tau$$

The inverter current (I_{inv}) is made to follow the current reference (I_{ref}) by selecting a sliding surface as [12], [44]:

$$\bar{s}(k) = y(k) - y_{ref}(k) \quad (5.7)$$

$$\therefore \bar{s}(k) = C_{smd}(k) \cdot x_{sm}(k) - I_{ref}(k)$$

$$\Rightarrow \bar{s}(k) = I_{inv}(k) - I_{ref}(k)$$

The sliding surface $\bar{s}(k)$ is selected, such that when the sliding mode exists, we have,

$$\bar{s}(k) = 0 \quad \text{or} \quad I_{inv} = I_{ref} \quad (5.8)$$

The sliding mode can be reached if the control input $u(k)$ is designed to be the solution of

$$: \quad \bar{s}(k+1) = y(k+1) - y_{ref}(k+1) = 0 \quad (5.9)$$

A control law that satisfies equation (5.9) is known as an equivalent control, and can be given as follows [12], [13], [44]:

$$\bar{s}(k+1) = y(k+1) - y_{ref}(k+1) = C_{smd} \cdot x_{sm}(k+1) - I_{ref} = 0$$

Substituting $x_{sm}(k+1)$ from equation (5.6), we get,

$$u_{eq}(k) = (C_{smd} \cdot B_{smd})^{-1} \cdot [I_{ref} - C_{smd} \cdot A_{smd} \cdot x_{sm}(k) - C_{smd} \cdot E_{smd} \cdot d(k)] \quad (5.10)$$

Thus, the discrete-time sliding mode control law, to be implemented in the inner control loop, is described by equation (5.10).

5.5.3 Step 2 - Formulation of the Plant for the Discrete-time RSP Voltage Controller

To design the RSP voltage controller, the system to be controlled by the RSP voltage controller needs to be known. Since, the RSP voltage controller is in the outer loop of the control structure, shown by Figure 5.5, the equivalent plant seen by the RSP voltage

controller is the combination of a true plant (single-phase inverter with load), with the discrete-time sliding mode current controller [12]-[13].

Therefore, to formulate the equivalent plant seen by the RSP voltage controller, equation (5.2), which represents single-phase inverter with load, and equation (5.6), which represents the discrete-time sliding mode current controller, need to be combined.

The sliding mode control law, given by equation (5.10), is the control input for the single-phase inverter given by equation (5.2). Hence, substituting equation (5.10) into equation (5.2) we get,

$$x_p(k+1) = A_{pd} \cdot x_p(k) - B_{pd} \cdot (C_{smd} \cdot B_{smd})^{-1} [(C_{smd} \cdot A_{smd} \cdot x_{sm}(k)) + (C_{smd} \cdot E_{smd} \cdot d(k))] + B_{pd} \cdot (C_{smd} \cdot B_{smd})^{-1} \cdot u_1(k) \quad (5.11)$$

Where, $u_1(k) = I_{ref}$

Now, we define: $C_{11} = \begin{bmatrix} 1 & 0 & 0 \\ 0 & 1 & 0 \end{bmatrix}$ and $C_{22} = [0 \ 0 \ 1]$

With C_{11} and C_{22} defined as above, we can write

$$x_{sm}(k) = C_{11} \cdot x_p(k) \quad \text{And} \quad d(k) = C_{22} \cdot x_p(k) \quad (5.12)$$

Where, $x_{sm} = [V_C \ I_{inv}]^T$, $x_p = [V_C \ I_{inv} \ I_L]^T$, $d = I_L$

Equation (5.11) can then be rewritten as,

$$x_p(k+1) = \{A_{pd} - B_{pd} \cdot (C_{smd} \cdot B_{smd})^{-1} [(C_{smd} \cdot A_{smd} \cdot C_{11}) + (C_{smd} \cdot E_{smd} \cdot C_{22})\} x_p(k) + B_{pd} \cdot (C_{smd} \cdot B_{smd})^{-1} \cdot u_1(k) \quad (5.13)$$

$$\Rightarrow x_p(k+1) = A_d \cdot x_p(k) + B_d \cdot u_1(k) \quad (5.14)$$

Where, $A_d = A_{pd} - B_{pd} \cdot (C_{smd} \cdot B_{smd})^{-1} [(C_{smd} \cdot A_{smd} \cdot C_{11}) + (C_{smd} \cdot E_{smd} \cdot C_{22})]$

$$B_d = B_{pd} \cdot (C_{smd} \cdot B_{smd})^{-1}, u_1(k) = I_{ref}$$

Thus, equation (5.14) represents an equivalent plant, for which the discrete-time RSP voltage controller is to be designed.

5.5.4 Step 3- Design of the Discrete-time RSP Voltage Controller

In a single-phase inverter, the load voltage is required to follow 60 Hz sinusoidal reference ($V_{rms} = 120 \text{ V}$, $V_{peak} = 120 \cdot \sqrt{2} \text{ V}$) in the presence of disturbances, which are currents drawn by the loads. Loads could be linear or nonlinear, and hence, can draw sinusoidal, as well as non-sinusoidal currents. Non-sinusoidal currents contain harmonic frequencies other than the fundamental frequency ($f_1 = 60 \text{ Hz}$). Moreover, the switching action of the inverter can introduce high-frequency components into the system. The low-pass L-C filter, as shown in Figure 5.1, is used to suppress these high frequency harmonics arising from the switching action. However, low frequency harmonic components (3^{rd} , 5^{th} , 7^{th} ...etc. multiple of fundamental frequency) can be present in the inverter output, which can affect the overall system performance, by producing harmonic currents [12]-[13].

It is to be noted that the even frequency harmonic components (2^{nd} , 4^{th} , 6^{th} , 8^{th} ...etc. multiple of fundamental frequency) are absent in the single-phase inverter system. Out of the low frequency harmonic components (3^{rd} , 5^{th} , 7^{th} ...etc. multiple of fundamental frequency), which can be present in the single-phase inverter system, specifically, an elimination or a minimization of 3^{rd} harmonic frequency component from the system output is more important, as it produces higher harmonic currents, compared

to those produced by other harmonic frequency components (5th, 7th ...etc multiple of fundamental frequency) [12]-[13].

5.5.5 Necessary Conditions for the Existence of a Solution of the Robust Servomechanism Problem

A solution to the robust servomechanism problem, defined by equation (5.14), exists if and only if following conditions are satisfied [13], [40]-[43]:

(Condition 1): A system [equation (5.14)] is stabilizable (controllable) and detectable (observable).

A system described by equation (5.14) is said to be controllable, if and only if, its controllability matrix (co) has a full rank = 3.

i.e. $rank(co) = 3$

$$co = [B_d \quad A_d B_d \quad A_d^2 B_d \quad \dots \quad A_d^{n-1} B_d] \quad (5.15)$$

Similarly, a system described by equation (5.14) is said to be observable, if and only if, its observability matrix (ob) has a full rank = 3.

i.e. $rank(ob) = 3$,

$$\text{where, } ob = [C_d \quad C_d A_d \quad C_d A_d^2 \quad \dots \quad C_d A_d^{n-1}]^T \quad (5.16)$$

(Condition 2): The dimension of the control must be greater than or equal to the dimension of the output. i.e. $m \geq r$. For the single-phase inverter, output is the load voltage, and input is the PWM voltage signal. Hence, the dimensions of the output and input are same.

(Condition 3): The transmission zeros of the system must exclude poles of the reference input signals and disturbance signals of the system. As the RSP voltage

controller is designed to eliminate only 3rd harmonic frequency, this condition can be satisfactorily met.

(Condition 4): The system outputs must be physically measurable. In practice, the output voltage and current of the single-phase inverter, can be easily measured.

5.6 Internal Model Principle

The problem of tracking the fundamental frequency ($f_1 = 60 \text{ Hz}$) in the output voltage of the single-phase inverter, is known as the output regulation problem or the servomechanism problem [40]-[43].

When the reference fundamental frequency is to be tracked in the presence of other harmonic frequency ($f_3 = 3 * f_1 \text{ Hz} = 180 \text{ Hz}$), which needs to be rejected, the problem is known as the robust servomechanism problem [40]-[43]. In order to address this problem, for the system given by equation (5.14), a feedback controller needs to be designed which can achieve:

- i) Asymptotic tracking of the reference fundamental frequency $f_1 = 60 \text{ Hz}$
- ii) Rejection or elimination of 3rd harmonic frequency $f_3 = 3 * f_1 \text{ Hz} = 180 \text{ Hz}$ (disturbance rejection) from the output voltage

Importantly, asymptotic tracking of the reference fundamental frequency and elimination of 3rd harmonic frequency from the system output voltage, should happen maintaining the closed-loop stability of the system. The solution to this problem exists, and known as the robust servomechanism problem (RSP) controller, which is based on the internal model principle and linear optimal control theory [40]-[43].

The internal model principle states that, a regulator or a controller is structurally stable, only if the controller utilizes feedback of the regulated variable, and incorporates in the feedback loop, a suitably reduplicated model of the dynamic structure of the exogenous signals, which the regulator is required to process [40]-[43]. I.e. the structurally-stable robust controller can be designed to solve the robust servomechanism problem, only if the dynamics of the reference and disturbance inputs are incorporated in the controller [40]-[43].

For the single-phase inverter, this means that to design the RSP voltage controller, to control the output voltage of the inverter, the fundamental frequency to be tracked ($\omega_1 = 2.\pi.f_1 \text{ rad / s}$) and the third harmonic frequency ($\omega_3 = 2.\pi.f_3 \text{ rad / s}$), which is to be rejected should be included in the controller structure. The linear optimal control theory is used to obtain the feedback gain, which satisfies well-defined performance criterion [12]. The detailed design steps of the RSP voltage controller are given below:

5.7 Design Steps for the RSP Voltage Controller

The RSP voltage controller consists of two parts: a) servocompensator b) stabilizing compensator [40] -[43]. Once, all the conditions for the existence of a solution of the robust servomechanism problem are satisfied, the RSP voltage controller is said to exist, for the system described by equation (5.14). The structure of the discrete-time RSP voltage controller is given as [12] -[13], [40] –[43]:

$$u(k) = K_1.\eta(k) + K_0.x_p(k) \quad (5.17)$$

Where, η is the output of the servocompensator, x_p are the system states, and K_1 and K_0 are the gains of the servocompensator and stabilizing compensators, to be determined.

The design is performed in the following steps:

Step 1: Design the servo compensator for the system given by equation (5.14).

Step 2: Obtain the augmented system, by applying the servocompensator [designed in Step 1] to the system given by equation (5.14).

Step 3: Design the stabilizing compensator for the augmented system [formulated in Step 2], such that the augmented system has the closed-loop stability.

5.7.1 Step 1: The Servocompensator Design

The servocompensator is a feedback compensator, with a voltage error as its input [12] -[13]. In the continuous-time domain, equation of servocompensator is given as:

$$\dot{\eta} = A_{con} \cdot \eta + B_{con} \cdot e_V \quad (5.18)$$

Where, $e_V = V_{ref} - V_{Load}$ is the voltage error.

The dynamics of the servocompensator, given by equation (5.18), depends on the reference input to be tracked and the disturbance input to be minimized or eliminated. Hence, a formulation of the matrix A_{con} , in equation (5.18), depends on the reference and disturbance input in the system [12].

Therefore, a matrix A_{con} must include the reference fundamental frequency ($\omega_1 = 2\pi \cdot f_1 \text{ rad/s}$), and the harmonic frequency ($\omega_3 = 2\pi \cdot f_3 \text{ rad/s}$). A formulation of A_{con} is done by creating the block matrices A_{con1} and A_{con3} as follows:

$$A_{con} = \begin{bmatrix} A_{con1} & \\ & A_{con3} \end{bmatrix}$$

Where, $A_{con1} = \begin{bmatrix} 0 & 1 \\ -(\omega_1)^2 & 0 \end{bmatrix}$ and $\omega_1 = 2\pi \cdot f_1 \text{ rad/s}$, $f_1 = 60 \text{ Hz}$

$$A_{con3} = \begin{bmatrix} 0 & 1 \\ -(\omega_3)^2 & 0 \end{bmatrix} \text{ and } \omega_3 = 2\pi.f_3 \text{ rad/s}, f_3 = 3 * f_1 \text{ Hz} = 180 \text{ Hz}$$

The matrix B_{con} is given as,

$$B_{con} = \begin{bmatrix} B_{con1} \\ B_{con3} \end{bmatrix}$$

$$\text{Where, } B_{con1} = \begin{bmatrix} 0 \\ 1 \end{bmatrix}, B_{con3} = \begin{bmatrix} 0 \\ 1 \end{bmatrix}$$

The servocompensator in the discrete-time domain can be given as:

$$\eta(k+1) = A_{con_d}.\eta(k) + B_{con_d}.e_v(k) \quad (5.19)$$

$$\text{Where, } A_{con_d} = e^{A_{con}.T_s}, B_{con_d} = \int_0^{T_s} e^{A_{con}.(T_s-\tau)}.B_{con}.d\tau$$

5.7.2 Step 2: Determination of the Augmented System

To design the stabilizing compensator, it is necessary to obtain the augmented system, by applying the servocompensator (designed in Step 1) to the system, given by equation (5.14).

The augmented system is obtained as follows:

$$\text{We have from equation (5.14): } x_p(k+1) = A_d.x_p(k) + B_d.u_1(k)$$

$$\text{From equation (5.19), we have: } \eta(k+1) = A_{con_d}.\eta(k) + B_{con_d}.e_v(k)$$

Substituting the voltage error, $e_v = V_{ref} - V_{Load}$, in equation (5.19), we get,

$$\therefore \eta(k+1) = A_{con_d}.\eta(k) + (B_{con_d}).V_{ref} - (B_{con_d}.C_d).x_p(k) - (B_{con_d}.D_d).u(k) \quad (5.20)$$

We can write equations (5.14) and (5.19) in the matrix form as:

$$\begin{bmatrix} x_p(k+1) \\ \eta(k+1) \end{bmatrix} = \begin{bmatrix} A_d & 0 \\ -B_{con_d}.C_d & A_{con_d} \end{bmatrix} \begin{bmatrix} x_p \\ \eta \end{bmatrix} + \begin{bmatrix} B_d \\ -B_{con_d}.D_d \end{bmatrix} .u + [B_{con_d}]V_{ref} \quad (5.21)$$

5.7.3 Step 3: Design of the Stabilizing Compensator

A linear optimal control theory is applied to design the stabilizing compensator. The augmented system, given by equation (5.21), is said to be stable, if the augmented closed-loop system obtained with $V_{ref} \equiv 0$ is stable [40]-[43]. Hence, to design the optimal stabilizing compensator, $V_{ref} \equiv 0$. The equation (5.21) then becomes,

$$\begin{bmatrix} x_p(k+1) \\ \eta(k+1) \end{bmatrix} = \begin{bmatrix} A_d & 0 \\ -B_{con_d}.C_d & A_{con_d} \end{bmatrix} \begin{bmatrix} x_p \\ \eta \end{bmatrix} + \begin{bmatrix} B_d \\ -B_{con_d}.D_d \end{bmatrix} u$$

$$\text{Let } A_{d_aug} = \begin{bmatrix} A_d & 0 \\ -B_{con_d}.C_d & A_{con_d} \end{bmatrix}, \quad B_{d_aug} = \begin{bmatrix} B_d \\ -B_{con_d}.D_d \end{bmatrix}, \quad x_{d_aug} = \begin{bmatrix} x_p \\ \eta \end{bmatrix}$$

$$\Rightarrow x_{d_aug}(k+1) = A_{d_aug}.x_{d_aug}(k) + B_{d_aug}.u(k) \quad (5.22)$$

To find the optimal solution (using linear optimal control theory) for the augmented system, given by equation (5.22), we define the discrete-time linear quadratic performance index as follows [12] -[13]:

$$J_\varepsilon = \sum_{k=0}^{\infty} x_{d_aug}(k)^T .Q. x_{d_aug}(k) + \varepsilon u(k)^T .u(k) \quad (5.23)$$

Where, Q is the symmetrical positive definite matrix, and $\varepsilon > 0$ is a small number needed to reduce the weight of the control force in the optimization [12]-[13]. The value epsilon selected is $\varepsilon = 10^{-5}$. The control performance of the single-phase inverter is dominated by the selection of the weight matrix Q .

In the proposed control design, three different gains w_p , w_1 , w_h are used as the weights for the plant states. The weight matrix Q is selected as follows [12]-[13]:

$$Q = \begin{bmatrix} Q_1 & 0_{2 \times 2} \\ 0_{2 \times 2} & Q_2 \end{bmatrix}, \quad \text{Where, } Q_1 = w_p \cdot \begin{bmatrix} 1 & 0 \\ 0 & 1 \end{bmatrix} \text{ and } Q_2 = \begin{bmatrix} w_1 & 0 \\ 0 & w_h \end{bmatrix} \quad (5.24)$$

For the best control performance, the weight factors are selected as follows: w_p is selected to be significantly smaller than w_1 and w_h . To ensure excellent tracking of the fundamental frequency, w_1 is set significantly greater than w_h [12]-[13].

The values of the weight factors are: $w_p = 0.005$, $w_1 = 5.10^4$, $w_h = 5$

The optimal control, which minimizes the discrete-time linear quadratic performance index, defined in equation (5.23), is given by [12]-[13]:

$$u(k) = K.x_{d_aug}(k) = [K_0 \quad K_1] \begin{bmatrix} x_p(k) \\ \eta(k) \end{bmatrix} = K_0.x_p(k) + K_1.\eta(k) \quad (5.25)$$

Now, to obtain the optimal gain matrix $K = [K_0 \quad K_1]$, by minimizing the discrete-time linear quadratic performance index, requires solving of the discrete-time algebraic Riccati equation [12]-[13], [40]-[43]:

$$[(A_{d_aug})^T.(P)] + [(P).(A_{d_aug})] + (Q) - \left[\left(\frac{1}{\varepsilon}\right).(P).(B_{d_aug}).(B_{d_aug})^T.(P)\right] = 0 \quad (5.26)$$

for the unique positive definite solution P , such that

$$K = -\left(\frac{1}{\varepsilon}\right).(B_{d_aug})^T.(P) \quad (5.27)$$

The discrete-time algebraic Riccati equation, given by (5.26), is solved in MATLAB by command `dlqr()`.

The values of servocompensator gain K_1 and the stabilizing compensator gain K_0 obtained are: $K_1 = [-0.78 \quad -0.68 \quad 1.58 \quad -67555.23]$, $K_0 = [988.95 \quad 3343.76 \quad 3.39]$

The block diagram of the discrete-time RSP voltage controller, with the servo compensator gain, and the stabilizing compensator gain is shown in Figure 5.6 [12].

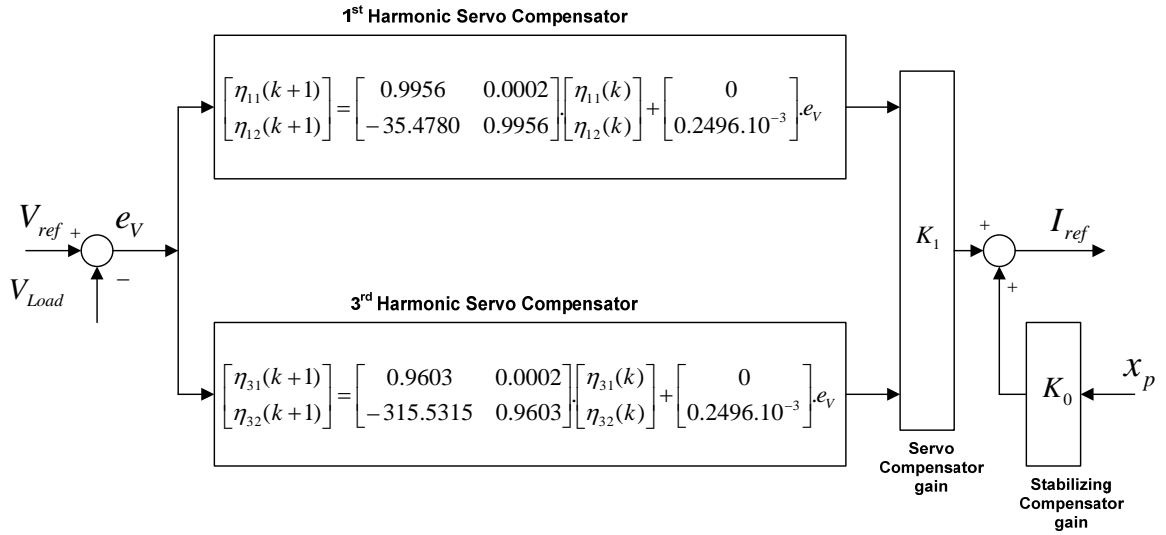


Figure 5.6 Block Diagram of the Discrete-time RSP Voltage Controller

5.8 Model of a Three-Phase Inverter

The schematic diagram of a three-phase inverter is shown in Figure 5.7 [12]-[13]. The system consists of a three-phase PWM inverter, an output L-C filter, and the transformer. The transformer is delta-wye connected, which provides isolation between the load side and the inverter side. The secondary side of the transformer, which is connected to the loads, is grounded. To develop the state space model of the three-phase inverter, shown in Figure 5.7, a model of the delta-wye transformer is required. Therefore, the transformer is modeled as an ideal transformer, with leakage inductance L_T and series resistance R_T , on the secondary side of the transformer. The model of the delta-wye transformer is shown in Figure 5.8 [12].

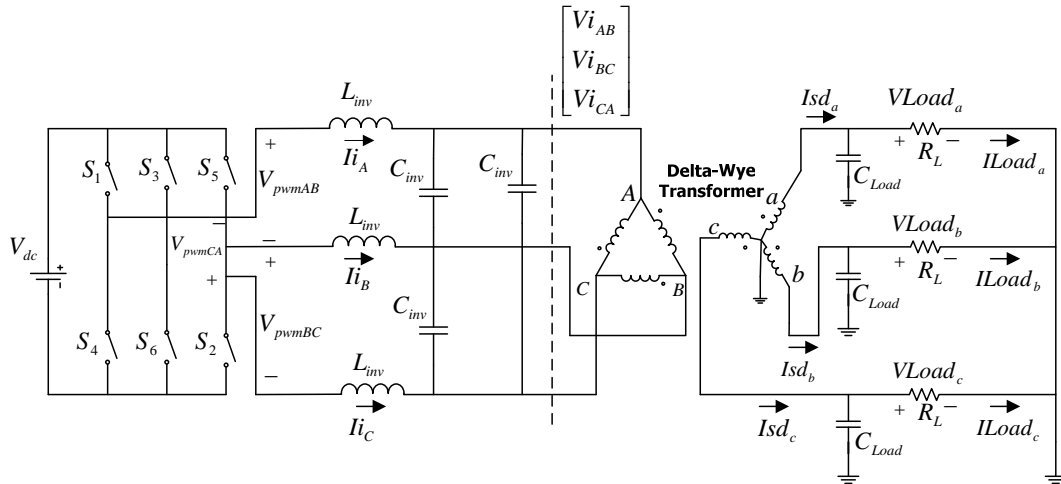


Figure 5.7 Three-Phase Inverter with a Low-pass L-C Filter and a Transformer

$L_{inv} = 10.2 \text{ mH}$	$V_{dc} = 480 \text{ V}$
$C_{inv} = 55 \text{ }\mu\text{F}$	Output Voltage: $V_{Load} = 208 \text{ V}_{L-L}, 120 \text{ V}_{L-N}$
$C_{Load} = 5 \text{ }\mu\text{F}$	PWM switching frequency = 5.4 kHz
$R_T = 0.001 \text{ pu}$	Fundamental frequency: $f_1 = 60 \text{ Hz}$
$L_T = 0.003 \text{ pu}$	

Table 5.2 Parameters of Three-Phase Inverter System

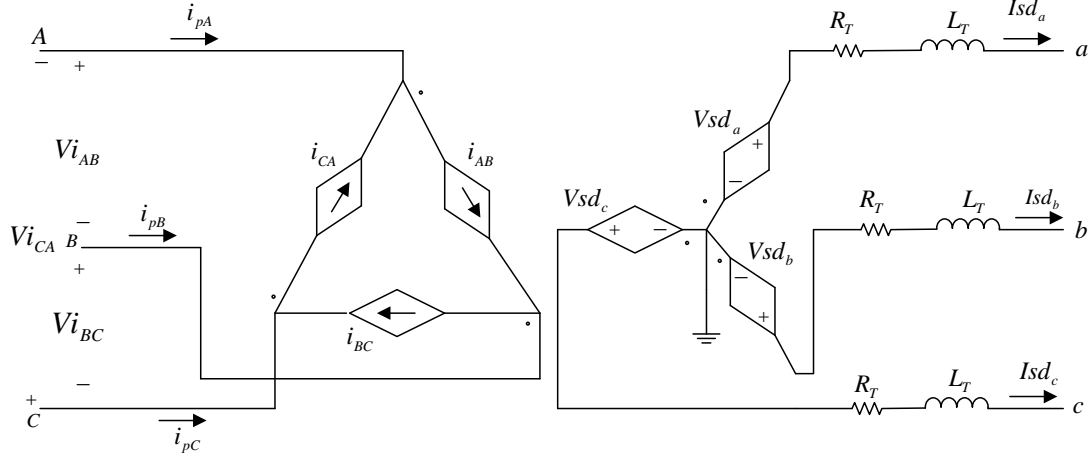


Figure 5.8 A Delta-Wye Transformer Model

From Figures 5.7 and 5.8, state space equations for the three-phase inverter, in abc reference frame, can be given as [12]-[13]:

$$\begin{aligned} \frac{d\vec{V}i_{ABC}}{dt} &= \left(\frac{1}{3.C_{inv}} \right) \vec{I}i_{ABC} - \left(\frac{1}{3.C_{inv}} \right) Tr_i \cdot \vec{I}sd_{abc} \\ \frac{d\vec{I}i_{ABC}}{dt} &= \left(\frac{1}{L_{inv}} \right) \vec{V}pwm_{ABC} - \left(\frac{1}{L_{inv}} \right) \vec{V}i_{ABC} \\ \frac{d\vec{V}Load_{abc}}{dt} &= \left(\frac{1}{C_{Load}} \right) \vec{I}sd_{abc} - \left(\frac{1}{C_{Load}} \right) \vec{I}Load_{abc} \\ \frac{d\vec{I}sd_{abc}}{dt} &= \left(\frac{-R_T}{L_T} \right) \vec{I}sd_{abc} + \left(\frac{1}{L_T} \right) Tr_v \cdot \vec{V}i_{ABC} - \left(\frac{1}{L_{inv}} \right) \vec{V}Load_{abc} \end{aligned} \quad (5.28)$$

Where, $\vec{V}i_{ABC}$, $\vec{I}i_{ABC}$, $\vec{V}Load_{abc}$, $\vec{I}sd_{abc}$, are the state variables of the three-phase inverter, $\vec{V}pwm_{ABC}$ is the control input, and $\vec{I}load_{abc}$ is the disturbance, which is the load current

$$Tr_i = tr. \begin{bmatrix} 1 & -2 & 1 \\ 1 & 1 & -2 \\ -2 & 1 & 1 \end{bmatrix}, \quad Tr_v = tr. \begin{bmatrix} 0 & 0 & -1 \\ -1 & 0 & 0 \\ 0 & -1 & 0 \end{bmatrix} \text{ are the current and voltage transformation}$$

matrices of the transformer, and $tr = \frac{N_s}{N_p}$ is the transformer's turns ratio [12].

These dynamic equations can be transformed into dq -axis stationary reference frame using the following voltage and current transformations [12] -[13]:

$$\vec{V}_{qd0} = K_s \cdot \vec{V}_{abc} \quad \text{and} \quad \vec{I}_{qd0} = K_s \cdot \vec{I}_{abc} \quad (5.29)$$

Where, \vec{V}_{abc} and \vec{I}_{abc} are the voltages and currents of three-phase inverter system in abc reference frame, while, \vec{V}_{qd0} and \vec{I}_{qd0} are the voltages and currents of three-phase inverter system in dq -axis reference frame, respectively. The transformation matrix K_s is given as [12]:

$$K_s = \frac{2}{3} \begin{bmatrix} 1 & -1/2 & -1/2 \\ 0 & -\sqrt{3}/2 & \sqrt{3}/2 \\ 1/2 & 1/2 & 1/2 \end{bmatrix}$$

The state space equations of the three-phase inverter system, in dq -axis reference frame, can be given as [12]-[13]:

$$\frac{d\vec{V}_{i_{qd}}}{dt} = \frac{1}{3C_{inv}} \vec{I}_{i_{qd}} - \frac{1}{3C_{inv}} Tr_{i_{qd}} \vec{I}_{sd_{qd0}}$$

$$\frac{d\vec{I}_{i_{qd}}}{dt} = \frac{1}{L_{inv}} \vec{V}_{pwm_{qd}} - \frac{1}{L_{inv}} \vec{V}_{i_{qd}}$$

$$\frac{d\vec{V}_{Load_{qd0}}}{dt} = \frac{1}{C_{Load}} \vec{I}_{sd_{qd0}} - \frac{1}{C_{Load}} \vec{I}_{Load_{qd0}}$$

$$\frac{\bar{I}sd_{qd0}}{dt} = \frac{-R_T}{L_T} \bar{I}sd_{qd0} + \frac{1}{L_T} Trv_{qd} \bar{V}i_{qd} - \frac{1}{L_T} \bar{V}Load_{qd0} \quad (5.30)$$

Where,

$$Tri_{qd} = [K_S \cdot Tr_i \cdot K_S^{-1}]_{(row1:2),(col1:2)} = \frac{3}{2} \cdot tr \cdot \begin{bmatrix} 1 & \sqrt{3} \\ -\sqrt{3} & 1 \end{bmatrix} \quad (5.31)$$

$$Trv_{qd} = [K_S \cdot Tr_v \cdot K_S^{-1}]_{(row1:2),(col1:2)} = \frac{1}{2} \cdot tr \cdot \begin{bmatrix} 1 & -\sqrt{3} \\ \sqrt{3} & 1 \end{bmatrix} \quad (5.32)$$

Therefore, the continuous-time state space model of three-phase inverter, in dq-axis reference frame, is given as:

$$\begin{aligned} \dot{\bar{x}}_{3p} &= A_{3p} \cdot \bar{x}_{3p} + B_{3p} \cdot \bar{u} \\ \bar{y} &= C_{3p} \cdot \bar{x}_{3p} + D_{3p} \cdot \bar{u} \end{aligned} \quad (5.33)$$

Where,

$$A_{3p} = \begin{bmatrix} \mathbf{0}_{2 \times 2} & \left(\frac{1}{3} C_{inv}\right) \cdot I_{2 \times 2} & \mathbf{0}_{2 \times 2} & \left(-\frac{1}{3} C_{inv}\right) \cdot Tri_{qd} \\ \left(-\frac{1}{L_{inv}}\right) \cdot I_{2 \times 2} & \mathbf{0}_{2 \times 2} & \mathbf{0}_{2 \times 2} & \mathbf{0}_{2 \times 2} \\ \mathbf{0}_{2 \times 2} & \mathbf{0}_{2 \times 2} & \mathbf{0}_{2 \times 2} & \left(\frac{1}{C_{Load}}\right) \cdot I_{2 \times 2} \\ \left(\frac{1}{L_T}\right) \cdot Trv_{qd} & \mathbf{0}_{2 \times 2} & \left(-\frac{1}{L_T}\right) \cdot I_{2 \times 2} & \left(-\frac{R_T}{L_T}\right) \cdot I_{2 \times 2} \end{bmatrix},$$

$$B_{3p} = \begin{bmatrix} \mathbf{0}_{2 \times 2} \\ \left(\frac{1}{L_{inv}}\right) \cdot I_{2 \times 2} \\ \mathbf{0}_{2 \times 2} \\ \mathbf{0}_{2 \times 2} \end{bmatrix}, \quad \bar{x}_{3p} = \begin{bmatrix} \bar{V}i_{qd} \\ \bar{I}i_{qd} \\ \bar{V}Load_{qd} \\ \bar{I}sd_{qd} \end{bmatrix} = \begin{bmatrix} V i_q \\ V i_d \\ I i_q \\ I i_d \\ V Load_q \\ V Load_d \\ I sd_q \\ I sd_d \end{bmatrix}, \quad \bar{u} = \bar{V}pwm_{qd} = \begin{bmatrix} Vpwm_q \\ Vpwm_d \end{bmatrix}$$

$$C_{3p} = [\mathbf{0}_{2 \times 2} \quad \mathbf{0}_{2 \times 2} \quad I_{2 \times 2} \quad \mathbf{0}_{2 \times 2}] \quad , \quad D_{3p} = [\mathbf{0}_{2 \times 2}]$$

To discretize the continuous-time model, the sampling time selected is the reciprocal of the PWM switching frequency [12]-[13].

$$\Rightarrow T_s = \frac{1}{\text{PWM Switching frequency}} = \frac{1}{5400} = 1.85 * 10^{-4} \text{ sec}$$

Equation (5.33) can be given in the discrete-time domain as:

$$\begin{aligned} \bar{x}_{3p}(k+1) &= A_{3pd} \cdot \bar{x}_{3p}(k) + B_{3pd} \cdot \bar{u}(k) \\ \bar{y}(k) &= C_{3pd} \cdot \bar{x}_{3p}(k) + D_{3pd} \cdot \bar{u}(k) \end{aligned} \quad (5.34)$$

Where,

$$\begin{aligned} A_{3pd} &= e^{A_{3p} \cdot T_s}, & B_{3pd} &= \int_0^{T_s} e^{A_{3p} \cdot (T_s - \tau)} \cdot B_{3p} \cdot d\tau, & C_{3pd} &= C_{3p}, & D_{3pd} &= D_{3p} \\ \bar{u}(k) &= \bar{V}pwm_{qd} = \begin{bmatrix} Vpwm_q \\ Vpwm_d \end{bmatrix} \end{aligned}$$

5.9 Control Development for the Three-Phase Inverter

The control design procedure explained in Sections 5.2 to 5.7, for the single-phase inverter, is followed for the three-phase inverter, and the following control strategies are designed:

- (i) The discrete-time PID voltage control and discrete-time PID current Control
- (ii) The discrete-time RSP voltage control with discrete-time sliding mode current control

The performance of the three-phase inverter, operating under balanced linear loads, unbalanced linear loads, and nonlinear loads under these control strategies is analyzed.

The control block diagram of the discrete-time PID voltage and discrete-time PID current controller for three-phase inverter, is shown in Figure 5.9. Figures 5.10 and 5.11 show the discrete-time PID voltage and the current control block, respectively.

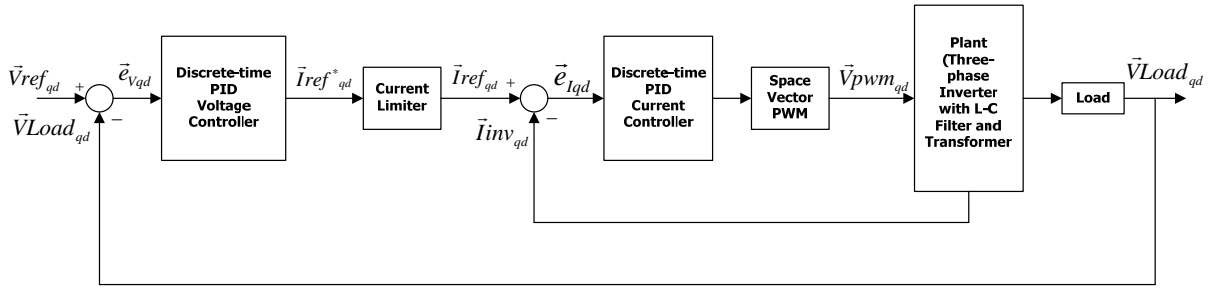


Figure 5.9 Control Block Diagram of the Discrete-time PID Voltage and Current Control for the Three-Phase Inverter

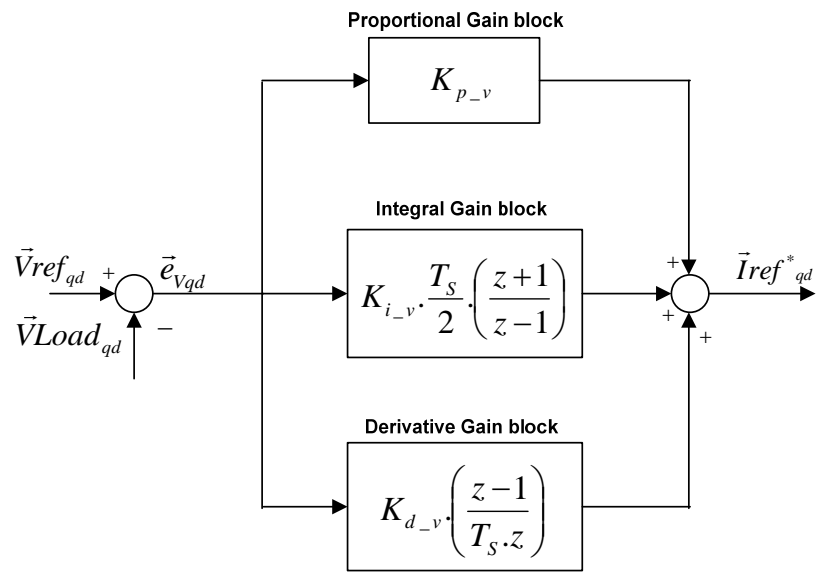


Figure 5.10 Discrete-time PID Voltage Control Block for the Three-Phase Inverter

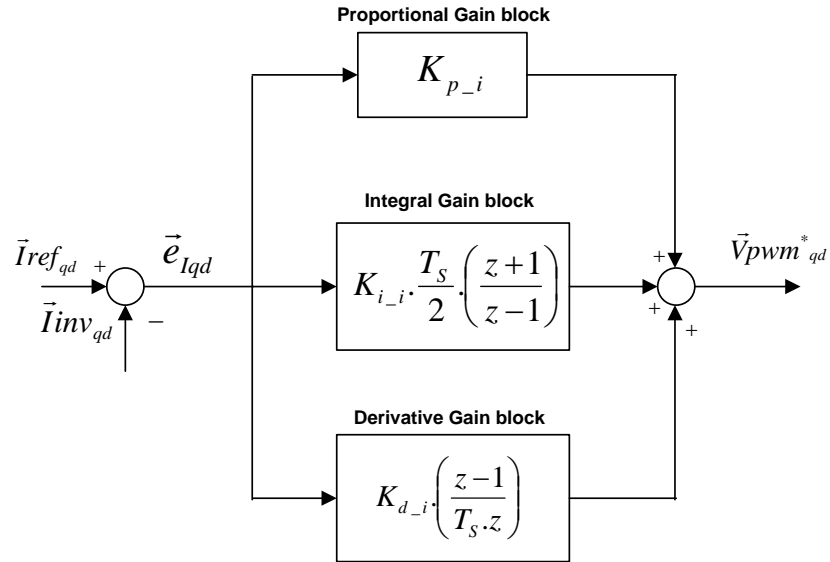


Figure 5.11 Discrete-time PID Current Control Block for the Three-Phase Inverter

The control block diagram of the discrete-time RSP voltage controller and discrete-time sliding mode current controller, for the three-phase inverter, is shown in Figure 5.12. The RSP voltage controller is designed to minimize the presence of 5th and 7th harmonic frequencies from the system output, and the block diagram of the RSP voltage controller is shown in Figure 5.13.

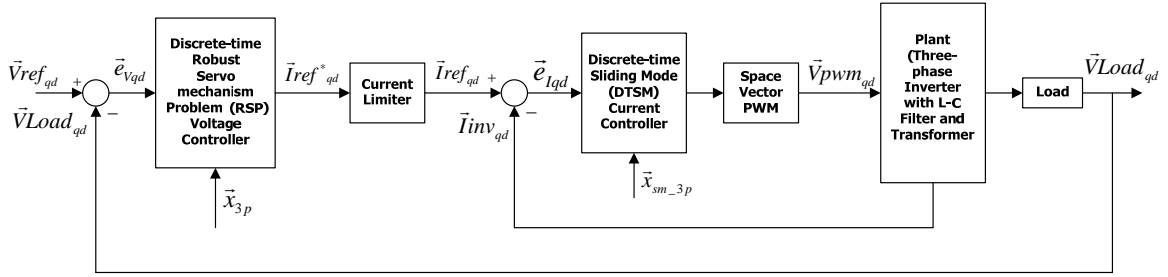


Figure 5.12 Control Block Diagram of the Discrete-time RSP Voltage Control and Discrete-time Sliding Mode Current Control for the Three-Phase Inverter

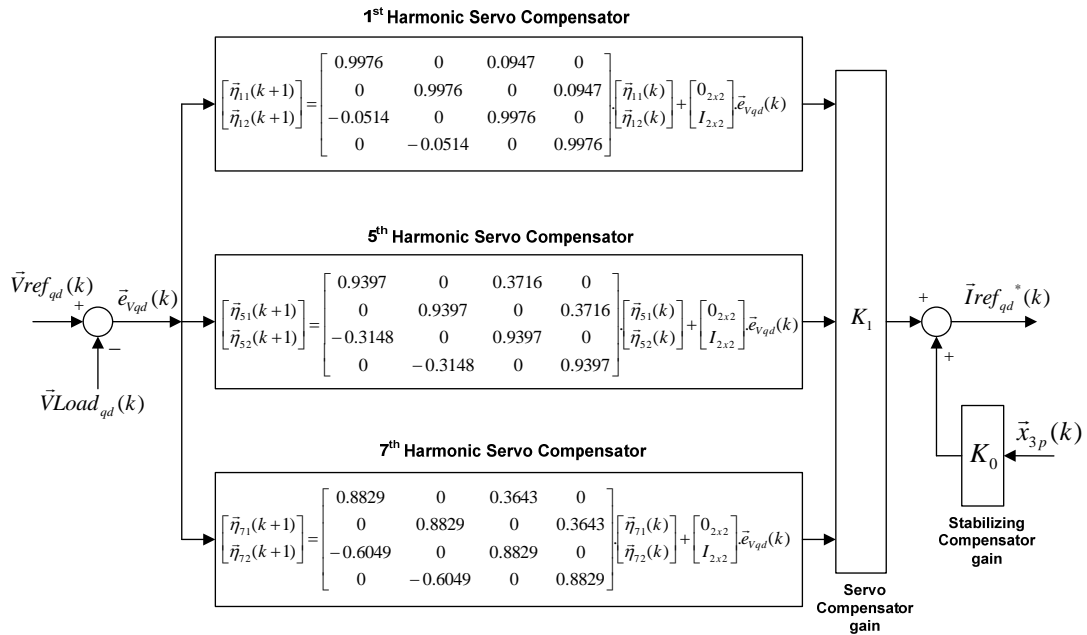


Figure 5.13 Block Diagram of the Discrete-time RSP Voltage Controller for the Three-Phase Inverter

5.10 Simulation Results

The simulation of single-phase inverter, with designed voltage and current control strategies, is performed in MATLAB/Simulink. The single-phase bridge inverter, with four power switches, can be simulated in two ways as follows: The full-bridge inverter available in '*Simpowersystems*' toolbox of MATLAB/Simulink can be directly used in the simulation or the simpler model of the bridge inverter can be derived, where, the full-bridge inverter is simulated as, ' $m_a * V_{dc}$ '. [71] The dynamics of the single-phase full-bridge inverter can be represented in this way because [71]:

- (i) the switching frequency of the inverter (4 kHz) is much higher than the fundamental frequency of the inverter (60 Hz).
- (ii) The output voltage of the single-phase bridge inverter is proportional to the input dc voltage, and duty cycle of the inverter.

Both the approaches are used to perform the simulation.

5.10.1 Simulation Results of Single-Phase Inverter with Discrete-time PID Voltage Controller and Discrete-time PID Current Controller

Type of Load	V _{Load} (rms) (V)	THD (%)
No-load	118.7	0.7268
Linear Load		
R	118.7	0.7268
R-L (pf : 0.7)	118.7	0.7268
Nonlinear Load		
Crest factor (3:1)	114.7	5.149

Table 5.3 Single-Phase Inverter: Results with the Discrete-time PID Voltage and Current Controller

Table 5.3 tabulates the simulation results of the application of the discrete-time PID voltage and current control design to the single-phase inverter operating under linear and nonlinear loads. The output voltage THD is less than 2% for linear loads. However, for nonlinear loads output voltage THD is more than 5%. Thus, it can be concluded that the PID control design works quite well for linear loads, but fails to achieve low THD output under nonlinear loads.

Figures 5.14 to 5.17 show the simulation plots of the application of the PID control design to the single-phase inverter.

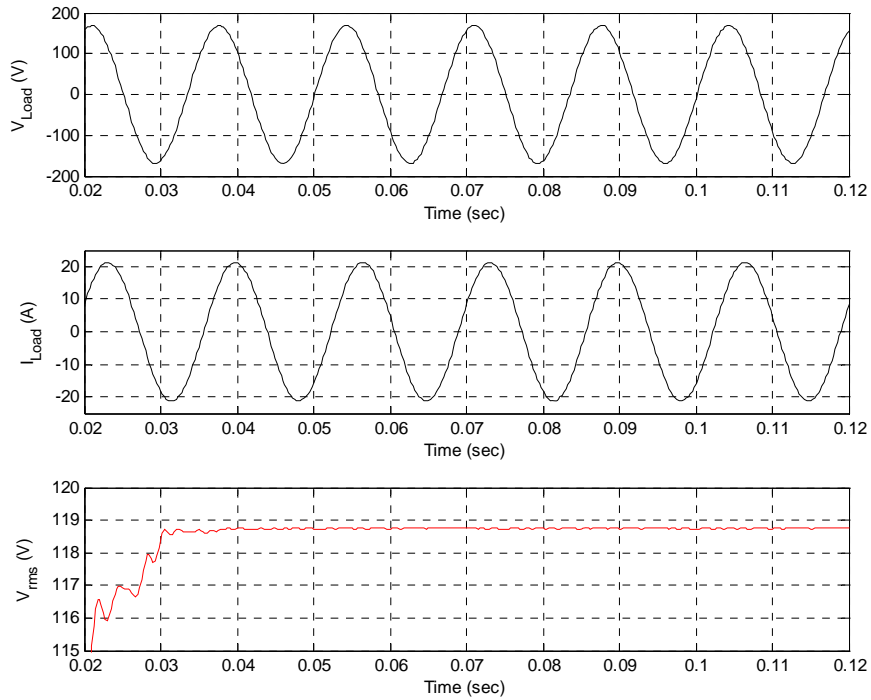


Figure 5.14 Simulation Results of the Single-Phase Inverter under Linear (R-L) Load with Power Factor 0.7 (**Top:** Load Voltage, **Middle:** Load Current, **Bottom:** Load (RMS) Voltage)

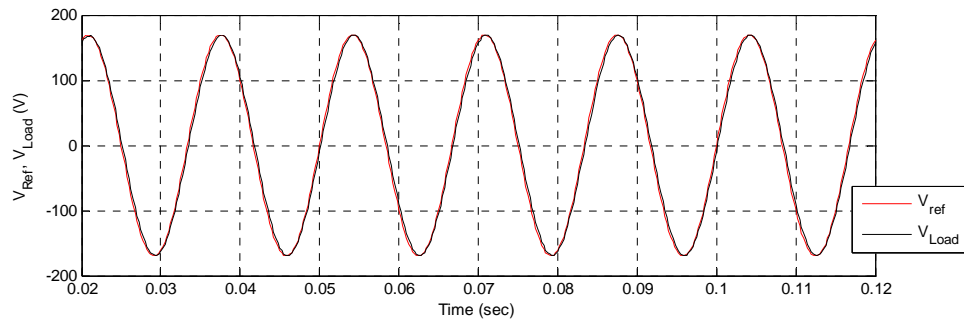


Figure 5.15 Comparison of the Reference Voltage with the Actual Load Voltage of the Single-Phase Inverter under Linear (R-L) Load with Power Factor 0.7

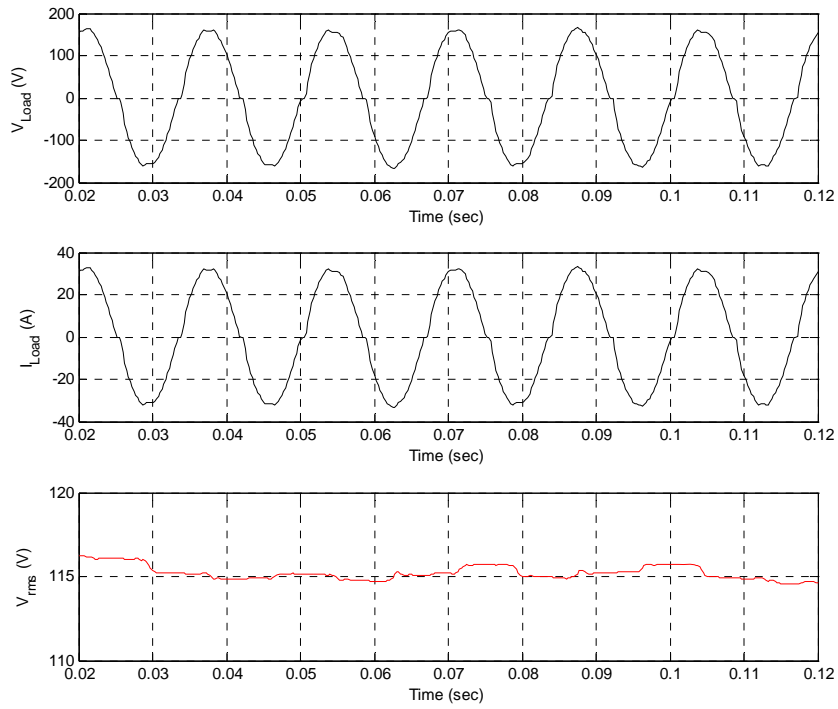


Figure 5.16 Simulation Results of the Single-Phase Inverter under Nonlinear load (**Top:** Load Voltage, **Middle:** Load Current, **Bottom:** Load (RMS) Voltage)

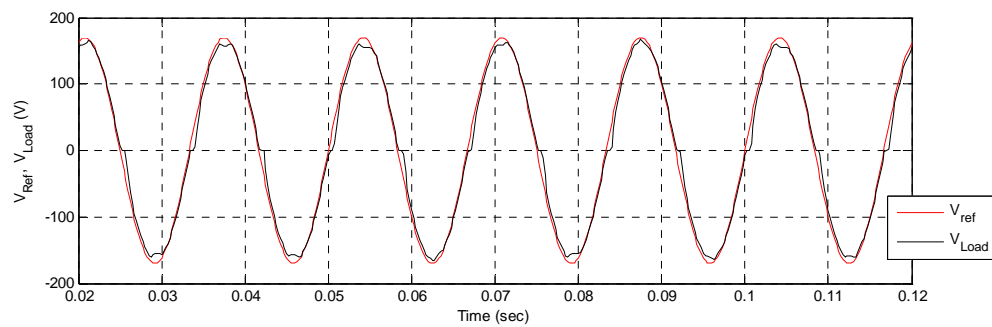


Figure 5.17 Comparison of the Reference Voltage with the Actual Load Voltage of the Single-Phase Inverter under Nonlinear Load

5.10.2 Simulation Results of Single-Phase Inverter with Discrete- time RSP Voltage Controller and Discrete-time Sliding Mode Current Controller

Type of Load	V _{Load} (rms) (V)	THD (%)
No-load	120	0.1087
Linear Load		
R	120	0.1087
R-L (pf : 0.7)	120	0.1087
Nonlinear Load		
Crest factor (3:1)	120	0.1098

Table 5.4 Single-Phase Inverter: Results with the Discrete-time RSP Voltage Controller and Discrete-time Sliding Mode Current Controller

Table 5.4 tabulates the simulation results of the application of the discrete-time RSP voltage control and discrete-time sliding mode current control design, to the single-phase inverter operating under linear and nonlinear loads. The output voltage THD obtained under all loading conditions, is less than 1% . Thus, it can be concluded that the discrete-time RSP voltage control and discrete-time sliding mode current control design, is the effective control strategy for the single-phase inverter, which achieves the low THD voltage output under linear, as well as nonlinear loads.

Figures 5.18 to 5.21 show the simulation plots of the application of this control technique to the single-phase inverter.

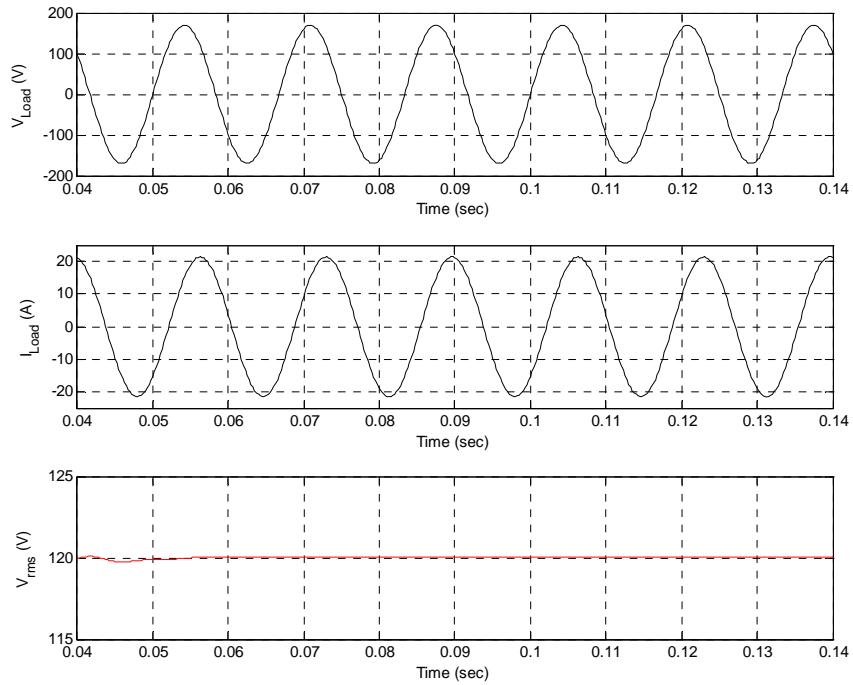


Figure 5.18 Simulation Results of the Single-Phase Inverter under Linear (R-L) Load with Power Factor 0.7 (**Top:** Load Voltage, **Middle:** Load Current, **Bottom:** Load (RMS) Voltage)

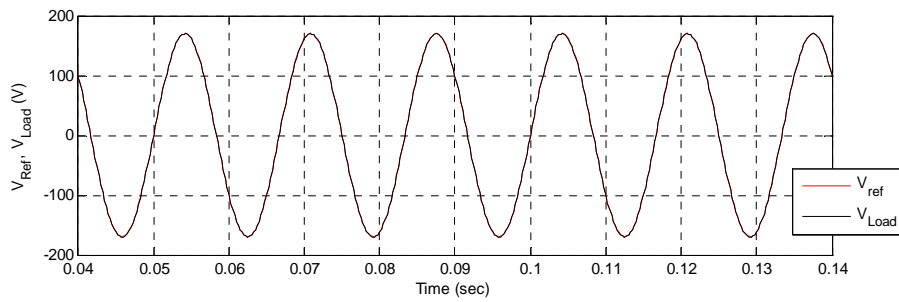


Figure 5.19 Comparison of the Reference Voltage with the Actual Load Voltage of the Single-Phase Inverter under Linear (R-L) Load with Power Factor 0.7

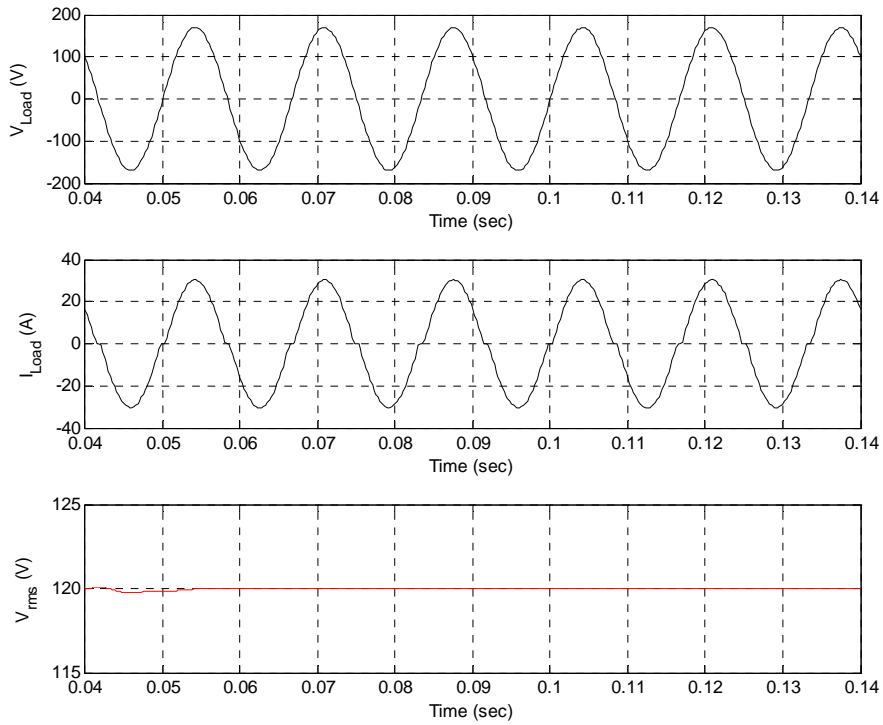


Figure 5.20 Simulation Results of the Single-Phase Inverter under Nonlinear load (**Top:** Load Voltage, **Middle:** Load Current, **Bottom:** Load (RMS) Voltage)

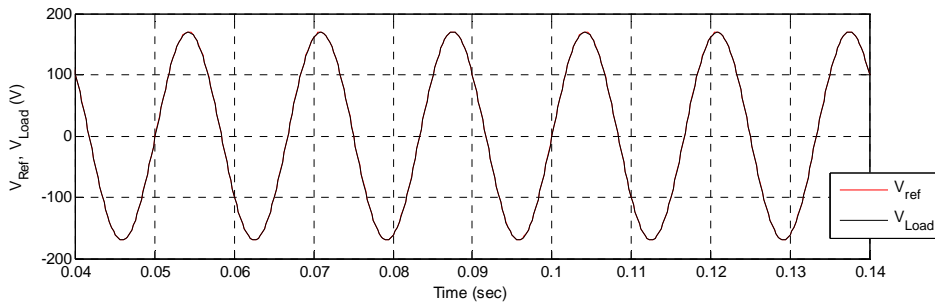


Figure 5.21 Comparison of the Reference Voltage with the Actual Load Voltage of the Single-Phase Inverter under Nonlinear Load

5.10.3 Simulation Results of Three-Phase Inverter with Discrete-time PID Voltage Controller and Discrete-time PID Current Controller

Linear Balanced Load			
Full-Load condition			
V_{PhaseA} (rms) (V)	V_{PhaseB} (rms) (V)	V_{PhaseC} (rms) (V)	THD (%)
119.6	119.6	119.6	0.62%
Linear Unbalanced Load			
Case- I: Phase A: Fully Loaded, Phase B: 75% Loaded, Phase C: 75% Loaded			
V_{PhaseA} (rms) (V)	V_{PhaseB} (rms) (V)	V_{PhaseC} (rms) (V)	THD (%)
105.6	115.5	115.4	22.2%
Case- II: Phase A: 75% Loaded, Phase B: 80% Loaded, Phase C: 90% Loaded			
V_{PhaseA} (rms) (V)	V_{PhaseB} (rms) (V)	V_{PhaseC} (rms) (V)	THD (%)
111.8	122.5	106.5	19.4%
Nonlinear Load: Crest factor (3:1)			
V_{PhaseA} (rms) (V)	V_{PhaseB} (rms) (V)	V_{PhaseC} (rms) (V)	THD (%)
113.1	120	121.7	14.61%

Table 5.5 Three-Phase Inverter: Results with the Discrete-time PID Voltage and Current Controller

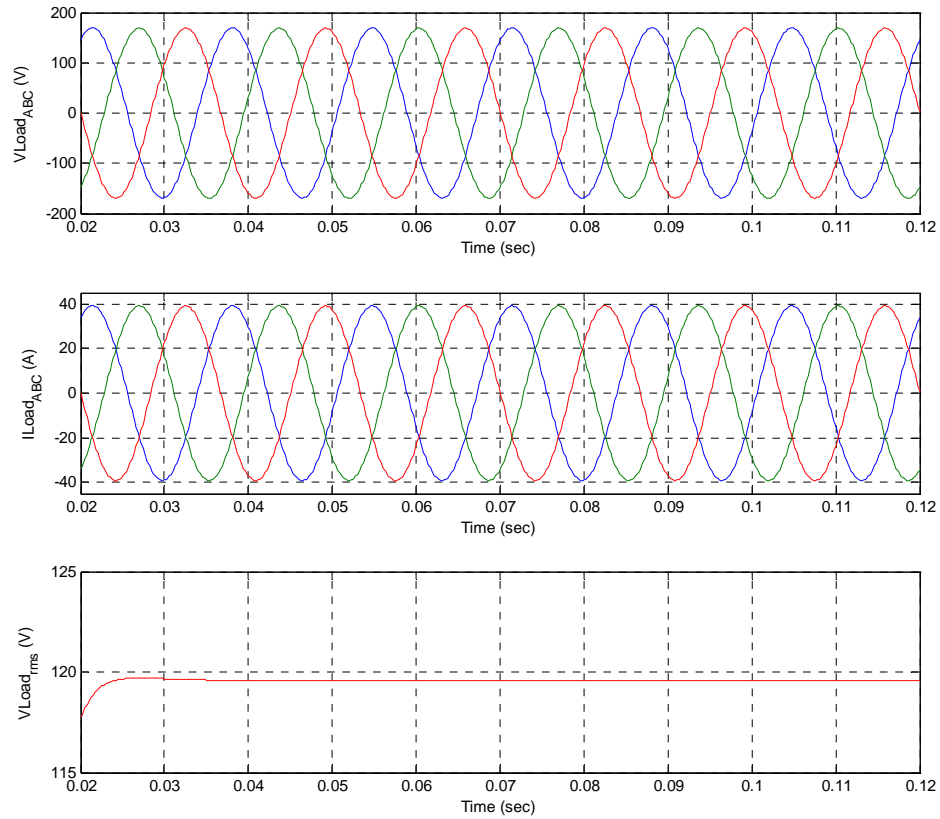


Figure 5.22 Simulation Results of the Three-Phase Inverter under Balanced Linear Load (Top: Load Voltage, Middle: Load Current, Bottom: Load (RMS) Voltage)

It can be seen from Figure 5.22 that the discrete-time voltage and current PID controller work very well for linear balanced loads. The harmonic reduction achieved (output voltage THD = 0.62%) is within the acceptable limit. Also, the RMS value of the load voltage obtained is 119.6 V.

The comparison of the reference voltage with the actual load voltage, in d-q axis reference frame, is shown in Figure 5.23. It can be seen that, under balanced linear load,

the discrete-time voltage and current PID controller provide a satisfactory output voltage regulation.

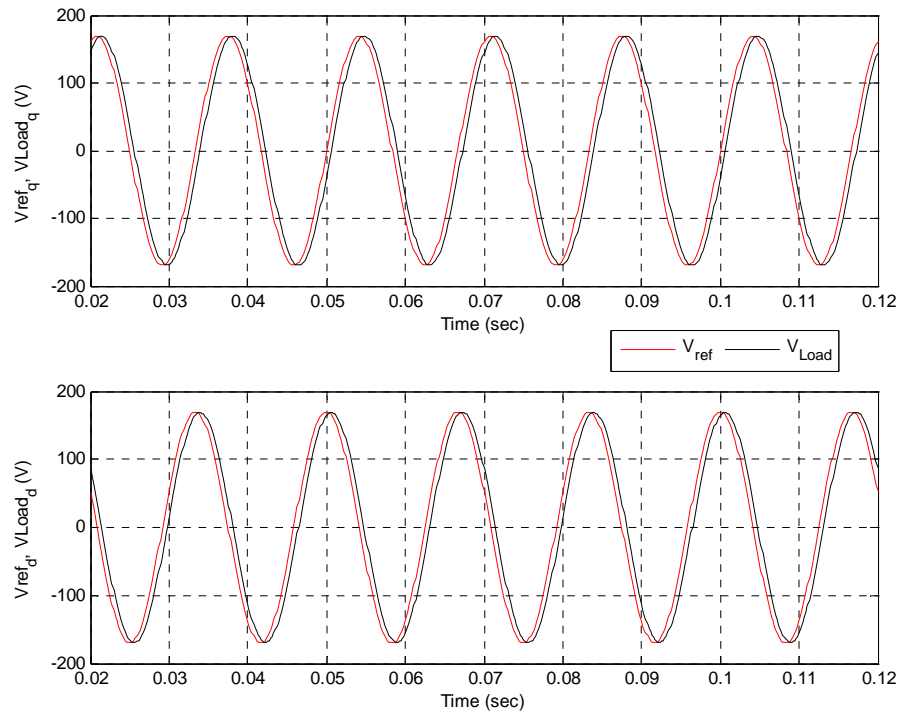


Figure 5.23 Comparison of the Reference Voltage with the Actual Load Voltage of the Three-Phase Inverter (in the d-q axis reference frame) under Balanced Linear Load

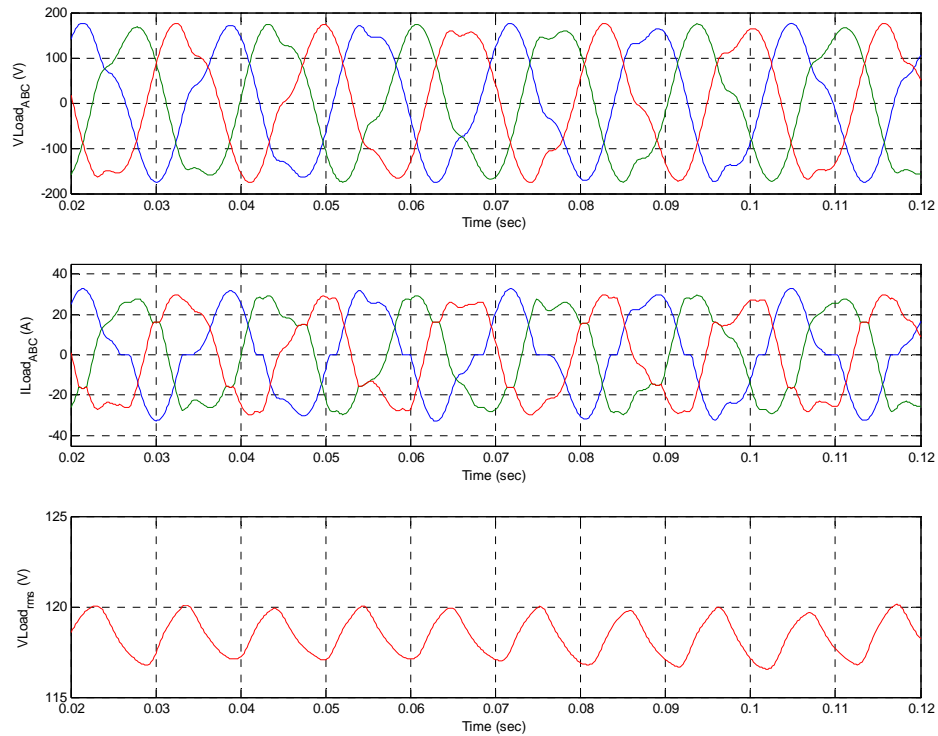


Figure 5.24 Simulation Results of the Three-Phase Inverter under Nonlinear Load
(Top: Load Voltage, Middle: Load Current, Bottom: Load (RMS) Voltage)

It can be seen from Figure 5.24 that three-phase inverter system does not perform satisfactorily with the discrete-time voltage and current PID controller under nonlinear load condition.

It is observed that when the system is simulated with the nonlinear load, the output voltage THD obtained is 14.61 %, which is not within the acceptable limit. Also, the nonsinusoidal current drawn by the load, distorts the output voltage of the system.

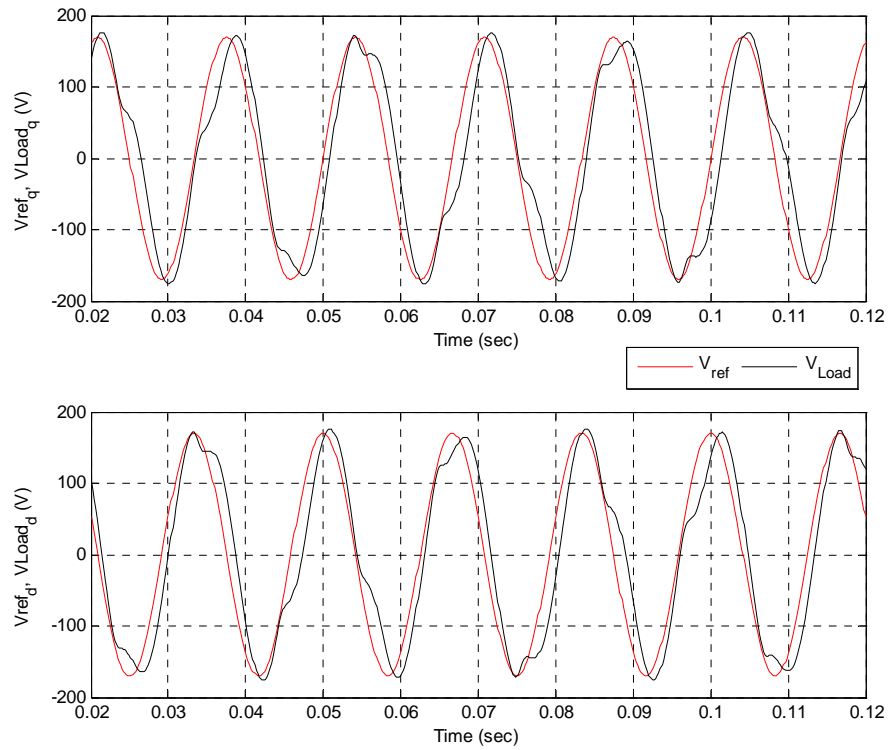


Figure 5.25 Comparison of the Reference Voltage with the Actual Load Voltage of the Three-Phase Inverter (in the d-q axis reference frame) under Nonlinear Load

The comparison of the reference voltage with the actual load voltage, in d-q axis reference frame, is shown in Figure 5.25. It can be seen that, under nonlinear load condition, the discrete-time voltage and current PID controller cannot provide a satisfactory output voltage regulation.

5.10.4 Simulation Results with Discrete-time RSP Voltage Controller and Discrete-time Sliding Mode Current Controller

Linear Balanced Load			
Full-Load condition			
V_{PhaseA} (rms) (V)	V_{PhaseB} (rms) (V)	V_{PhaseC} (rms) (V)	THD (%)
120	120	120	0.37%
Linear Unbalanced Loads			
Case- I: Phase A: Fully Loaded, Phase B: 75% Loaded, Phase C: 75% Loaded			
V_{PhaseA} (rms) (V)	V_{PhaseB} (rms) (V)	V_{PhaseC} (rms) (V)	THD (%)
120.1	120	119.9	0.45%
Case- II: Phase A: 75% Loaded, Phase B: 80% Loaded, Phase C: 90% Loaded			
V_{PhaseA} (rms) (V)	V_{PhaseB} (rms) (V)	V_{PhaseC} (rms) (V)	THD (%)
120	120.1	120	0.38%
Nonlinear Load: Crest factor (3:1)			
V_{PhaseA} (rms) (V)	V_{PhaseB} (rms) (V)	V_{PhaseC} (rms) (V)	THD (%)
120	120	120	0.40%

Table 5.6 Three-Phase Inverter: Results with the Discrete-time RSP Voltage Controller and Discrete-time Sliding Mode Current Controller

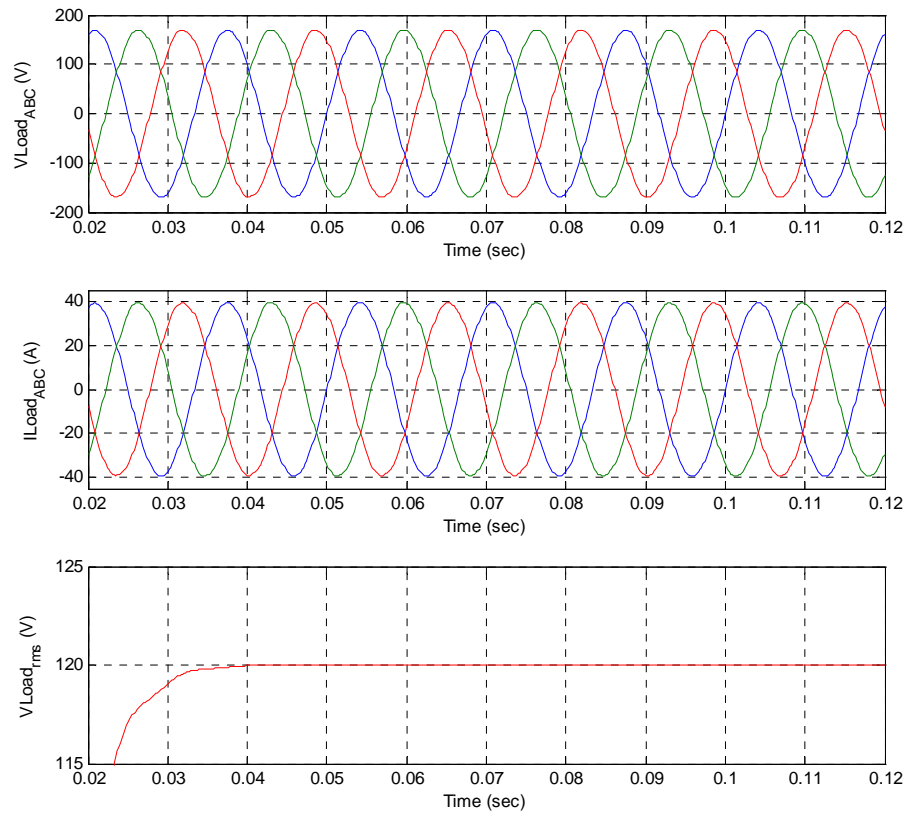


Figure 5.26 Simulation Results of the Three-Phase Inverter under Balanced Linear Load (Top: Load Voltage, Middle: Load Current, Bottom: Load (RMS) Voltage)

Table 5.6 tabulates the simulation results of the application of the discrete-time RSP voltage control and discrete-time sliding mode current control design, to the three-phase inverter. The output voltage THD obtained, under all loading conditions, is less than 1% . Thus, it can be concluded that the discrete-time RSP voltage control and discrete-time sliding mode current control design is an effective control strategy for the three-phase inverter.

Figures 5.26 to 5.33 show the simulation plots of the application of this control technique to the three-phase inverter

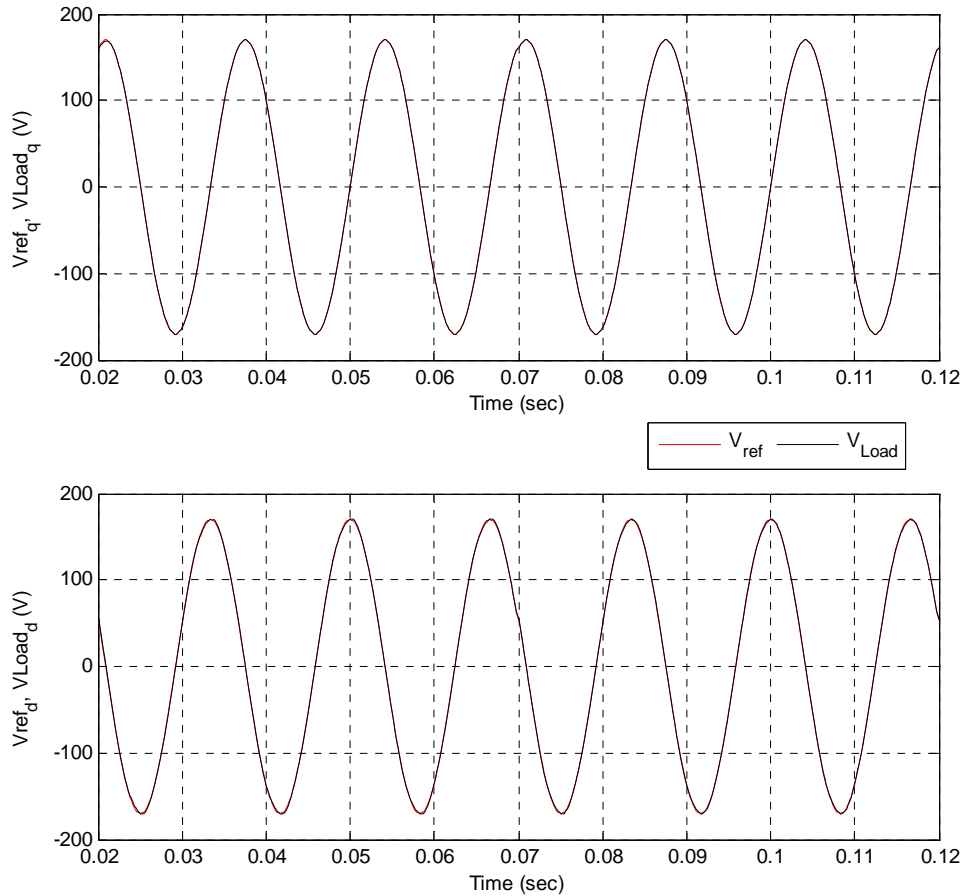


Figure 5.27 Comparison of the Reference Voltage with the Actual Load Voltage of the Three-Phase Inverter (in the d-q axis reference frame) under Balanced Linear Load

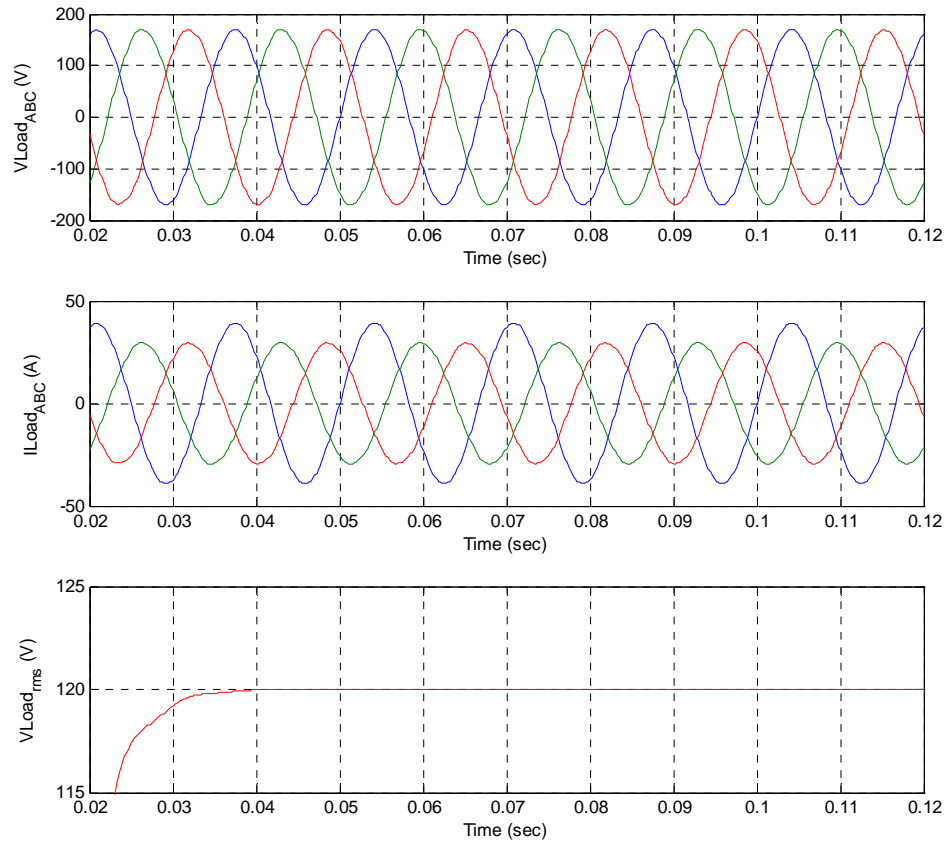


Figure 5.28 Simulation Results of the Three-Phase Inverter under Unbalanced Linear Load **Case I: Phase A: Fully Loaded, Phase B: 75% Loaded, Phase C: 75% Loaded** (**Top: Load Voltage, Middle: Load Current, Bottom: Load (RMS) Voltage**)

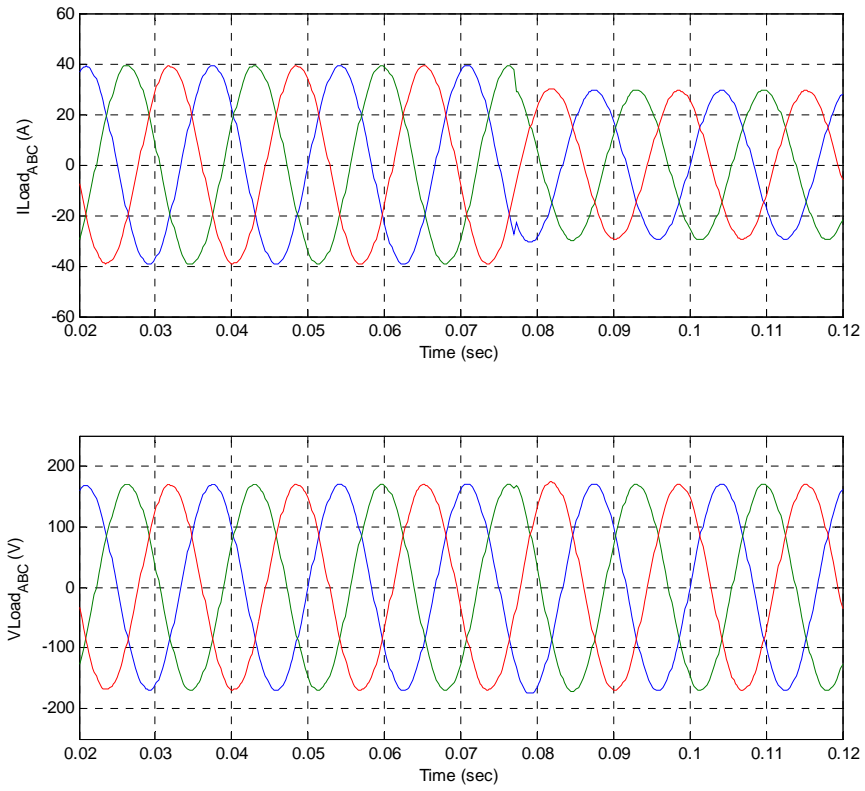


Figure 5.29 Transient Response of the Three-Phase Inverter for 100 % to 75% Load Change (**Top:** Load Current, **Bottom:** Load Voltage)

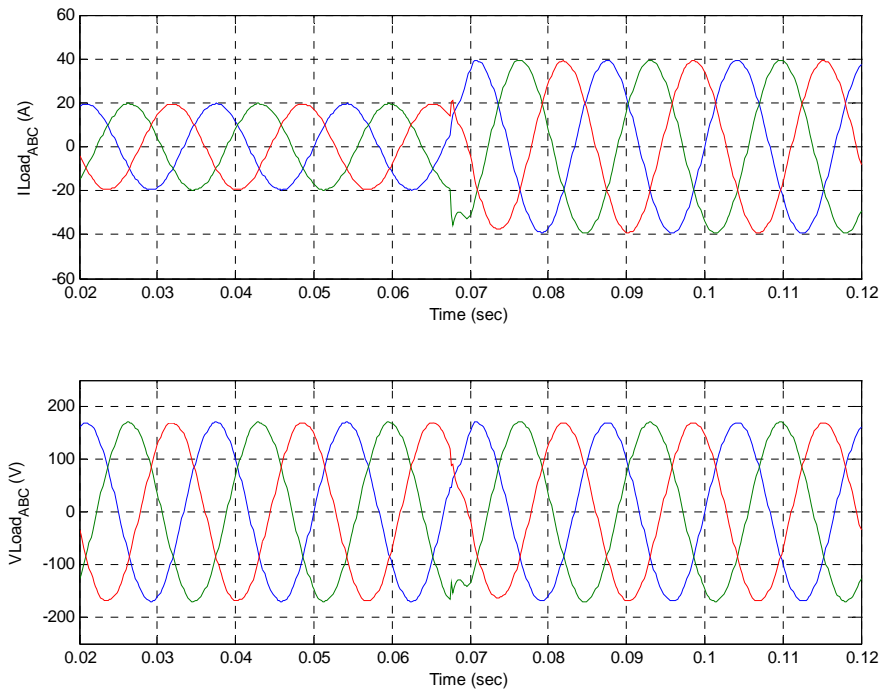


Figure 5.30 Transient Response of the Three-Phase Inverter for 50 % to 100% Load Change (**Top:** Load Current, **Bottom:** Load Voltage)

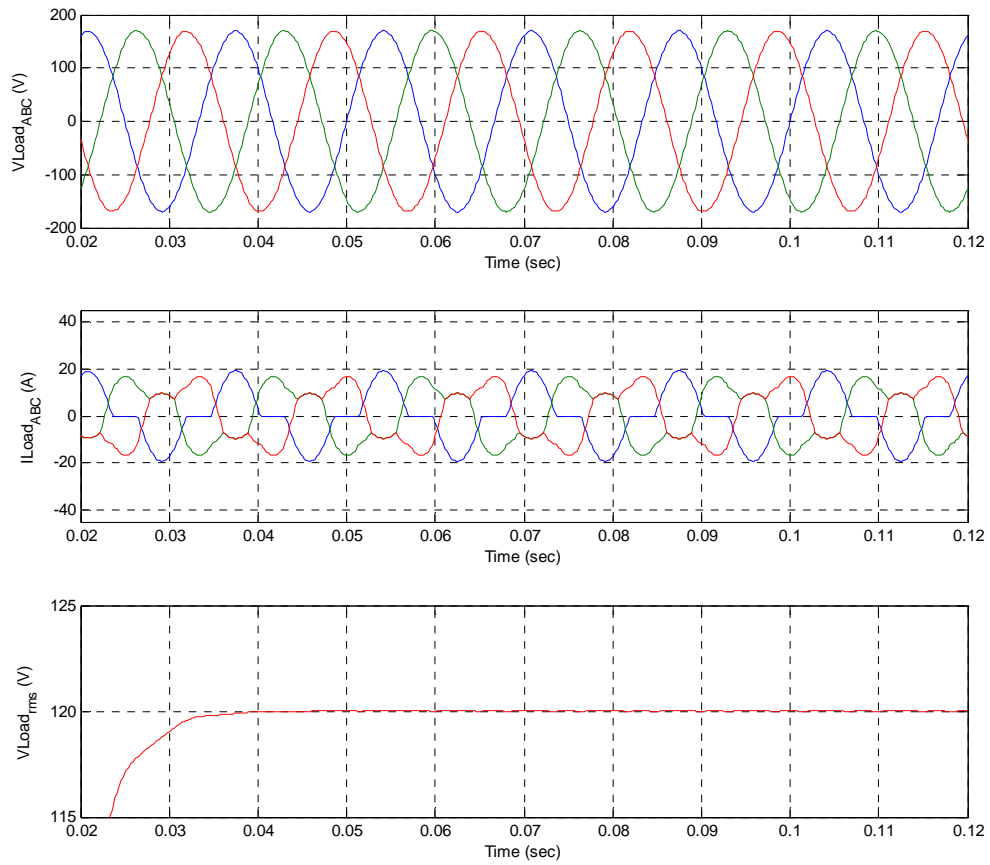


Figure 5.31 Simulation Results of the Three-Phase Inverter under Nonlinear Load (**Top:** Load Voltage, **Middle:** Load Current, **Bottom:** Load (RMS) Voltage)

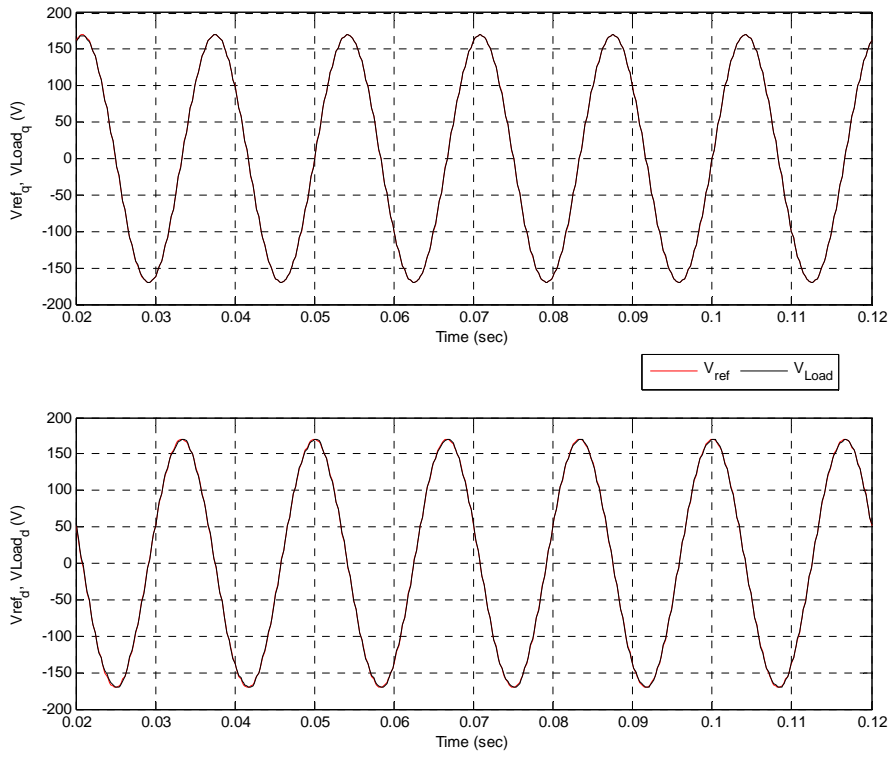


Figure 5.32 Comparison of the Reference Voltage with the Actual Load Voltage of the Three-Phase Inverter (in the d-q axis reference frame) under Nonlinear Load

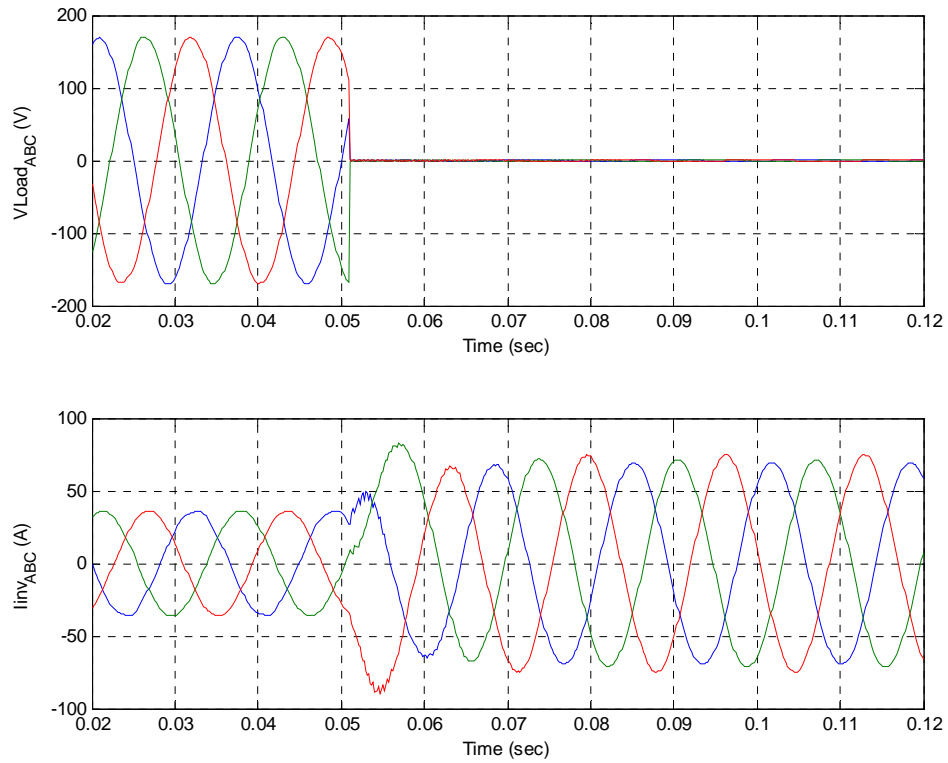


Figure 5.33 Simulation Results of the Three-Phase Inverter for Short-circuit Condition
(**Top:** Load Voltage, **Bottom:** Inverter Current)

5.11 Chapter Summary

In this chapter, a voltage and current control strategies for a single-phase and three-phase inverter are designed. Two different control strategies are applied to a single-phase and three-phase inverter operating under linear and nonlinear loads.

First, the discrete-time PID voltage and discrete-time PID current controller are used. For single-phase inverter, it is shown that the PID control technique works very well for

linear loads and achieves an acceptable level of harmonic reduction. However, with nonlinear loads the PID control technique fails to achieve a satisfactory level of harmonic suppression. This inability of the PID control technique, to suppress harmonic frequencies other than the fundamental, cannot be improved even if the PID controller gains are increased. For three-phase inverter, similar performance is observed with the PID control technique. The technique works very well for balanced linear loads, however, with unbalanced linear loads and nonlinear loads, the PID control technique does not achieve a satisfactory performance.

The second control technique – a discrete-time RSP voltage controller with a discrete-time sliding mode current controller – is then applied to the single-phase and three phase inverter.

For the single-phase inverter, it is found that this technique works very well under linear loads, as well as nonlinear loads, and achieves a satisfactory level of harmonic suppression in both cases.

A similar performance is observed for the three-phase inverter, and it is found that this technique works well under balanced linear loads, unbalanced linear loads, as well as nonlinear loads, and achieves an acceptable level of harmonic suppression.

For the single-phase inverter, reduction of 3rd harmonic frequency component is demonstrated, while, for the three-phase inverter, minimization of 5th and 7th harmonic frequency components from the system output is demonstrated.

CHAPTER 6

CONCLUSIONS AND FUTURE WORK

6.1 Conclusions of the Dissertation

In this dissertation, an analysis of the fuel cell-based distributed generation (DG) system is performed. New approaches are proposed to model the behavior of the fuel cell. The models of the other units of the DG system are also presented. The behavior of the fuel cell-based DG system is studied, by performing mathematical analyses and simulation studies. Suitable control strategies are designed for the dc/dc boost converter as well as, for the single-phase and three-phase inverter, used in the DG system.

A PEM fuel cell is one of the potential candidates for DG applications. Research in this dissertation is focused on the proton exchange membrane (PEM) fuel cell. First, the behavior of the PEM fuel cell is understood by developing a novel state space model of 500-W PEM fuel cell. The important physical processes inside the PEM fuel cell system are modeled, and it is found that the transient response of the PEM fuel cell over a short-time period is mainly dominated by the capacitance of a charge double-layer formed on the surface of the cathode of the PEM fuel cell, while, the transient response of the PEM fuel cell over a long-time period mainly depends on the thermodynamic processes and flow delays inside the PEM fuel cell system. It is also found that the irreversible voltage

losses in the PEM fuel cell system can be reduced, by operating the PEM fuel cell at the higher values of input variables.

A novel state space model of the PEM fuel cell developed in this dissertation is well-suited for the PEM fuel cell control studies. The model can be used to design advanced control strategies to control the output voltage of the PEM fuel cell, by regulating the channel input pressures, and flow rates, of hydrogen and oxygen supplied to the PEM fuel cell.

The use of nonparametric modeling approach to model the behavior of the PEM fuel cell is also demonstrated. It is shown that the nonlinear dynamics of the PEM fuel cell can be effectively modeled using a two-layer recurrent neural network. The neural network modeling approach is extremely useful when the process parameters are unknown or difficult to determine. The training of the neural network model for the PEM fuel cell's output voltage and stack temperature values is shown and the analysis of the dynamic behavior of the PEM fuel cell, using the neural network model, is demonstrated.

The neural network modeling approach can be used to develop nonparametric models for other energy sources of the DG system, such as – microturbines, wind power generators, photovoltaic arrays, as well as other types of fuel cells used in DG applications, such as- phosphoric acid fuel cells (PAFC), solid oxide fuel cells (SOFC), molten carbonate fuel cells (MCFC).

The energy storage element is an important element in the DG system. In this dissertation, the sizing of the lead-acid battery bank is performed for the stand-alone 5-kW PEM fuel cell-based DG system feeding to the residential loads. Further, the

charging of the battery bank, using the PEM fuel cell array and dc/dc boost converter, is demonstrated. A sliding mode control law is designed, for the dc/dc boost converter, to control its output voltage.

Two different control strategies are designed for the single-phase and three-phase inverter. First, the PID control technique is used, and the discrete-time PID voltage controller and discrete-time PID current controller is designed. For the single-phase inverter, it is found that the PID control technique works very well for linear loads, and achieves an acceptable level of harmonic reduction. However, with nonlinear loads, the PID control technique performs poorly, and cannot achieve a satisfactory level of harmonic suppression. Total harmonic distortion (THD) in the output voltage is found to be more than 5% under nonlinear load with the crest factor 3:1.

For the three-phase inverter, a similar result is observed. The PID control technique performs satisfactorily with balanced linear loads. However, with unbalanced linear loads and nonlinear loads, it cannot achieve a satisfactory harmonic reduction. Total harmonic distortion (THD) in the output voltage, under unbalanced linear loads and nonlinear loads, is found to be more than 10%.

The second control technique – a discrete-time RSP voltage controller with a discrete-time sliding mode current controller – is then designed for the single-phase and three-phase inverter. It is found that this technique is quite effective under all the loading conditions, and achieves an acceptable level of harmonic suppression for balanced linear loads, unbalanced loads, as well as for nonlinear loads. Total harmonic distortion (THD)

in the output voltage is found to be less than 2% for all the loading conditions, for both single-phase, as well as three-phase inverter.

6.2 Future Work

The models and methods proposed, in this dissertation, to analyze the performance of the fuel cell-based DG system, can be used to perform future research as follows:

(i) A state space model of the PEM fuel cell, proposed in this dissertation, can be used to develop the advanced control strategies to control the output voltage of the PEM fuel cell. Also, models of other DG system technologies, such as – microturbines, photovoltaic cells, and other fuel cells such as, SOFC, MCFC, can be developed based on the proposed PEM fuel cell modeling approach presented in this dissertation.

(ii) This dissertation uses the lead-acid battery as the energy storage element. However, other energy storage devices, such as an ultracapacitor, which has different properties than the lead-acid battery, can be used to analyze the operation of the DG system.

(iii) In this dissertation, the energy storage element is placed on the high-voltage side of the dc/dc boost converter. This topology has certain advantages, as well as certain disadvantages. The performance of the DG system can also be assessed by connecting the energy storage element on the low-voltage side of the dc/dc boost converter.

BIBLIOGRAPHY

- [1] Ellis M.W., Von Spakovsky M.R, Nelson D.J., "Fuel Cell Systems: efficient, flexible energy conversion for the 21st century", *Proceedings of IEEE*, Vol. 89, Issue 12, pp. 1808-1818, Dec. 2001.
- [2] J.H. Scott," The Development of Fuel Cell Technology for Electric Power Generation: From NASA's Manned Space Program to the "Hydrogen Economy"", *Proceedings of the IEEE*, Vol. 94, Issue 10, pp. 1815-1825, Oct. 2006.
- [3] Andreas Poullikkas, "Implementation of distributed generation technologies in isolated power systems", *Renewable and Sustainable Energy Reviews*, Vol. 11, Issue 1, pp. 30-56, January 2007.
- [4] G. Pepermans, J. Driesen, D. Haeseldonckx, R. Belmans and W. D'haeseleer, "Distributed generation: definition, benefits and issues", *Energy Policy*, Vol. 33, pp. 787-798, 2005.
- [5] Thomas Ackermann, Göran Andersson and Lennart Söder, "Distributed generation: a definition" *Electric Power Systems Research*, Vol. 57, Issue 3, pp. 195-204, 20 April 2001.
- [6] W. El-Khattam and M. M. A. Salama, "Distributed generation technologies, definitions and benefits", *Electric Power Systems Research*, Vol. 71, Issue 2, pp. 119-128, October 2004.
- [7] Andreas Poullikkas, "Implementation of distributed generation technologies in isolated power systems", *Renewable and Sustainable Energy Reviews*, Vol. 11, Issue 1, pp. 30-56, January 2007.
- [8] Williamson, S.S., Emadi, A., Shahidehpour, M.," Distributed fuel cell generation in restructured power systems", *IEEE Power Engineering Society General Meeting*, Vol. 2, pp. 2079-2084,6-10 June 2004.
- [9] Ausilio Bauen, David Hart and Adam Chase, "Fuel Cells for distributed generation in developing countries - an analysis", *International Journal of Hydrogen Energy*, Vol. 28, Issue 7, pp. 695-701, July 2003.

- [10] D. Morsi Ali, S. K. Salman, "A Comprehensive Review of the Fuel Cells Technology and Hydrogen Economy", *Proceedings of the 41st International Universities Power Engineering Conference (UPEC)*, Vol. 1, pp. 98-102, 6-8 Sept. 2006.
- [11] Pukrushpan J.T., Stefanopoulou A.G., and Huei Peng "Control of Fuel Cell Breathing", *IEEE Control Systems Magazine*, Vol. 24, Issue 2, pp. 30-46, April 2004.
- [12] Marwali, Mohammad Nanda, "Digital control of pulse width modulated inverters for high performance uninterruptible power supplies", Ph.D. Dissertation, Ohio State University, Columbus, OH, 2004.
- [13] Min Dai, "Control of power converters for distributed generation applications", *Ph.D. Dissertation*, Ohio State University, Columbus, OH 2005.
- [14] Georgakis D., Papathanasiou S., Manias S., "Modeling and Control of a Small Scale Grid-connected PEM Fuel Cell System", *IEEE 36th Power Electronics Specialists Conference*, pp. 1614-1620, 2005.
- [15] J. C. Amphlett, R.M. Baumert, R.F. Mann, B.A. Peppley, P. R. Roberge, and Harris T.J , "Performance Modeling of the Ballard Mark IV Solid Polymer Electrolyte Fuel Cell, I. Mechanistic Model Development", *Journal of The Electrochemical Society*, Vol. 142, Issue 1, pp. 1-8, January 1995.
- [16] J. C. Amphlett, R. M. Baumert, R.F. Mann, B.A. Peppley, P. R. Roberge, and Harris T.J, "Performance Modeling of the Ballard Mark IV Solid Polymer Electrolyte Fuel Cell II. Empirical Model Development", *Journal of The Electrochemical Society*, Vol. 142, Issue 1, pp. 9-15, January 1995.
- [17] T. E. Springer, T. A. Zawodzinski, and S. Gottesfeld, "Polymer Electrolyte Fuel Cell Model", *Journal of The Electrochemical Society*, Vol. 138, Issue 8, pp. 2334-2342, August 1991.
- [18] Daisie D. Boettner, Gino Paganelli, Yann G. Guezennec, Giorgio Rizzoni, and Michael J. Moran, "Proton Exchange Membrane Fuel Cell System Model for Automotive Vehicle Simulation and Control", *Journal of Energy Resources Technology*, Vol. 124, Issue 1, pp. 20-27, March 2002.
- [19] Pasricha S., Shaw S.R., "A dynamic PEM fuel cell model ", *IEEE Transactions on Energy Conversion*, Vol. 21, Issue 2, pp. 484-490, June 2006.

- [20] Caisheng Wang, Nehrir, M.H., Shaw S.R., "Dynamic Models and Model Validation for PEM Fuel Cells Using Electrical Circuits", *IEEE Transactions on Energy Conversion*, Vol. 20, Issue 2, pp. 442-451, June 2005.
- [21] Garnier J., Pera M.C., Hissel D., Harel F., Candusso D., Glandut N., Diard J.P., De Bernardinis A., Kauffmann J.M., Coquery G., " Dynamic PEM fuel cell modeling for automotive applications", *IEEE 58th Vehicular Technology Conference (VTC)*, Vol. 5, pp. 3284-3288, 6-9 Oct. 2003.
- [22] Friede W., Rael S., Davat B., " Mathematical model and characterization of the transient behavior of a PEM fuel cell", *IEEE Transactions on Power Electronics*, Vol. 19, Issue 5, pp. 1234-1241, Sept. 2004.
- [23] Yu D., Yuvarajan S., " A novel circuit model for PEM fuel cells", *Nineteenth Annual IEEE Applied Power Electronics Conference and Exposition (APEC)*, Vol. 1, pp. 362-366, 2004.
- [24] Kong Xin, Khambadkone, A.M., " Dynamic modelling of fuel cell with power electronic current and performance analysis", *The Fifth International Conference on Power Electronics and Drive Systems, PEDS*, Vol. 1, pp.607-612, 17-20 Nov. 2003.
- [25] Qiuli Yu, Song-Yul Choe, Srivastava A.K., Wenzhong Gao, "Improved Modeling and Control of a PEM Fuel Cell Power System for Vehicles", *Proceedings of the IEEE Southeast Con. 2006*, pp. 331-336, March 31 2005-April 2 2006.
- [26] Tirnovan R., Miraoui A., Munteanu R., Vadan I., Balan H., " Polymer Electrolyte Fuel Cell System (PEFC) Performance Analysis", *IEEE International Conference on Automation, Quality and Testing, Robotics*, Vol. 1, pp. 457-462, May 2006.
- [27] Haubrock J., Heideck G., Styczynski Z., "Dynamic Investigation on Proton Exchange Membrane Fuel Cell Systems", *IEEE Power Engineering Society General Meeting*, pp. 1-6, 24-28 June 2007.
- [28] Lu-Ying Chiu, Diong B., Gemmen R.S., " An improved small-signal model of the dynamic behavior of PEM fuel cells", *IEEE Transactions on Industry Applications*, Vol. 40, Issue 4, pp. 970-977, July-Aug. 2004.
- [29] Caisheng Wang; Nehrir, M.H., "A Physically Based Dynamic Model for Solid Oxide Fuel Cells", *IEEE Transaction on Energy Conversion*, Vol. 22, Issue 4, pp. 887-897, Dec. 2007.

- [30] J. Padulles, G.W. Avult, and J.R. McDonald, " An integrated SOFC plant dynamic model for power systems simulation", *Journal of Power Sources*, Vol. 86, pp. 495-500, March 2000.
- [31] S. Jemei, D. Hissel, M.C. Pera, J.M. Kauffmann, "Dynamical Recurrent Neural Network towards Modeling of On-board Fuel Cell Power Supply", *2004 IEEE International Symposium on Ind.Electron.*, vol.1, pp. 471-476, May 2004.
- [32] S. Jemei, D. Hissel, M.C. Pera, J.M. Kauffmann, "Black Box Modeling of Proton Exchange Membrane Fuel Cell Generators", *28th Annual Conf. of the Ind.Electon. Society, IECON'02*, vol. 2, pp. 1474-1478, Nov. 2002.
- [33] Hatti M., Tioursi M., Nouibat W.," Static Modelling by Neural Networks of a PEM Fuel Cell ", *IEEE 32nd Annual Conference on Industrial Electronics, IECON 2006*, pp. 2121-2126, Nov. 2006.
- [34] Sun Tao,YAN Si-jia, CAO Guang-yi, ZHU Xin-jian, "Modeling and Control PEMFC using Fuzzy neural networks", *Journal of Zhejiang University SCIENCE*, 2005, pp. 1084-1089, 2005.
- [35] Wang C., Nehrir M.H., Gao H.," Control of PEM fuel cell distributed generation systems", *IEEE Transactions on Energy Conversion*, Vol. 21, Issue 2, pp. 586-595, June 2006.
- [36] Uzunoglu M., Alam M.S.," Dynamic modeling, design, and simulation of a combined PEM fuel cell and ultracapacitor system for stand-alone residential applications", *IEEE Transactions on Energy Conversion*, Vol. 21, Issue 3, pp. 767-775, Sept. 2006.
- [37] Tanrioven, M., Alam, M. S., "Modeling, Control, and Power Quality Evaluation of a PEM Fuel Cell-Based Power Supply System for Residential Use", *IEEE Transactions on Industry Applications*, Vol. 42, No. 6, pp. 1582-1589, Nov-Dec. 2006.
- [38] Sedghisigarchi K., Feliachi A.," Dynamic and transient analysis of power distribution systems with fuel Cells-part I: fuel-cell dynamic model", *IEEE Transactions on Energy Conversion*, Vol. 19, Issue 2, pp. 423-428, June 2004.
- [39] Sedghisigarchi K., Feliachi A.," Dynamic and transient analysis of power distribution systems with fuel Cells-part II: control and stability enhancement", *IEEE Transactions on Energy Conversion*, Vol. 19, Issue 2, pp. 429-434, June 2004.

- [40] E.J. Davison, and B. Scherzinger, "Perfect Control of the robust servomechanism problem", *IEEE Trans. On Automatic Control*, 32(8), pp. 689-702, 1987.
- [41] E.J. Davison and I.J. Ferguson, "The design of controllers for the multivariable robust servomechanism problem using parameter optimization methods", *IEEE Transactions on Automatic Control*, Vol. AC-26, pp. 93-110, Feb. 1981.
- [42] E.J. Davison and A. Goldenberg, "Robust control of a general servomechanism problem: The servo-compensator", *Automatica*, Vol. 11, pp.461-471, 1975
- [43] E.J. Davison, " The robust control of a servomechanism problem for linear time-invariant multivariable systems", *IEEE Transactions on Automatic Control*, Vol. AC-26, No.1, pp. 25-34, 1976.
- [44] V. Utkin, J. Guldner, and J.X. Shi, *Sliding Mode Control in Electromechanical Systems*, London, U.K.: Taylor and Francis, 1999.
- [45] Jin-Woo Jung, "Modeling and control Fuel Cell based Distributed Generation Systems", Ph.D. Dissertation, Ohio State University, Columbus, OH, 2005.
- [46] Ceraolo, M., "New dynamical models of lead-acid batteries", *IEEE Transactions on Power Systems*, Vol. 15, Issue 4, Nov. 2000, pp. 1184-1190.
- [47] Chan H.L., Sutanto D., "A new battery model for use with battery energy storage systems and electric vehicles power systems" , *IEEE Power Engineering Society Winter Meeting*, Vol. 1, pp. 470-475, 2000.
- [48] Salameh Z.M., Casacca M.A., and Lynch W.A., "A mathematical model for lead-acid batteries", *IEEE Transactions on Energy Conversion*, Vol. 7, No. 1, pp. 93-98, 1992.
- [49] Berndt D. " Maintenance-free batteries", 2nd ed. Taunton, UK: Research Studies Press Ltd., 1997.
- [50] Matthias Dürr, Andrew Crudena, Sinclair Gaira and J.R. McDonald, "Dynamic model of a lead acid battery for use in a domestic fuel cell system" , *Journal of Power Sources*, Vol. 161, Issue 2, October 2006, pp. 1400-1411.
- [51] Jantharamin N., Zhang, L., "A new dynamic model for lead-acid batteries", 4th IET Conference on Power Electronics, Machines and Drives, April 2008, pp. 86-90.
- [52]] NP valve regulated lead acid battery manual, Yuasa Battery Sale (UK) Ltd., 1991.

- [53] N. Mohan , T.M. Undeland, and W.P. Robbins, *Power Electronics: Converters, Applications, and Design*. New York: Wiley, 2003.
- [54] James Larminie and Anderw Dicks, *Fuel Cell Systems Explained*, 1st ed. New York: Wiley, 2000, pp. 29-52.
- [55] U.S. Department of Energy website, Energy Efficiency and Efficient Energy. [Online]. Available: http://www1.eere.energy.gov/hydrogenandfuelcells/fuelcells/fc_types.html
- [56] G. Kortum, *Treatise on Electrochemistry*, 2nd ed. New York:El-sevier, 1965.
- [57] National Energy Technology Laboratory, *Fuel Cell Hand Book*, 6th ed. Nov. 2002.
- [58] G..N. Hatsopoulos and J.H. Keenan, *Principles of General Thermodynamics*. 1st ed. New York: Wiley, 1965.
- [59] Calderon G., Draye J.-P., Pavisic D., Teran R., Libert G., "Nonlinear dynamic system identification with dynamic recurrent neural networks", *Proceedings of International Workshop on Neural Networks for Identification, Control, Robotics, and Signal/Image Processing*, pp. 49-54, 21-23 Aug. 1996.
- [60] Neural Network Toolbox (Version 5.0.2) , MATLAB 7.4.0.287 (R2007a), MATLAB/Simulink Help.
- [61] Olivera Jovanovic, "Identification of Dynamic System Using Neural Network", The scientific Journal FACTA UNIVERSITATIS, Vol. 1, No. 4, pp. 525-532, 1997.
- [62] Ali Keyhani, Wenzhe Lu, Gerald T. Heydt, "Composite Neural Network Load Models for Power System Stability Analysis," *IEEE Power Engineering Society 2004 Power Systems Conference & Exposition*, Vol. 2, pp. 1159-1163, New York city, October 10-13, 2004.
- [63] Mahmoud El-Gohary; Mcnames, J., Ellis, T., Goldstein, B.,"Time Delay and Causality in Biological Systems Using Whitened Cross-Correlation Analysis", in *proc.of 28th IEEE EMBS Conf.*, pp. 6169-6172, New York City, Aug 2006.
- [64] C.H. Knapp and G.C. Carter, "The generalized correlation method for estimation of time delay", *IEEE Trans. Acoustics ,Speech and Signal Processing*, vol. 24, Issue 4, pp. 320-327, Aug 1976.

- [65] Lance C. Benn, Bruce Burton and Ron G. Harley, "Online Converter fed Induction Motor Impulse Response Identification and Parameter Extraction using Pseudorandom Modified PWM", *4th IEEE International Symposium on Diagnostics of Electric Machines, Power Electronics and Drives*, pp. 70-75, Aug. 2003.
- [66] Abrahart R. J., Dawson C. W., "Neural Network Hydrological Modelling: Linear Output Activation Functions?", *American Geophysical Union*, Fall Meeting, 2005.
- [67] S. Pillutla, A. Keyhani, and I. Kamwa, "Neural network observers for on-line tracking of synchronous generator parameters", *IEEE Trans. Energy Conversion*, vol. 14, Issue 1, pp. 23-30, March 1999.
- [68] Nelson J.P., Bolin W.D., "Basics and advances in battery systems", *IEEE Transactions on Industry Applications*, Vol. 31, Issue 2, March-April 1995, pp. 419-428.
- [69] Lead-Acid Battery, Available: http://en.wikipedia.org/wiki/Lead-acid_battery
- [70] Control Systems/Controllers and Compensators, Available: http://en.wikibooks.org/wiki/Control_Systems/Controllers_and_Compensators
- [71] Roshan Arman, Burgos Rolando, Baisden Andrew C., Wang Fred, and Boroyevich Dushan, "A D-Q Frame Controller for a Full-Bridge Single Phase Inverter Used in Small Distributed Power Generation Systems", *Twenty Second Annual IEEE Applied Power Electronics Conference, APEC 2007*, pp. 641-647, 2007.